

**INKJET-PRINTED SENSORS AND VIA-ENABLED STRUCTURES  
FOR LOW-COST AUTONOMOUS WIRELESS PLATFORMS**

A Dissertation  
Presented to  
The Academic Faculty

by

Sangkil Kim

In Partial Fulfillment  
of the Requirements for the Degree  
Doctor of Philosophy in the  
School of Electrical and Computer Engineering

Georgia Institute of Technology  
December 2014

Copyright © 2014 by Sangkil Kim

**INKJET-PRINTED SENSORS AND VIA-ENABLED STRUCTURES  
FOR LOW-COST AUTONOMOUS WIRELESS PLATFORMS**

Approved by:

Dr. Manos M. Tentzeris, Advisor  
School of Electrical and Computer  
Engineering  
*Georgia Institute of Technology*

Dr. Herve Aubert  
School of Electrical and Computer  
Engineering  
*CNRS-LAAS*

Dr. Andrew F. Peterson  
School of Electrical and Computer  
Engineering  
*Georgia Institute of Technology*

Dr. Yang Wang  
School of Civil and Environmental  
Engineering  
*Georgia Institute of Technology*

Dr. Gregory D. Durgin  
School of Electrical and Computer  
Engineering  
*Georgia Institute of Technology*

Date Approved: December 14 2014

To my family and friends

## **ACKNOWLEDGEMENTS**

I would like to acknowledge all of my committee members, especially my advisor, Professor Manos M. Tentzeris for his guidance and advice. I would also like to thank Dr. Apostolos Georgiadis (CTTC, Spain), Dr. Ana Collado (CTTC, Spain), Dr. Herve Aubert (LAAS-CNRS), Dr. Kawahara Yoshihiro (The University of Tokyo, Japan), Dr. Maurizio Bozzi (University of Pavia) and Dr. Atif Shamim (KAUST, The Kingdom of Saudi Arabia) for the interesting discussions and insight on research. Additionally, I would like to thank Dr. Young-Joong Yoon, Dr. Jong-Gwan Yook, Dr. Dae-shik Hong, and Dr. Yong-shik Lee at Yonsei University (Seoul, Korea) for their cordial advice from my undergraduate to graduate school life. I would also like to thank ATHENA group members and friends for their support. Lastly, I really would like to thank my family for endless support, love and encouragement.

# TABLE OF CONTENTS

	Page
ACKNOWLEDGEMENTS	iv
LIST OF TABLES	ix
LIST OF FIGURES	x
LIST OF SYMBOLS AND ABBREVIATIONS	xiv
SUMMARY	xvii
<u>CHAPTER</u>	
1 Introduction	1
1.1 Introduction	1
1.2 Contribution	6
2 Inkjet Printing Technology	8
2.1 Introduction	8
2.2 Inkjet-printed Silver Nanoparticle	9
2.3 Inkjet Printing of Catalyst and Electroless Copper Deposition	14
2.3.1 Paladium-Chloride (PdCl <sub>2</sub> ) Catalyst Ink	14
2.3.2 Electrical Property of the Deposited Copper	16
2.4 Summary	20
3 Low-cost Substrates	22
3.1 Introduction	22
3.2 Material Characterization Methods	23
3.2.1 Ring Resonator Method	24

3.2.2 T-resonator Method	27
3.3 Synthetic Paper: Teslin	29
3.4 Poly(methyl methacrylate) (PMMA)	31
3.5 Summary	33
4 Printed Wireless Components for Autonomous Sensor Platform	36
4.1 Introduction	36
4.2 Inkjet-printed AMC Ground	38
4.2.1 AMC Plane Design	38
4.2.2 Antenna Measurement	41
4.2.3 Communication Range Measurement	44
4.3 Inkjet-printed Beacon Oscillator	44
4.3.1 Passive Antenna Design and Measurement	44
4.3.2 Active Antenna Oscillator Design	49
4.3.3 Solar Power-enabled Autonomous Active Antenna	53
4.4 Dual-band Energy Harvester	60
4.4.1 Dual-band Dipole Antenna Design	60
4.4.2 Dual-band Rectenna Design	61
4.5 Summary	65
5 Printed RFID-enabled Sensors	65
5.1 Introduction	66
5.2 RFID and RFID-enabled Sensors	67
5.3 Inkjet-printed Dual-tag RFID-enabled Haptic Sensor	70
5.3.1 Dual-tag Sensing Topology	70
5.3.2 Isolation Structure: Series LC Resonator	72
5.3.3 RFID-enabled Sensor Tag with LC Resonators	75

5.3.4	Read Range Estimation	78
5.4	Experimental Results	84
5.4.1	Sensor Integration	84
5.4.2	Event Decision (Detection)	87
5.5	Chipless RFID-based Passive Fluid Sensor Platform	90
5.5.1	Operation Principle	90
5.5.2	Capacitive Gap-loaded Tunable Filter	91
5.5.3	Broadband Antenna Design	93
5.5.4	Sensor Integration and Sensing Capability	97
5.5.5	Inkjet Printing of the Sensor Platform	99
5.6	Summary	100
6	Inkjet-printed Vias and SIW Components	101
6.1	Introduction	101
6.2	Inkjet-printed SIW Components on Paper	102
6.2.1	Via Fabrication on Paper	102
6.2.2	Inkjet-printed $\mu$ Strip-to-SIW Interconnect	104
6.2.3	Inkjet-printed SIW Cavity Filter	106
6.3	Inkjet-printed Via	107
6.3.1	Challenges	107
6.3.2	Stepped-via Topology	109
6.3.3	Stepped-via Modeling	111
6.3.4	Stepped-via Fabrication	115
6.3.5	Fully Inkjet-printed SIW Interconnect	120
6.3.6	Fully Inkjet-printed SIW Slot Antenna	122
6.4	Gully Inkjet-printed SIW Multilayer Coupler	126

6.4.1 Flexible Inkjet-printed SIW Interconnect	126
6.4.2 Inkjet-printed Multilayer Coupler	128
6.4.3 Printed Multilayer Coupler Design	129
6.4 Summary	132
7 Conclusion	134
7.1 Summary and Conclusion	134
7.2 Future Work	138
7.2.1 Nanoparticle-based Ink Characterization	138
7.2.2 Develop Printable Electronic Inks	139
7.2.3 Optimize Printed Wireless Components	140
7.2.4 Integrate RFID-enabled Sensor to WSN	140
7.2.5 Optimization and Characterization of the Printed Via	141
APPENDIX A: The Effective Width and Effective Permittivity	143
REFERENCES	146
VITA	154



## LIST OF TABLES

	Page
Table 2.1: Contribution.	7
Table 2.1: Conductivity of printed silver nanoparticles.	13
Table 3.1: Dielectric material characterization methods.	25
Table 3.2: Popular materials for RF substrates.	35
Table 4.1: Circuit component values.	50
Table 6.1: Inkjet-printed vias.	108

## LIST OF FIGURES

	Page
Figure 1.1: (a) The growing number of sensor-enabled electronics	1
Figure 1.2: Research object.	6
Figure 2.1: Surface and profile of inkjet-printed silver nanoparticles.	11
Figure 2.2: Profiles of inkjet-printed traces: 1 pL.	12
Figure 2.3: Profiles of inkjet-printed traces: 10 pL.	12
Figure 2.4: Chemical reaction of catalyst-based electrolessly copper deposition.	15
Figure 2.5: Sheet resistance and conductivity.	17
Figure 2.6: Deposited coppers and cross section.	18
Figure 2.7: XRD analyses of Teslin paper.	18
Figure 2.8: EDX analyses of samples	19
Figure 3.1: Fabricated ring resonator and measurement.	30
Figure 3.2: Fabrication T-resonators and measurement.	32
Figure 3.3: Extracted relative permittivity and loss tangent.	34
Figure 4.1: Geometry of the single split ring resonator (SSRR).	39
Figure 4.2: Geometry and phase response of AMC.	39
Figure 4.3: Array size and reflection coefficient ( $S_{11}$ ) variation.	40
Figure 4.4: Fabricated antenna.	41
Figure 4.5: Reflection coefficient ( $S_{11}$ ) of the antenna with/without AMC.	42
Figure 4.6: Radiation patterns	43
Figure 4.7: Measured antenna gain.	44
Figure 4.8: Communication range comparison on body.	45
Figure 4.9: Circuit schematic	46

Figure 4.10: Folded antenna	47
Figure 4.11: Reflection coefficient ( $S_{11}$ ) of the folded slot antenna	48
Figure 4.12: Measured antenna gain.	48
Figure 4.13: Fabricated Circuit.	49
Figure 4.14: Active oscillator antenna performance versus DC-bias voltage.	51
Figure 4.15: Measured EIRP (dBm).	52
Figure 4.16: Solar-powered active antenna.	53
Figure 4.17: Solar cell $I_{SC}$ and $V_{OC}$ versus illuminance	55
Figure 4.18: Oscillation frequency versus illuminance with/without voltage regulator.	56
Figure 4.19: Radiation patterns of active antenna under sun light.	57
Figure 4.20: Measured power spectra and phase noise of active antenna.	59
Figure 4.21: Dual-band folded dipole antenna.	60
Figure 4.22: Reflection coefficient ( $S_{11}$ ) of the dual-band antenna.	61
Figure 4.23: Simulated and measured radiation patterns at 2.45 GHz.	62
Figure 4.24: Simulated and measured radiation patterns at 915 MHz.	62
Figure 4.25: Schematic of the proposed dual band rectifier.	63
Figure 4.26: Reflection coefficient ( $S_{11}$ ) of the dual band rectifier.	64
Figure 5.1: RFID application areas.	68
Figure 5.2: RFID tag and RFID-enabled sensor tag.	69
Figure 5.3: RFID-enabled sensor topologies.	70
Figure 5.4: The LC resonator and the proposed RFID-enabled sensor.	73
Figure 5.5: Parameter sweep of the LC resonator structure.	74
Figure 5.6: Crosstalk level with/without the LC resonators.	76
Figure 5.7: S-parameters ( $S_{11}$ & $S_{22}$ ) of the sensor tag and the reference tag.	77
Figure 5.8: Inkjet-printed RFID-enabled sensor on paper substrate.	79

Figure 5.9: Radiation patters of the RFID-enabled sensors.	80
Figure 5.10: Read range of the RFID-enabled sensor tags at 915 MHz.	84
Figure 5.11: Measurement procedure.	85
Figure 5.12: Measured backscattered power before/after event occurrence.	86
Figure 5.13: Absolute power level difference before/after the event occurrence.	87
Figure 5.14: Operation principle of the proposed RFID-based sensor platform.	90
Figure 5.15: The capacitive gap-loaded tunable ring resonator filter.	92
Figure 5.16: S-parameters of the tunable filter without fluid sample.	93
Figure 5.17: S-parameters of the tunable filter with various fluid samples.	94
Figure 5.18: The proposed microstrip monopole antenna.	95
Figure 5.19: Reflection coefficient of the microstrip monopole antenna.	95
Figure 5.20: Simulated radiation patterns.	96
Figure 5.21: The measurement setup and reflection coefficient.	98
Figure 5.22: The inkjet-printed chipless RFID-based fluid sensor platform.	99
Figure 6.1: Via metallization on paper.	103
Figure 6.2: Geometry of a SIW interconnect on paper.	104
Figure 6.3: Fabricated SIW interconnect on paper.	105
Figure 6.4: Measured S-parameters.	106
Figure 6.5: Geometry and fabricated the SIW filter.	106
Figure 6.6: Simulated and measured S-parameters of SIW filter on paper.	107
Figure 6.7: Crack formation and SEM image.	108
Figure 6.8: Proposed via profiles and testing SIW structure.	109
Figure 6.9: S-parameters ( $S_{11}$ & $S_{21}$ ) of the testing SIW structures.	110
Figure 6.10: Equivalent circuit model of a cylindrical via and a stepped-via.	111
Figure 6.11: Generalized cylindrical via and stepped via circuit model.	112

Figure 6.12: Concept of equivalent via model and simulated model comparison.	115
Figure 6.13: Fabrication process of the stepped via.	116
Figure 6.14: Fabricated inkjet-printed stepped via hole.	116
Figure 6.15: Geometry of stepped via hole and SEM images: top view.	118
Figure 6.16: Geometry of stepped via hole and SEM images: side view.	119
Figure 6.17: Geometry and fabricated the $\mu$ Strip-to-SIW interconnect.	121
Figure 6.18: Measured scattering parameters of microstrip-to-SIW transition.	122
Figure 6.19: SIW slotted waveguide antenna geometry.	123
Figure 6.20: Measured reflection coefficient ( $S_{11}$ ) of the printed antenna.	125
Figure 6.21: Measured and simulated antenna gain.	125
Figure 6.22: Normalized radiation patterns at 5.6 GHz.	126
Figure 6.23: Geometry of flexible SIW interconnect and measured S-parameters.	127
Figure 6.24: Geometry of the multilayer coupler.	128
Figure 6.25: S-parameters and phase of the inkjet-printed multilayer coupler.	130
Figure 6.26: Inkjet-printed multilayer broadband coupler on polyimide film.	132

## LIST OF SYMBOLS AND ABBREVIATIONS

$\alpha_c$	Attenuation constant of conductor loss	
$\alpha_d$	Attenuation constant of dielectric material loss	
$\alpha_r$	Attenuation constant of radiation loss	
$\epsilon_r$	Dielectric constant (Permittivity)	
$\epsilon_{\text{eff}}$	Effective dielectric constant	
$\lambda$	Wavelength	
$\Omega$	Ohms	
$\mu_0$	Permeability	
$\sigma$	Conductivity	
$\tan \delta$	Loss tangent	
ADS	Advance Design System	
AMC	Artificial Magnetic Conductor	
CTE	Coefficient of Thermal Expansion	
cP	Center Poise	
CPW	Coplanar Waveguide	
BAN	Body Area Network	
BCB	Bisbenzocyclobutene-based monomer	
BW	Bandwidth	
dB	Decibels	
dBc	dB relative to the carrier	
dB <sub>i</sub>	dB isotropic	
dBm	dB power relative to mW	
DC	Direct Current	

DPI	Dots Per Inch
EIRP	Equivalent Isotropically Radiated Power
EBG	Electromagnetic Band Gap
EDX	Energy Dispersive X-ray spectroscopy
EM	Electromagnetics
EPC Gen2	Electronic Product Code Generation 2
GHz	Giga Hertz
GPa	Giga Pascal
Hz	Hertz
IoT	Internet of Things
IL	Insertion Loss
KeV	Kilo Electronvolt
LCP	Liquid Cristal Polymer
LTCC	Low Temperature Co-fired Ceramic
MHz	Mega Hertz
mm	Millimeter
mmWave	Millimeter wave
nH	Nano Henry
nm	Nanometer
$\mu\text{m}$	Micrometer
$\mu\text{Strip}$	Microstrip
PEC	Perfect Electric Conductor
pF	Pico Farad
pL	Pico Liter
ppm	Part Per Million

PLL	Phase Locked Loop
PMC	Perfect Magnetic Conductor
PMMA	Poly(methyl methacrylate)
RF	Radio Frequency
RFID	Radio Frequency Identification
SIW	Substrate Integrated Waveguide
SMD	Surface Mount Device
SRR	Split Ring Resonator
SSRR	Single Split Ring Resonator
TRL	Thru-Reflection-Line
UWB	Ultra Wide Band
VCO	Voltage Controlled Oscillator
VNA	Vector Network Analyzer
WLAN	Wireless Local Area Network
WPT	Wireless Power Transfer
WSN	Wireless Sensor Network
XRD	X-Ray Diffraction



## SUMMARY

Fundamental research to implement the printed autonomous wireless sensor platform is studied in three aspects: fabrication method, material selection, and novel applications for autonomous sensing/communication. Additive fabrication processes, such as inkjet printing technology and electroless electroplating, are discussed and the additively created metal layers are characterized. Fundamentals for material characterization utilizing resonators are presented and electrical properties of flexible low-cost substrates like synthetic Teslin paper and Poly(methyl methacrylate) (PMMA) are characterized. Widely used flexible substrates for printing, such as Liquid Crystal Polymer (LCP) and Kapton (polyimide), are summarized and tabulated as well. Novel antenna-based applications for efficient and autonomous operation of wireless sensor system, such as an antenna on Artificial Magnetic Conductor (AMC) for wearable applications, an active beacon oscillator for Wireless Power Transfer (WPT), and a multiband RF energy harvester, are designed and their performances are experimentally verified. The printed RFID-enabled sensor topologies with/without RFID chip are discussed as a new sensor platform for autonomous wireless operation. Fully inkjet-printed via topology for system miniaturization and integration is proposed for the first time. Challenges, circuit modeling and experimental data are presented. Future and remaining work to implement the novel low-cost autonomous wireless sensor platform are also discussed.

# CHAPTER 1

## INTRODUCTION

### 1.1 Introduction

A printed flexible sensor platform is one of the most promising research areas as growing demand of the portable ubiquitous computing system involving multidisciplinary research areas, such as the Internet of Things and wearable computing as shown in Figure 1.1. Implementing novel sensor-integrated systems is a critical factor because they recognize the surrounding environment and interact with users or machines [1][2]. It is not efficient to integrate conventional wireless sensors to the emerging sensor-based system concepts, such as ubiquitous computing and the Internet of Things (IoT), because the emerging sensor-based system requires low-cost flexible autonomous wireless sensors [2]. It is necessary to utilize a low-cost flexible substrate and fabrication method, which satisfy design specifications. The flexibility is an important design factor for the universal mounting and wearable applications, and a multi-layer structure is a critical factor for the system integration and miniaturization. Once the fabrication method and substrate for the application are chosen, it is important to verify the feasibility and

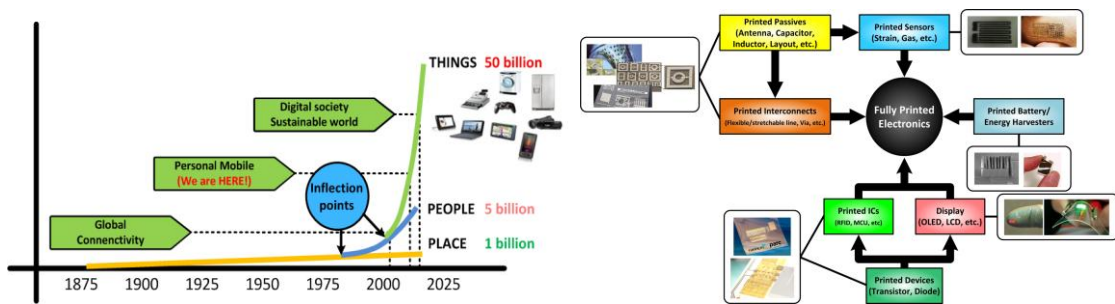


**Figure 1.1** (a) The growing number of sensor-enabled electronics and (b) research areas of the printed electronics.

capability of them to implement the autonomous wireless sensor system. The cost of the sensors are also an important factor since a huge quantity of sensors are going to be deployed.

Inkjet printing technology is a well known technology for most people as it is one of the most common method of printing in both personal and commercial settings [3][4]. In the field of electrical engineering, it has been shown that conductive traces can be formed by using a conductive ink [5]. This method of printing has also been shown to be usable for a variety of different substrates in addition to paper, many of which are greatly flexible [6-8]. The ability to utilize flexible substrates, as well as it being a completely additive method of fabrication, has led many research groups to investigate its properties and applications. Beyond the use of flexible substrates, the ever growing demand for low-cost, environmentally friendly, and flexible wireless devices has brought about brilliant progress. Inkjet printing is a purely additive process, only depositing conductive lines where needed, which does not produce unwanted material, such as in etching and milling where waste chemicals and/or materials are produced. The inkjet printing method only uses as much ink as it needs and produces no byproducts, unlike the conventional methods. Therefore, lots of metals can be saved without extra.

Selecting proper substrate materials depending on applications is one of the most important design steps because material for the substrate determines relative dielectric constant ( $\epsilon_r$ ), loss ( $\tan \delta$ ) and flexibility. The thickness of the substrate is also an important design parameter. It is directly related to effective relative dielectric constant ( $\epsilon_{\text{eff}}$ ) which affects resonance frequency as well as feature sizes of the structures on the substrate. The loss of the substrate should be considered when the substrate is chosen,

too. The loss of the substrate may limit microwave circuit designs since some kinds of designs are not compatible with high loss substrates like a cavity filter or an antenna with a high-Q factor. For the flexibility, the thickness and the natural property of the substrate material are critical. The flexible substrates are preferred for certain applications such as biomedical applications. The material and the thickness should be carefully chosen based on requirements of desired applications. It is necessary step to decide how much flexibility is required and what kind of structure is suitable on flexible substrate since performance of microwave structures are affected by their shape.

Implementation of flexible passive microwave circuit components, such as antennas, inductors, and transformers, utilizing substrates such as paper, polyethylene terephthalate (PET) and textiles is receiving significant attention. The possibility of the inkjet printing of a complete System-On-Substrate (SoS), based on multilayer flexible substrate modules and inkjet deposition of active devices remains a challenge, especially when it comes to operating at microwave frequencies [9]. While inkjet printing of semiconducting polymers to develop organic thin film transistors (OTFTs) is still far from operation in the GHz frequency range, integration of off-the-shelf active electronic components onto flexible substrates provides an exciting alternative. The realization and integration of active and passive topologies, sensors and energy harvesting topologies on flexible substrates, combined with passive interconnects, transmission lines and antennas, presents a significant challenge with few notable examples. Furthermore, extending the operational autonomy of wireless sensors and transceivers has spurred significant efforts related to energy harvesting technologies, as well as wireless power transmission. Towards this goal, various passive, active energy harvesting-enabled electronics on a

flexible low-cost paper substrate taking advantage of the capabilities of inkjet printing technology are introduced.

Over the last decade RFID-enabled sensing systems have received an increasing level of attention mostly due to their relative simple system architecture, that typically consist of simple sensing tags and interrogation readers, facilitating their integration with other existing Wireless Sensor Networks (WSN) and RFID infrastructure. In addition, a passive RFID sensing system's life time is longer and its cost is much lower compared to active sensing systems, while RFIDs can constitute low-power wireless platforms with broad sensing capabilities including temperature, gas, strain and humidity sensing. The RFID-enabled sensor systems could potentially be one of the most enabling factors to implement realistic large-scale topologies of Internet of things (IoT). Nevertheless, there are still numerous challenges on implementing the proposed RFID-enabled sensor with the dual tag sensing topology. First of all, the crosstalk between the multiple tags utilized in the sensor should be considered. A higher amount of power is required to activate the dual-tag sensor compared to typically used single-tag sensor topologies since multiple RFID IC's should be activated by the reader, otherwise the same amount of interrogation power results in shorter reading ranges. It is important to find an optimal distance between the two dipole antennas in order to minimize the size of the sensor as well as the crosstalk level, thus preventing unwanted power losses. The cost of the RFID-enabled sensor is also a critical factor for large-scale practical implementations.

Most of the reported inkjet-printed electronics on flexible substrate are single-layered structures because it is challenging to implement vias which are one of the most critical factors for the realization of highly integrated systems and multi-layered structures. Only

a small number of technologies for implementing vias utilizing inkjet printing technology have been reported, all of which have been implemented on very thin substrates with thickness below 100  $\mu\text{m}$  [10-12]. Such thin substrates are not suitable for applications in relatively lower frequency bands, such as mobile, WiFi, ISM, etc. The feature size of microwave components such as the width of microstrip line is very narrow on the thin substrate, which results in high design sensitivities to fabrication tolerances. The radiation efficiency of antennas, like patches, resonators and waveguide structures, such as substrate-integrated waveguides (SIW), is significantly affected by the substrate thickness. Therefore it is necessary to develop via fabrication concepts or techniques which can be applied on various of different thicknesses. The major issue in the metallization of via holes utilizing inkjet printing technology is to maintain a continuous metal layer after the sintering process, which is very challenging because the inkjet-printed silver nanoparticles shrink during sintering. The via hole topology with an exponentially tapered profile is introduced in order to facilitate the formation of continuous metal layers using conductive inks.

Three main design considerations for implementing the inkjet-printed low-cost autonomous wireless sensor platform are discussed: contemporary inkjet-printing technology, substrate material selection, and inkjet-printed microwave structures/components including vias (Figure 1.2). Chapter 2 and 3 discusses the state-of-art additive process and material selection. Chapter 4 and 5 presents the inkjet-printed

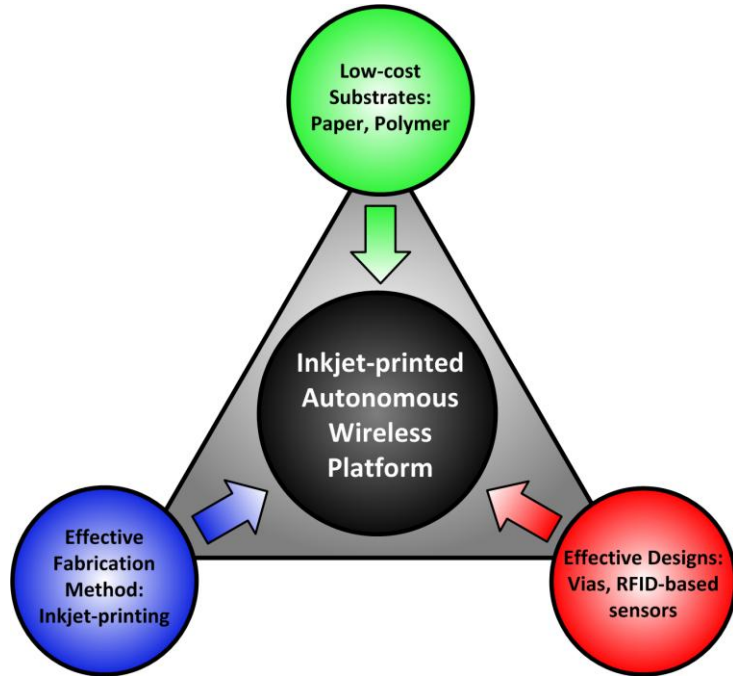


**Figure 1.2** Research object.

microwave designs including a wearable antenna, a beacon oscillator, and RFID-enabled sensors, using the data from previous chapters. Chapter 6 proposed a novel inkjet-printed via topology on many types of substrates. Chapter 7 summarizes the thesis and discusses future work.

## 1.2 Contribution

The proposed research has a disruptive impact on low-cost wireless sensor systems on flexible organic substrates like paper and polymer. First of all, the presented fully inkjet-printed via on flexible substrates such as polymer enables to realize a fully inkjet-printed multilayer structure which results in improvement of system integration and miniaturization. The proposed via topology can be applied to many inkjet-printable flexible substrates such as Kapton, and it is a first step toward the fully inkjet-printed wireless autonomous sensor platform. A fully inkjet-printed millimeter wave (mmWave)

sensors can be facilitated since a via-enabled multilayer structure is critical structure for mmWave applications such as a radar. The inkjet-printed RFID-enabled sensors on flexible paper pave the new way for scalable conformal low-cost wireless sensor/identification systems. The additive fabrication method like the inkjet-printing technology reduces by-products which result in cost effective fabrication and environmentally friendly "green" technology. The electrical properties of the silver nanoparticle ink, such as thickness and conductivity, are studied with respect to the printer cartridges (1 pL/10 pL), and these results suggest design guides on selecting inkjet cartridges. The inkjet-printed ring resonator is utilized to characterize a material for the first time and its performance is demonstrated. The proposed dual-tag sensing topology shows the stable RFID-based sensing topology. The integrated LC resonator miniaturizes the sensor tag by suppressing the crosstalk. This dual tag approach suggests the possibility of a calibration-free low-cost stable sensor platform. Numerous applications can be made out of this research because of the electrical properties of the characterized flexible inkjet-printable low-cost substrates (cellulose/synthetic paper and PMMA). The properties of inkjet-printed silver nanoparticle ink are useful basic knowledge for designing other low-cost inkjet-printed electronics on papers or polymers. These are summarized in Table 1.1.

**Table 1.1** Contribution.

<b>Area</b>	<b>Research</b>	<b>Details</b>
<b>Printed passives</b>	Printed AMC reflector	A printed high gain antenna on the "rugged"/wearable environment
<b>Printed interconnects</b>	Printed via topology & SIW structures	Via-hole metallization method using inkjet-printing technology
<b>Printed sensors</b>	RFID-enabled dual-tag sensor	Printed dual-tag RFID-enabled sensor & haptic detection method
<b>Printed circuits</b>	Beacon oscillator	Hybrid printed electronics as a cornerstone of fully printed electronics



## CHAPTER 2

### INKJET PRINTING TECHNOLOGY

#### 2.1 Introduction

Over the last decade, printing technology has dramatically advanced which enables to implement printed electronics on various substrates including flexible and organic substrates. The advent of nanoparticle ink has accelerated the progress of printing technology. The nanoparticle ink can be made from various materials such as metals, carbon based nanostructures, polymers, and semiconducting materials [13]–[17]. Due to the broad spectrum of the nanoparticle inks, inkjet printing technology has attracted lots of interest among many printing technologies. The inkjet printing technology is cheap, efficient, and environmentally friendly fabrication process because it is an additive process. It is different from other widely used fabrication method such as etching which is subtractive fabrication method. The additive process like inkjet printing technology drops nanoparticle conductor inks on the exact desired position while the subtractive process removes unwanted metal claddings from the surface of substrate utilizing acids and heavy chemicals. Therefore, there are no wasted metals and byproduct such as acid for metal removal [18]. Inkjet printing technology also enables rapid fabrication of any shapes of patterns with high resolutions up to 50  $\mu\text{m}$  without any wet processes such as photolithography, and the printing resolution can be improved as high as submicronmeter [19].

In this chapter, the electrical properties of inkjet-printed silver nanoparticles and electrolessly electroplated copper (Cu) utilizing catalyst ink are thoroughly characterized. A conductivity value, a thickness and mechanical properties of printed silver nanoparticles have been extracted. Palladium-chloride ( $\text{PdCl}_2$ ) catalyst ink is inkjet-

printed as a seed layer for electroless electroplating of copper on organic substrates. The conductivity value and the chemical reaction are discussed. These characterization data are fundamental for implementing a low-cost flexible sensor platform.

## **2.2 Inkjet-printed Silver Nanoparticle**

The properties of inkjet-printed conductors have been studied by many researchers. Specially, silver nanoparticle ink has been widely used and investigated among many types of nanoparticle inks made from silver (Ag), copper (Cu), and gold (Au) due to its low sintering temperature and high conductivity.

Silver nanoparticles form an agglomeration of silver particles 10 ~ 50 nm in size when they are deposited on the substrate and they are surrounded by a polymer coating which is used as a dispersant while the particles are in ink form. The mean diameters of the drops of nanosilver particles are about 28  $\mu\text{m}$  with a volume of 1 pL droplet and 45  $\mu\text{m}$  with 10 pL droplets [20]. Upon deposition, the net structures have a low conductivity because the particles are suspended in a solvent. A sintering process is required to evaporate the solvent and melt the particles together to achieve high conductivity. The heat sintering is examined in this paper as it is the most common of the methods to sinter metallic nanoparticles. However, other processes such as laser, UV flash lamp, and microwave sintering have been demonstrated and utilized [21-23]. Several variables play an important role in the conductivity of the printed structures. Number of ink layers printed, surface roughness of the substrate, sintering temperature, and ink properties, such as nanoparticle concentration, are the key factors determining conductivity of printed inks. It is also important to select and optimize printing parameters for the best printing

resolution, accuracy and repeatability: ink droplet volume, drop spacing, printing waveform of the nozzle, nozzle temperature, and temperature of the substrate.

Heat sintering is one of the most common methods of annealing or melting nanoparticle inks to form continuous conducting structures. Metallic nanoparticles exhibit a unique property in which their small size decreases their melting point to temperatures as low as 80 °C, which is important when printing on substrates such as paper and plastic which cannot be handled at high temperatures. Figure 2.1 shows the surface of the printed nanosilver particle image using Veeco Atomic Force Microscopy (AFM) [24]. The measured arithmetic average ( $R_a$ ) and root mean squared ( $R_q$ ) roughness are 11.4 nm and 14.4 nm respectively.

To extract conductivity, a series of traces are printed on a paper substrate using 1, 3, and 5 layers of ink and all printed structures use a 10 pL cartridge with 1024 dpi (20  $\mu$ m drop spacing). The substrates are then placed in an air-filled oven at atmospheric pressure using different times and temperatures for curing. The resistance of the traces is then measured on a Cascade probing station. The thickness of the layers were measured to extract the conductivity from the sheet resistance using a Dekktak profilometer as shown in Figure 2.2 and Figure 2.3. Each layer adds approximately 250 nm of thickness for a 1 pL cartridge and 500 nm of thickness for a 10 pL cartridge. The conductivity can be extracted using the cross-sectional area of the trace and the sheet resistance, because the conductivity is in inverse proportion to the product of sheet resistance and cross-sectional area of the trace. Using the area of the traces along with their resistance yields the conductivity of the sintered nanoparticle inks as shown in (1).

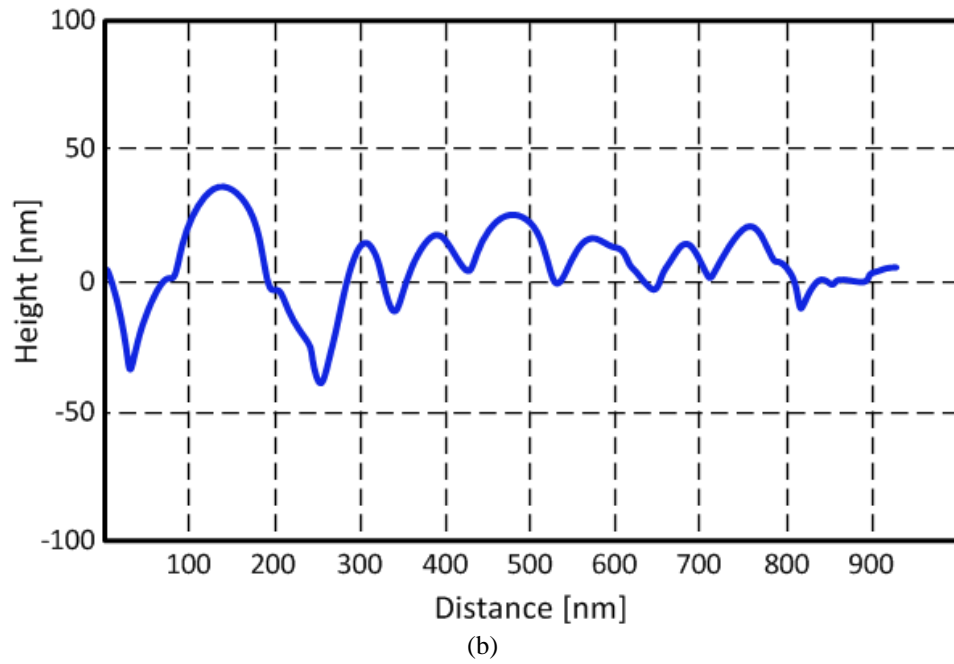
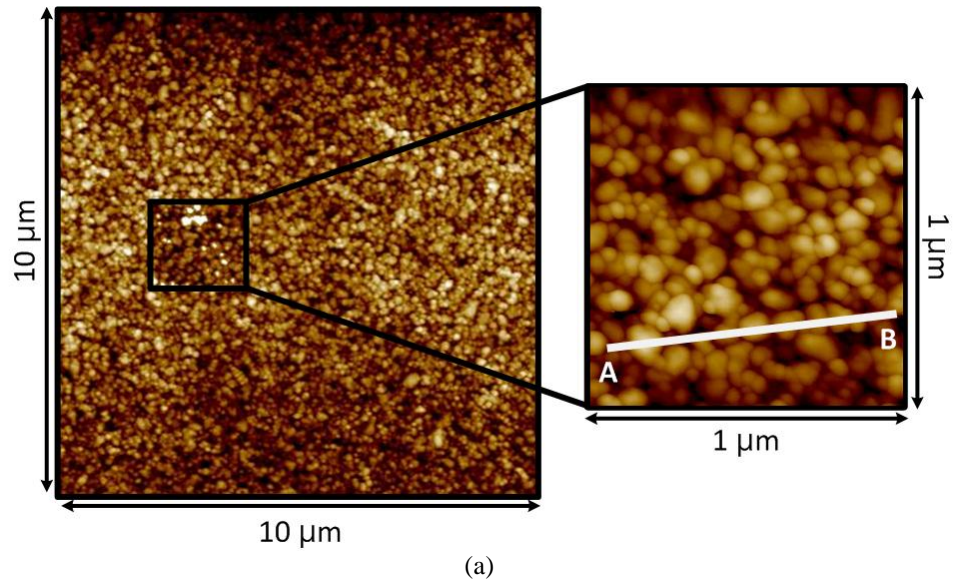


**Figure 2.1** Surface and profile of inkjet-printed silver nanoparticles: (a) AFM image of inkjet-printed silver nanoparticles (b) cross section of  $\overline{AB}$ .

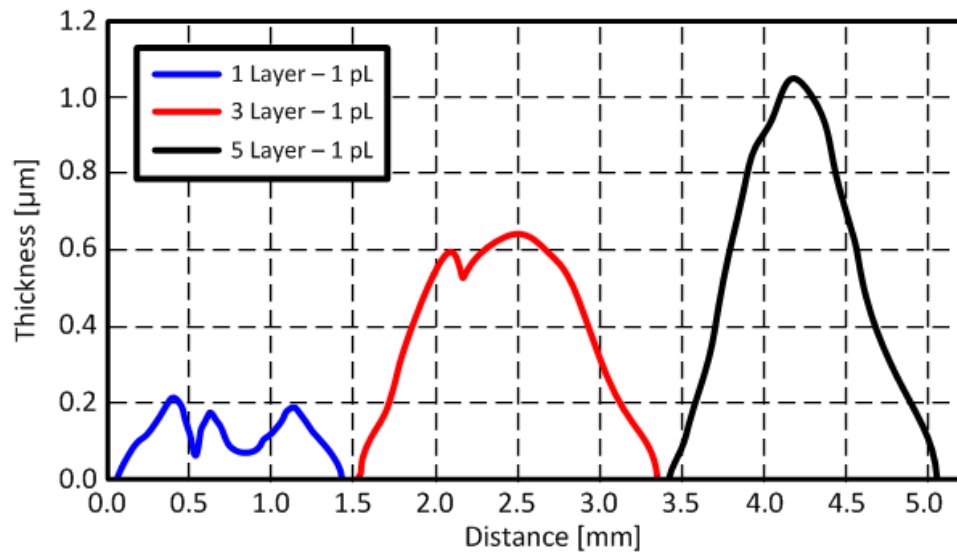


**Figure 2.2** Profiles of inkjet-printed traces: 1 pL.

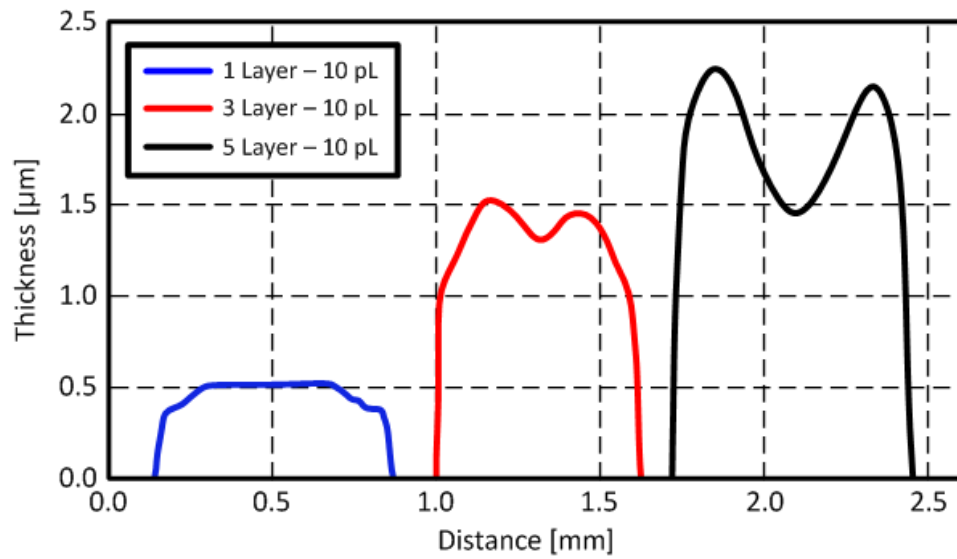


**Figure 2.3** Profiles of inkjet-printed traces: 10 pL.

$$\sigma = \frac{1}{\text{Resistance} \cdot \int (\text{trace height}) dx} \quad (1)$$

**Table 2.1** Conductivity of printed silver nanoparticles.

Layers	Conductivity (S/m)	
	120 °C	200 °C
1	$0.55 \times 10^6$	$1.1 \times 10^6$
3	$1.16 \times 10^6$	$5.56 \times 10^6$
5	$2.16 \times 10^6$	$1.2 \times 10^7$

The extracted conductivities are shown in Table 2.1. The maximum order of the conductivity is  $1.2 \times 10^7$  S/m which is about 18.75 % of bulk silver ( $6.4 \times 10^7$  S/m). This value is almost the same with the conductivity of bulk iron ( $1.04 \times 10^7$ ). As sintering temperature and number of ink layers printed increases, conductivity increases. Higher temperatures increase conductivity by dissolving more of the solvent and further fusing the silver nanoparticles. Printing more layers helps by increasing the density of particles in a given area so that when melted together, the nanoparticles form less of a porous and more of a uniformly solid structure. More layers also increases the thickness of the conductive traces, thus increasing the bulk conductance.

The mechanical properties of the printed silver nanoparticles are shown in [25], which reports that the pull-off breaking force of the sintered silver lines on flexible substrates is about 50 N and its young's modulus is a function of sintering temperature. The reported young's modulus of the printed silver line is about 5 GPa when the sintering temperature is 150 °C and about 52 GPa when the sintering temperature is 200 °C [25]. The humidity affects adhesion strength more so than conductivity. The conductivity difference between the printed silver lines on paper substrate in 30 % and 53 % humidity was only about 2.8 %. However, the adhesion strength of the printed silver lines

decreases dramatically when the substrate absorbs moisture. The reported average pull-off strength of the wet flexible substrate is about 21 N which is much smaller than that of the dry.

### **2.3 Inkjet Printing of Catalyst and Electroless Copper Deposition**

In this section, a method of using a catalyst-based ink to deposit copper which forgoes the use of nanoparticles altogether is proposed. Catalyst-based inks work by forming a seed layer for an electroless growth of copper onto the patterned seed. This eliminates the problems of nozzle clogging (as the catalyst ink is a solution), gaps in the deposited metal, and oxidation (as no sintering or nanoparticle production is required). This also allows the use of substrates which have lower glass transition temperatures and cannot handle thermal sintering or material composites with different coefficients of thermal expansion. This method is also much cheaper and less time consuming than purchasing commercially available Cu nanoparticles, with up to a ten times cost saving.

#### *2.3.1 Palladium-Chloride ( $PdCl_2$ ) Catalyst Ink*

The copper catalyst ink uses palladium (Pd) to form a seed layer for copper growth [26]. Palladium is a well known seed for electroless copper growth, and has the benefit of being able to sustain a continuous electroless deposition as long as copper is available for a reaction to take place [27]. This means thick layers can be deposited if the copper source is replenished during the reaction.

A 10 mg batch of palladium chloride was incubated with 40 mL of anhydrous ethanol at room temperature at 30 rpm for 2 h. The mixture was centrifuged and the supernatant collected. After filtered through a 0.22  $\mu$ m filter, the supernatant was mixed

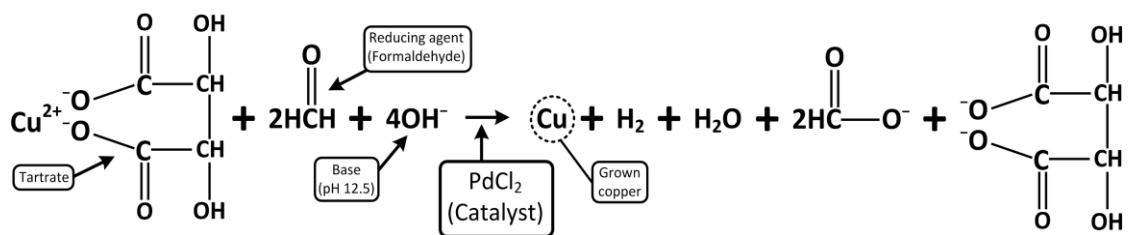


**Figure 2.4** Chemical reaction of catalyst-based electrolessly copper deposition.

with 50 wt% of glycerol to increase its viscosity to approximately 12 cP which is needed for proper jetting using the Dimatix DMP-2800 print nozzle.

The palladium chloride ( $\text{PdCl}_2$ ) catalyst ink is filtered and loaded into the ink cartridge. The DMP-2800, which is a drop-on-demand (DOD) printer, has the option of 1 and 10 pL nozzle cartridges allowing for droplet volume control. Ink-jetting is performed with a cartridge temperature of 37.5 °C to lower ink viscosity with the substrate at 40 °C to aid in quick ink solvent evaporation once the droplets hit the substrate. The printed  $\text{PdCl}_2$  ink is adsorbed and attaches to the surface when the ethanol solvent evaporates. A single layer of catalyst is printed on the substrate at a resolution of 1270 DPI (20  $\mu\text{m}$  drop spacing) to ensure overlapping of the droplets.

Once the catalyst ink is printed on the substrate, the substrate is placed in an electroless copper deposition bath which electrolessly deposits copper on the patterned  $\text{PdCl}_2$  catalyst. The reaction that occurs is shown in Figure 2.4 in which the copper precipitates out upon contact with the palladium seed, and the precipitated copper is then used as a seed for further copper growth [28]. The copper source that is used is an aqueous solution consisting of 0.19 M cupric sulfate and 0.67 M sodium potassium tartrate tetrahydrate with the pH adjusted to 12.5 using an aqueous NaOH solution. This copper source is filtered to remove any particulates activated with 220 mM of formaldehyde.

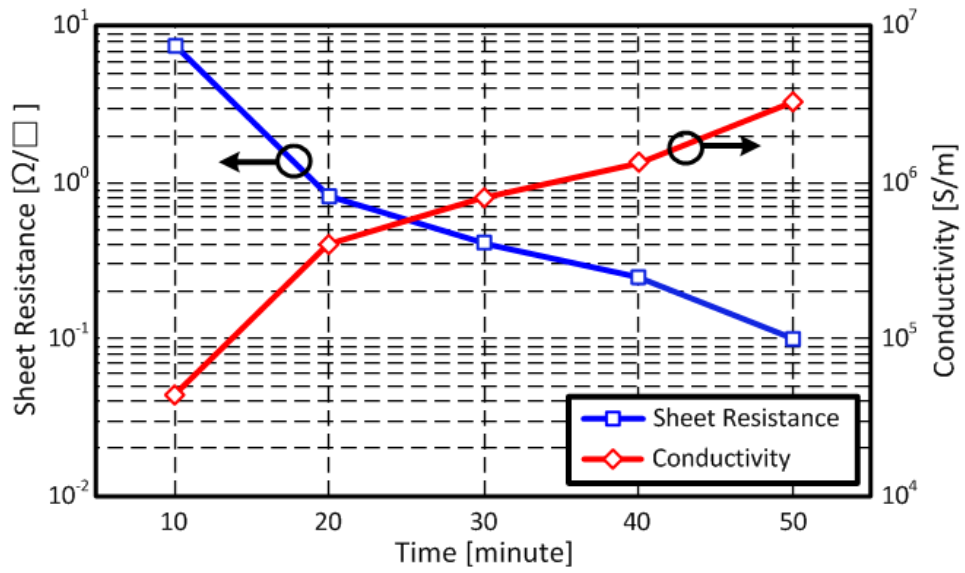


### *2.3.2 Electrical Properties of the Deposited Copper*

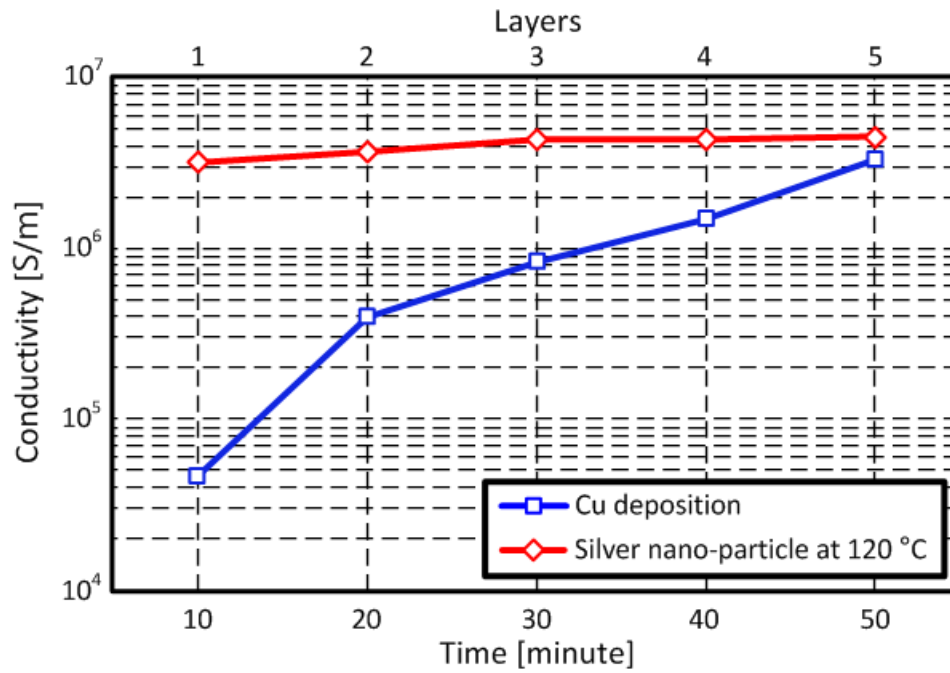
In order to characterize the deposited Cu, test structures are printed using the catalyst ink on commercially available Teslin paper which is a synthetic polymer substrate commonly used for ID cards [29]. Teslin substrate is a polyolefin base blended with silica which is low-cost, non-oil based environmentally friendly, and exhibits much lower loss than standard cellulose based substrates such as photo paper [20]. Electroless deposition is performed on the printed substrates from 10 ~ 60 minutes to determine the optimum deposition time. Theoretically the electroless deposition process should continue indefinitely, but in experiment the copper source or the reducing agent (formaldehyde) will become depleted over time and the deposition rate will slow.

As a comparison, a standard commercially available silver nanoparticle ink Cabot CCI-300 is also used to print the same structures on Teslin paper. After deposition, the sheet resistance of the test traces is measured using the four point probe method. Figure 2.5 shows the electroless copper sheet resistance compared to that of deposited silver nanoparticles. The copper deposition process produces sheet resistances as low as  $0.1 \Omega/\square$  after 50 minutes with no sintering which is similar to three layers of printed silver nanoparticles sintered at  $200 \text{ }^\circ\text{C}$  for one hour. An important point to note is that the sheet resistance of the copper could be further decreased by a longer deposition time. This proves to be a major advantage as the copper deposition process is much low-cost and takes about half the time of the silver deposition process.

From the sheet resistances and thickness measurements, the maximum conductivity is calculated to be near  $1 \times 10^7 \text{ S/m}$  for silver nanoparticles, and  $4 \times 10^6 \text{ S/m}$  for copper, which is approximately ten times less than that of bulk copper. These conductivities,



(a)



(b)

**Figure 2.5** Sheet resistance and conductivity: (a) deposited copper and (b) conductivity of the deposited copper and inkjet-printed silver nanoparticles.

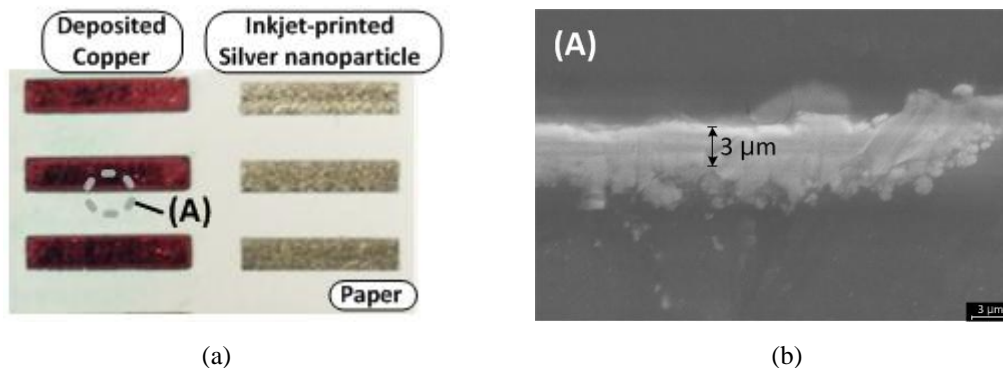


**Figure 2.6** Deposited coppers and cross section: (a) Deposited copper and inkjet-printed silver nanoparticles and (b) a cross section of the deposited copper layer.

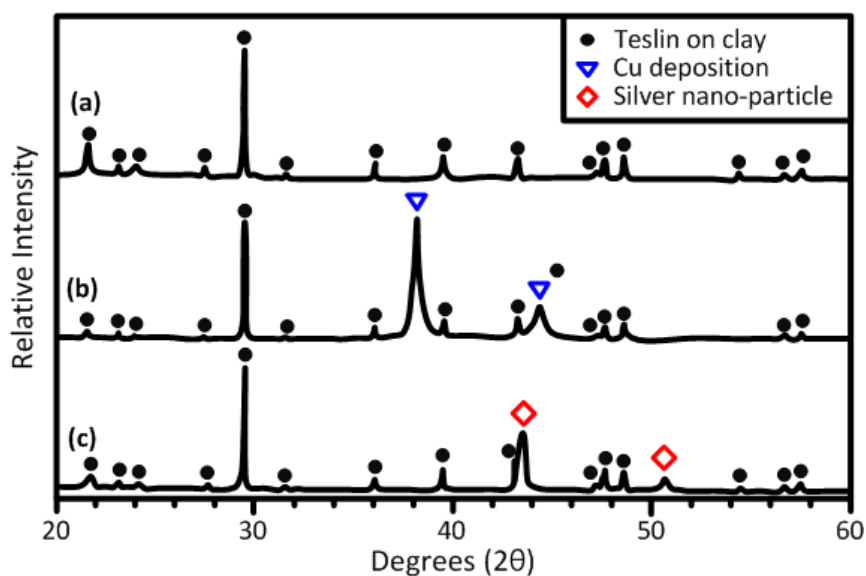
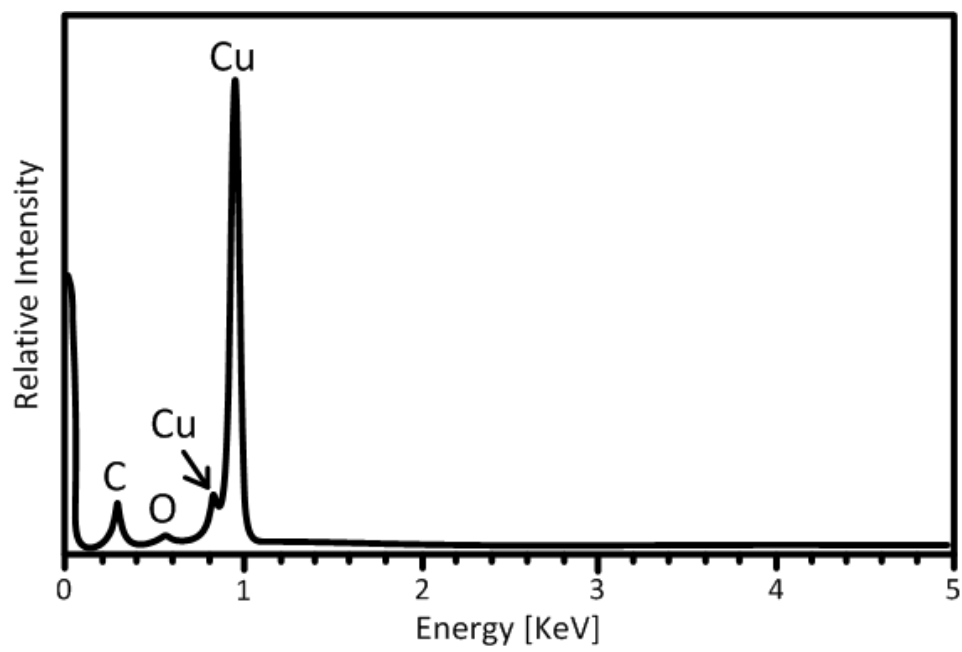


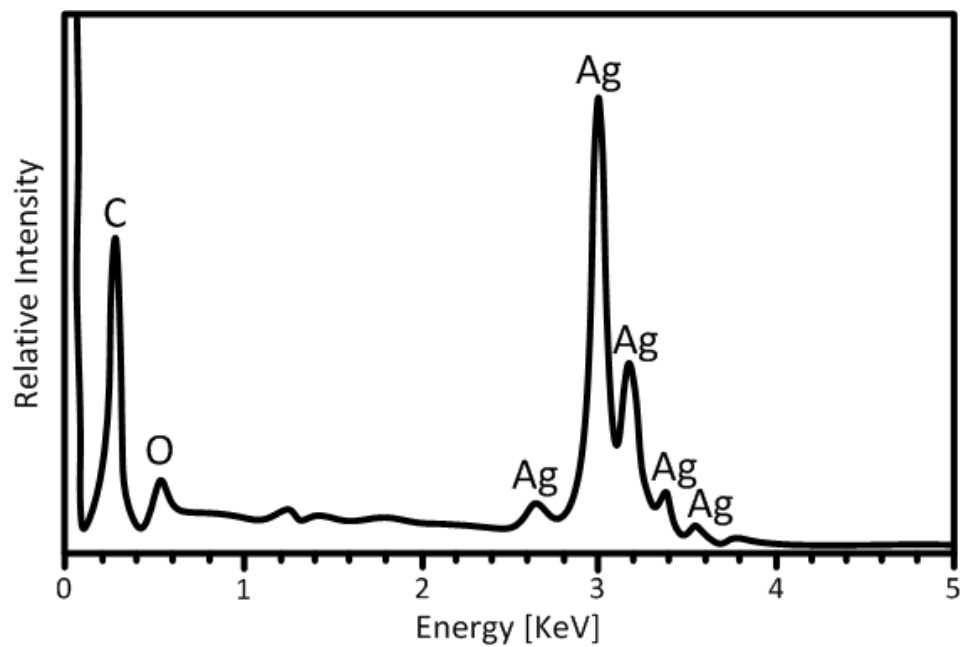
**Figure 2.7.** XRD analyses of Teslin paper: (a) Teslin paper held on a clay backing, (b) deposited copper film on Teslin paper, and (c) printed silver nanoparticles.

however, are sufficient for producing efficient microwave components such as filters and antennas. Figure 2.6 shows the deposited copper and the printed silver nanoparticles. A thickness of the deposited copper for 50 minutes is about 3 μm as shown in Figure 2.6(b).

X-ray diffraction (XRD) and energy dispersive x-ray spectroscopic analysis (EDX) are performed on the copper samples as shown in Figure 2.7. In order to keep the thin and flexible Teslin paper flat for XRD analyses, the control (no copper) and patterned specimen were placed on sticky clay and pressed down with a plain microscope slide



(a)



(b)

**Figure 2.8.** EDX analyses of samples: (a) Figure 2.7(b) and (b) Figure 2.7(c).

until the top surface of the sample is level with the top edges of the sample holder. As a result, the clay used to secure the specimen also contributes to the resulting XRD patterns. Figure 2.7(a) shows the control XRD pattern of blank Teslin paper and the clay, while the lower pattern (Figure 2.7(b)) shows the XRD pattern of Teslin paper with patterned copper printed on it and the clay. Comparing the upper and lower XRD patterns of Figure 2.7, it can be concluded that the printed copper pattern is composed of copper only, with no copper oxides ( $\text{Cu}_2\text{O}$  or  $\text{CuO}$ ) being detected. The same results are present in the EDX measurements in Figure 2.8.

## **2.4 Summary**

In this chapter, the cost efficient additive metallization processes such as nanoparticle inkjet printing and catalyst-based copper deposition are discussed. The inkjet printing technology is a cost-efficient environmentally friendly fabrication method and there are many types of electronic materials such as polymer and carbon-based materials that can be printed. The inkjet-printed silver nanoparticles have a high conductivity value which is as high as a bulk iron. The conductivity value is extracted experimentally utilizing a digital multimeter and profiles of printed traces. The surface roughness is on the order of a nano-meter so that the inkjet-printed silver nanoparticles can be utilized to implement mmWave applications. The catalyst-based copper deposition is much low-cost process than the inkjet printing process and its electrical properties are as good as inkjet-printed silver nanoparticles. The conductivity is high enough to implement microwave components such as antennas and filters. The robustness of the deposited copper layer is experimentally verified through XDR and EDX. The electrical properties of these additive processes are fundamental to design RF circuits and

components which are critical to implement the autonomous printed wireless sensor platform.

## CHAPTER 3

### LOW-COST SUBSTRATES

#### 3.1 Introduction

Selecting proper substrate materials depending on applications is one of the most important design steps in microwave design because the substrate material determines relative dielectric constant ( $\epsilon_r$ ), loss ( $\tan \delta$ ) and flexibility. The impedance of transmission lines, such as microstrip line and co-planar waveguide (CPW), is a function of the relative dielectric constant ( $\epsilon_r$ ) and thickness of the substrate as well as its physical dimensions. Therefore, the dimensions of transmission lines like the width of conductors are decided by the substrate material. For compact system integration, a substrate which has a high relative dielectric constant ( $\epsilon_r$ ) is preferable since increased capacitances of the overall microwave circuit components result in small feature sizes and low radiation losses. Otherwise, a material with low relative dielectric constant ( $\epsilon_r$ ) is a good substrate for structures for radiation like antennas or RFIDs. The thickness of the substrate is also an important design parameter. It is directly related to the effective relative dielectric constant ( $\epsilon_{\text{eff}}$ ) which affects resonance frequency as well as feature sizes of the structures on the substrate. It is obvious that the resonance frequencies or poles of RF components like antennas or filters change depending on effective relative dielectric constant ( $\epsilon_{\text{eff}}$ ), which is function of substrate height. In addition, directivity of antennas is affected by the thickness of the substrate because the radiated wave tend to propagate to a material with high dielectric constant ( $\epsilon_r$ ) which results in uneven radiation pattern as the substrate thickness is getting larger. The loss of the substrate should be considered when the

substrate is chosen, too. The loss of the substrate may limit microwave circuit designs since some kinds of designs are not compatible with high loss substrates like a cavity filter or an antenna which has a high-Q factor. The loss of the substrate can be reduced by utilizing a thin substrate but sometimes it may introduce a fabrication limitation due to stability. For flexibility, the thickness and the natural property of the substrate material are critical. The flexible substrates are preferred for certain applications such as biomedical applications. The material and the thickness should be carefully chosen based on requirements of the desired applications. It is necessary step to decide how much flexibility is required and what kind of structure is suitable on flexible substrate, since the performance of microwave structures is affected by their shape.

Using a proper substrate compatible with the desired application is very important as discussed so far. It is convenient and easy to use well predefined substrate materials but sometime it is necessary to characterize a new material. In this chapter, not only mechanical/electrical properties of popular materials but also various RF characterization methods for unknown materials are presented. Ring- and T- resonator methods for extracting relative permittivity ( $\epsilon_r$ ) and loss tangent ( $\tan \delta$ ) are discussed in detail.

### **3.2 Material Characterization Methods**

Knowing the electrical properties of the substrate is critical to accurate modeling and simulation of microwave devices and antennas, and because of this, substrates must be characterized accurately for permittivity and loss. In this section, several substrate characterization methods utilizing ring- and T- resonators are discussed in detail. High frequency characterization methods utilizing ring- and T-resonators are introduced and the theory for each characterization method is presented. A summary of the electrical and



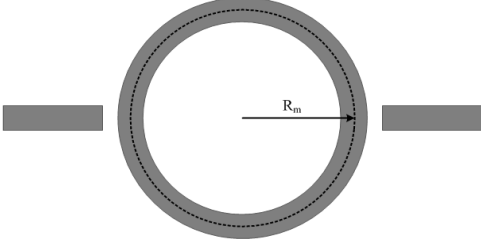
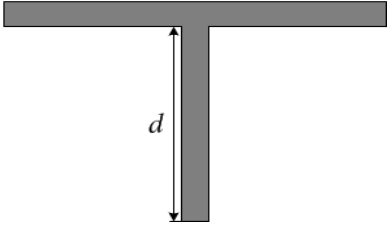
mechanical properties of widely used substrate materials for RF applications is presented at the end of this section.

### 3.2.1 Ring Resonator Method

Resonators offer one of the most precise and popular methods for characterizing RF properties of substrates. The two-port ring resonator method is one of the most popular methods for substrate characterization at high frequency [4,30]. The left column of Table 3.1 shows the structure of a typical microstrip ring resonator.  $R_m$  is the mean radius of the ring resonator to the center of the microstrip line. The most critical design parameter of the ring resonator is  $R_m$ .  $R_m$  determines the dominant resonance mode frequency of the resonator, and periodic higher order resonance frequencies are decided based on the dominant resonance frequency. The ring resonates when the circumference is approximately a wavelength. The wavelength is determined by the effective permittivity ( $\epsilon_{\text{eff}}$ ) of the microstrip line, which is a function of the substrate thickness, the microstrip line width, and the superstrate (air). Because of this, the relative permittivity ( $\epsilon_r$ ) of a substrate can be extracted from the location of those resonance frequencies using the effective permittivity ( $\epsilon_{\text{eff}}$ ). The loss tangent ( $\tan \delta$ ) of a substrate can be extracted from the quality factor ( $Q_0$ ) of the resonance peaks, which is the 3-dB bandwidth of the resonance over the resonant frequency.

$$\epsilon_r = \frac{2\epsilon_{\text{eff}} + M - 1}{M + 1} \quad (3.1)$$

**Table 3.1** Dielectric material characterization methods.

Method	Ring Resonator	T-Resonator
Geometry		
Effective Relative Dielectric Constant ( $\epsilon_{eff}$ )	$\left(\frac{n \cdot c}{4R_m f_n}\right)^2$	$\left(\frac{n \cdot c}{4(d + k)f_n}\right)^2$
Loss Tangent ( $\tan \delta$ )	$\frac{\alpha_d \lambda_0 \epsilon_{eff} (\epsilon_r - 1)}{8.686\pi \epsilon_r (\epsilon_{eff} + 1)}$	

$R_m$ : Mean radius of a ring resonator,  $d$ : Length of a T-resonator,  $n$ :  $n$ -th resonance,  $c$ : The speed of light,  $k$ : correction factor (junction and open stub effect),  $f_n$ :  $n$ -th resonant frequency,  $\alpha_d$ : attenuation coefficient,  $\lambda_0$ : wavelength in free space

$$M = \left(1 + \frac{12h}{W_{eff}}\right)^{-0.5} \quad (3.2)$$

The dielectric constant ( $\epsilon_r$ ) of a material can be calculated from (3.1) and (3.2).  $\epsilon_{eff}$  is the effective dielectric constant of the substrate, and  $W_{eff}$  is the effective width of the ring resonator. The effective width of the microstrip line is discussed in Appendix A. The effective permittivity ( $\epsilon_{eff}$ ) can be derived from the measured resonant frequencies of the ring resonator (3.3), (3.4).

$$f_n = \frac{n \cdot c}{2\pi \cdot R_m \cdot \sqrt{\epsilon_{eff}}} \quad (3.3)$$

$$\epsilon_{eff} = \left( \frac{n \cdot c}{2\pi \cdot R_m \cdot f_n} \right)^2 \quad (3.4)$$

where  $n$  is the order of the resonance ( $n = 1, 2, 3 \dots$ ),  $c$  is the speed of light, and  $f_n$  is the resonant frequency of the  $n$ -th resonant mode.

The loss of the substrate can be extracted from the quality factor of the ring resonator at each resonant frequency. The total loss ( $\alpha_t$ ) includes conductor loss ( $\alpha_c$ ), dielectric loss ( $\alpha_d$ ), and radiation loss ( $\alpha_r$ ) (3.5).  $Q_n$  is the quality factor of the ring resonator at the  $n$ -th resonant frequency and  $\lambda_{eff}$  is the effective wavelength (3.6). The radiation loss ( $\alpha_r$ ) and conductor loss ( $\alpha_c$ ) should be subtracted from the total loss ( $\alpha_t$ ) to calculate dielectric loss ( $\alpha_d$ ). The radiation loss and the conductor loss can be theoretically calculated.

The first step to extract the loss tangent is to calculate the quality factor at the measured resonance frequency as given in equation, (3.7), where IL stands for the insertion loss which corresponds to the magnitude of  $S_{21}$  of the ring resonator at the resonance. The total loss of the ring resonator can be calculated according to (3.5), and the dielectric loss ( $\alpha_d$ ) can be derived when the conductor loss ( $\alpha_c$ ) and radiation loss ( $\alpha_r$ ) are subtracted from the total loss ( $\alpha_t$ ). Finally, the loss tangent ( $\tan \delta$ ) of the substrate can be extracted from (3.8). The unit of dielectric attenuation is Np/m.

$$\begin{aligned}\alpha_t &= \alpha_c + \alpha_d + \alpha_r \\ &= \frac{\pi}{Q_n \lambda_{eff}}\end{aligned}\quad (3.5)$$

$$\lambda_{eff} = \frac{\lambda_0}{\sqrt{\epsilon_{eff}}}\quad (3.6)$$

$$Q_n = \frac{f_n}{BW_{3dB} \cdot (1 - 10^{-\frac{n}{20}})}\quad (3.7)$$

$$\tan \delta = \frac{\alpha_d \lambda_0 \sqrt{\epsilon_{eff}} (\epsilon_r - 1)}{\pi \epsilon_r (\epsilon_{eff} - 1)}\quad (3.8)$$

### 3.2.2 *T-resonator Method*

The T-Resonator, while not as common as the ring resonator in characterization, is much simpler to fabricate as it consists of a microstrip transmission line with an open circuit stub. The structure of the T-resonator is shown in right column of Table 3.1. Due to the open circuit stub with length  $d$ , a null occurs in the transmission whenever  $d$  is an odd multiple of a quarter wavelengths [31], which is caused by the reflected wave being  $180^\circ$  out of phase once it returns from the open end of the stub.

$$f_{r,n} = \frac{n \cdot c}{4d \sqrt{\epsilon_{eff}}}\quad (3.9)$$

The equation for resonance is shown in (3.9), where  $n$  is the resonance index (1, 3, 5, ...),  $c$  is the speed of light in vacuum,  $d$  is the length of the open circuit stub, and  $\epsilon_{eff}$  is the effective permittivity of the microstrip line [31]. However, due to the parasitic effects of the T-junction and fringing fields at the end of the open circuit stub, a correction factor for the length of the stub needs to be incorporated when calculating  $\epsilon_{eff}$ . A method for

doing this is presented in [31]. Shown in (3.10),  $k$  is the correction factor which includes the junction and open circuit effects on the resonant frequency. Using the relations of relative to effective permittivity in a microstrip from appendix A, the permittivity of the substrate can be extracted.

$$\epsilon_{eff,n} = \frac{n \cdot c}{4(d+k)f_{r,n}} \quad (3.10)$$

The Q-factor of the resonance peaks can be used to extract the loss tangent of the substrate. The loaded Q-factor is calculated in (3.11), and then needs to be converted to the unloaded Q-factor (3.12) which de-embeds the loading caused by the measurement equipment [31].

$$Q_{l-n} = \frac{f_{r,n}}{BW_{3dB-n}} \quad (3.11)$$

$$Q_{ul-n} = \frac{Q_{l-n}}{\sqrt{1 - 2 \cdot 10^{-IL/10}}} \quad (3.12)$$

In (3.11),  $Q_{l-n}$  is the Q-factor for the n-th resonance,  $f_{r,n}$  is the resonant frequency, and  $BW_{3dB-n}$  is the 3-dB bandwidth. In (3.12),  $IL$  is the insertion loss at resonance which is used to de-embed the loading effects. The total losses in the microstrip resonator (3.13) can then be extracted [32].

$$\begin{aligned}
\alpha_{tot,n} &= \alpha_{c,n} + \alpha_{d,n} + \alpha_{r,n} \\
&= \frac{8.686\pi f_{r,n} \sqrt{\epsilon_{eff,n}}}{c \cdot Q_{ul-n}} \left[ \frac{dB}{\text{unit length}} \right]
\end{aligned} \tag{3.13}$$

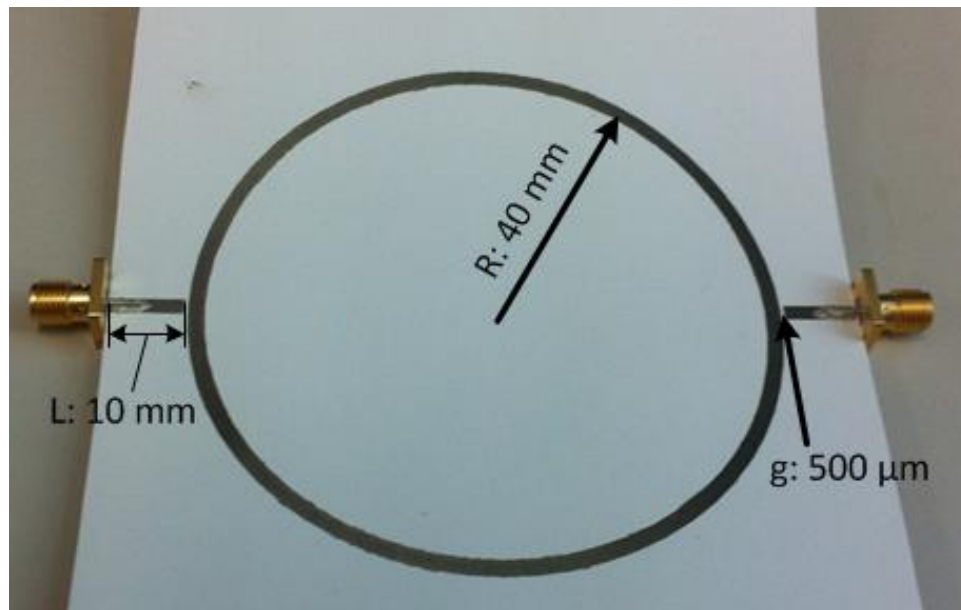
There are a variety of methods to extract conductor and radiation losses, however in this work, Agilent's Line-calc utility is used to subtract these two losses from the total loss leaving only the dielectric losses. The dielectric loss can be directly converted to loss tangent through (3.14) using standard microstrip loss equations given in [33].

$$\tan \delta = \frac{\alpha_{d,n} \lambda_0 \sqrt{\epsilon_{eff,n}} (\epsilon_{r,n} - 1)}{8.686\pi \epsilon_{r,n} (\epsilon_{eff,n} + 1)} \tag{3.14}$$

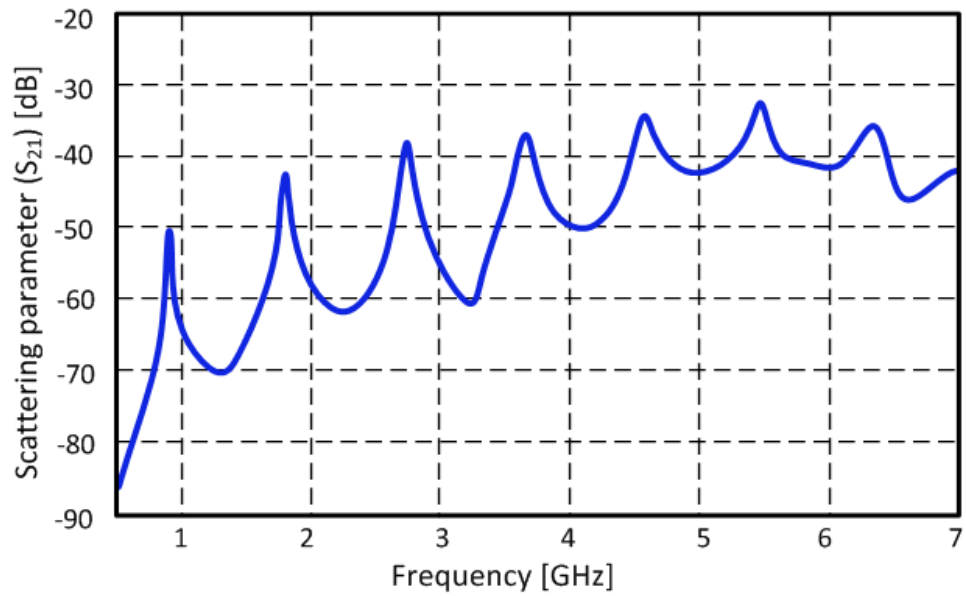
### 3.3 Synthetic Paper: Teslin

Teslin is a flexible and waterproof printing medium for inkjet, laser, and aerosol jet printing. This material is an excellent substrate for wearable RF applications since it is petroleum-free, meaning non-toxic, recyclable, and environmentally friendly. It is widely used in the production of ID and security cards. An inkjet-printed ring resonator is fabricated on a Teslin substrate (Figure 3.1(a)), and its RF properties including relative dielectric constant ( $\epsilon_r$ ) and loss tangent ( $\tan \delta$ ) can be derived from the scattering parameter ( $S_{21}$ ) as shown in Figure 3.1(b).

The ring resonator method is utilized in this section to characterize the Teslin. Figure 3.1 shows the fabricated microstrip ring resonator on Teslin. The width of the microstrip line is 2.2 mm and the substrate thickness ( $h$ ) is 0.76 mm. The length of the feeding lines ( $L$ ) and the gap ( $g$ ) between the feeding line and the resonator are 10 mm and 500  $\mu\text{m}$ ,



(a)



(b)

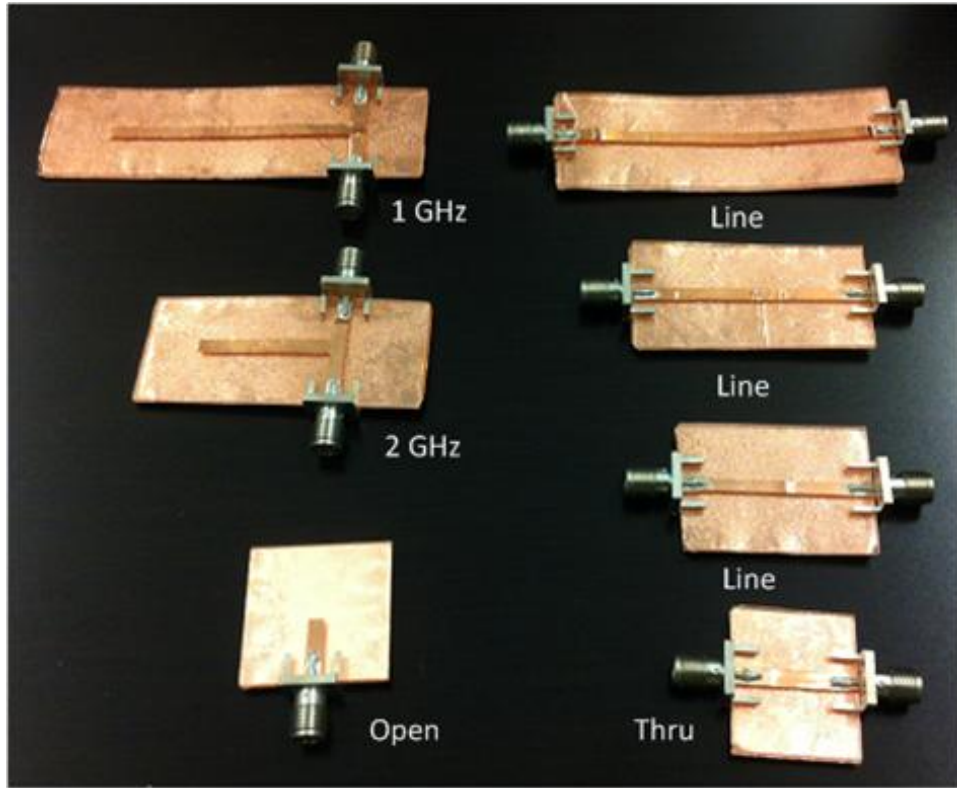
**Figure 3.1** Fabricated ring resonator and measurement: (a) Printed ring resonator for Teslin® characterization and (b) measured  $S_{21}$

respectively. The radius of the ring resonator (R) is 40 mm. The most critical design parameter of the ring resonator is R which determines the dominant resonance mode frequency of the resonator. The ring resonates when the circumference is approximately a guided wavelength ( $\lambda_g$ ). The average value of the dielectric constant ( $\epsilon_r$ ) and loss tangent ( $\tan \delta$ ) of the Teslin are about 2.0 and 0.022, respectively. It should be noticed that the Teslin has relatively low dielectric constant and loss tangent compared to other inkjet-printable low-cost organic substrate such as paper [4].

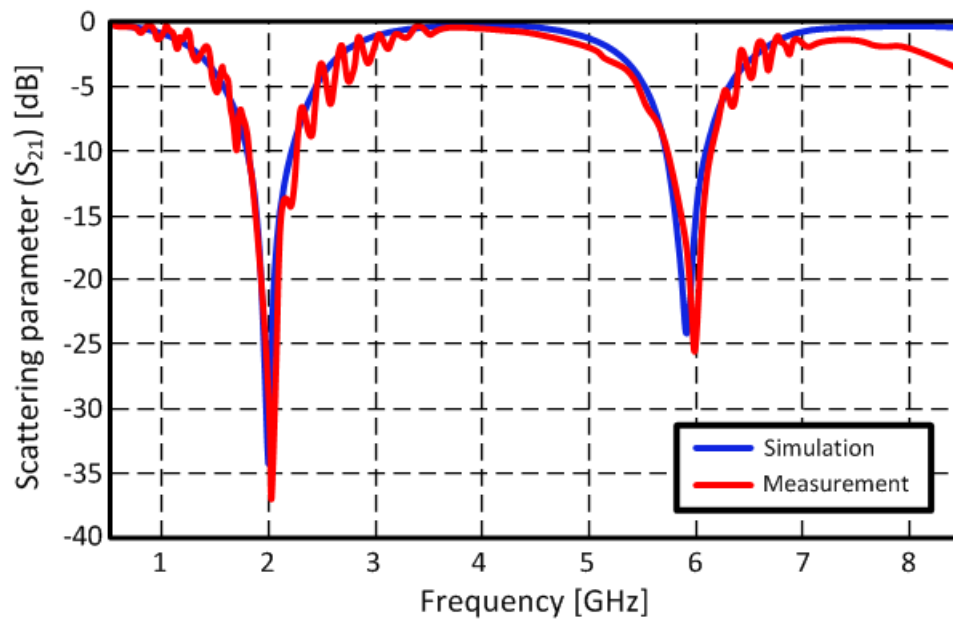
### 3.4 Poly(methyl methacrylate) (PMMA)

A commercially available PMMA (Goodfellow, London, UK [34]) sample has been characterized up to 8 GHz through the microstrip T-resonator method in this work. The relative permittivity ( $\epsilon_r$ ) and loss tangent ( $\tan \delta$ ) have been extracted from the measurements. Figure 3.2(a) shows the fabricated T-resonator structures and the thru-reflection-line (TRL) calibration structures on 1 mm thick PMMA. The T-resonators consist of 50  $\Omega$  feeding lines and an open stub. The length of the open stub is one quarter-wavelength ( $\lambda_g/4$ ) at the desired resonant frequency. The width of the microstrip feeding lines is 2.8 mm and the length of the T-resonator for 1 GHz is 51.92 mm and for 2 GHz is 25.56 mm. The simulated and measured values of  $S_{21}$  of the 1 GHz T-resonator are shown in Figure 3.2(b). The simulations and measurements match very well and odd mode resonances ( $n = 1, 3, 5, 7$ ) are clearly observed. The dielectric constant and loss tangent at each frequency are extracted according to the method discussed in Section 3.2.2. The resulted relative permittivity ( $\epsilon_r$ ) is  $2.38 \pm 0.12$  and the extracted loss tangent is  $0.011 \pm 0.002$  over the frequency of 1 ~ 8 GHz band.





(a)

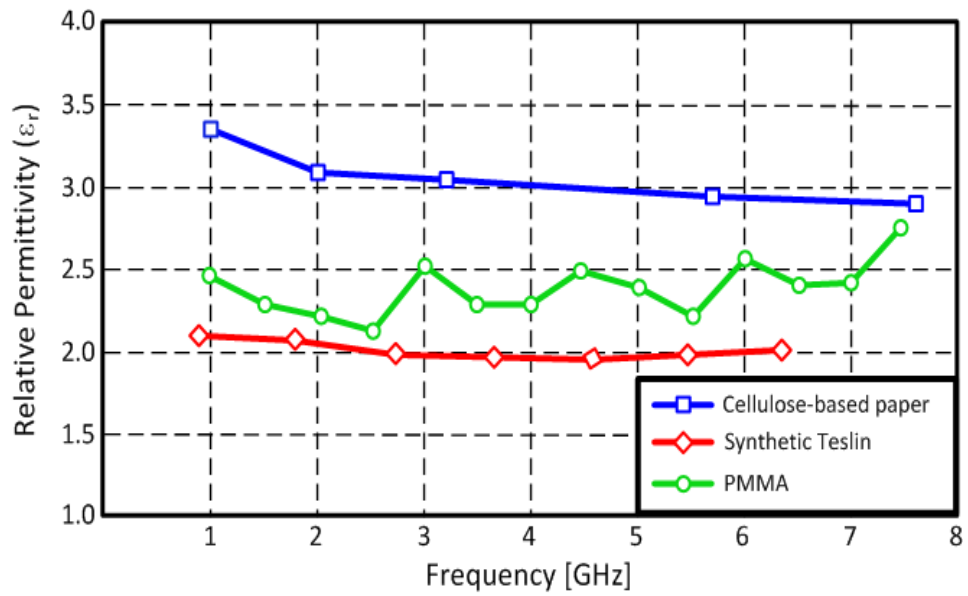


(b)

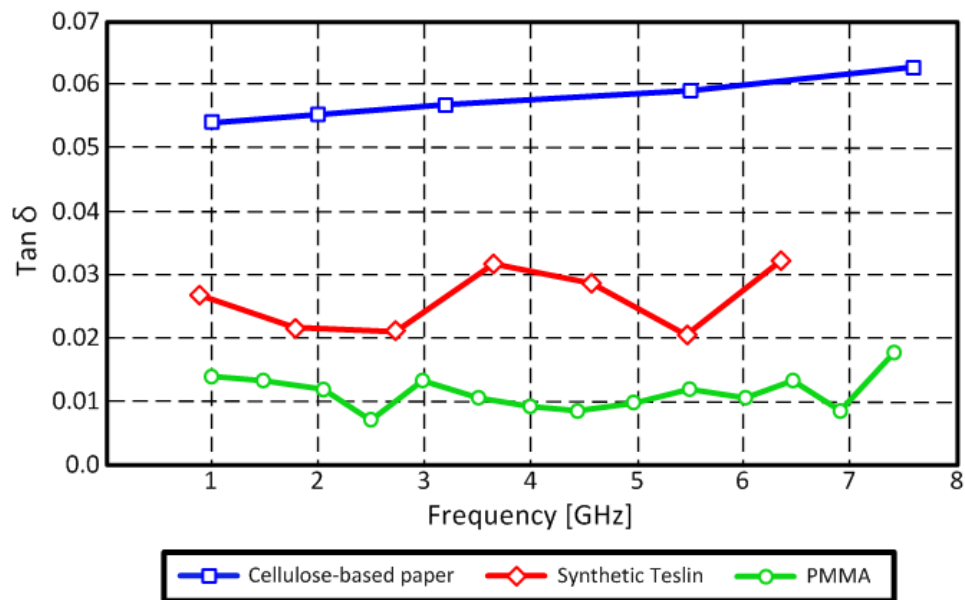
**Figure 3.2** Fabrication T-resonators and measurement: (a) Fabricated T-resonators for PMMA characterization and (b) measured  $S_{21}$

### 3.5 Summary

The material characterization methods utilizing resonators, such as ring- and T-resonator, are discussed. The equations and resonator geometries for extracting relative permittivity ( $\epsilon_r$ ) and the loss tangent ( $\tan \delta$ ) of material are presented and practical examples are also discussed in this chapter. Synthetic Teslin paper and PMMA are characterized and the extracted electrical parameters ( $\epsilon_r$  and  $\tan \delta$ ) are summarized in Figure 3.3. The electrical parameters of a cellulose-based paper substrate are also included for comparison as those substrates are widely used for printed flexible sensors.



(a)



(b)

**Figure 3.3** Extracted relative permittivity and loss tangent: (a) relative permittivity ( $\epsilon_r$ ) and (b) loss tangent ( $\tan \delta$ )

**Table 3.2** Popular materials for RF substrates.

	FR4 [35]	SiO <sub>2</sub>	LCP <sup>2</sup> [33]	PET	Kapton (Polyimide) [36]	Paper [4]	Parylene (N, C) [37]	LTCC <sup>3</sup> [35]	BCB <sup>4</sup> [38]
<b>Relative permittivity (<math>\epsilon_r</math>)</b>	4.0 ~ 5.0	3.9	2.9	3.4	3.4	2.8~3	2.65 (N) 2.95 ~ 3.15(C)	5.7 ~ 9.1	2.5
<b>Loss tangent (<math>\tan \delta</math>)</b>	0.02 ~ 0.03	$2.0 \times 10^{-5}$	$2.0 \times 10^{-3}$	$2.0 \times 10^{-3}$	$2.0 \times 10^{-3}$	0.05 ~ 0.06	$2.0 \times 10^{-4}$ (N) 0.02 (C)	$1.2 \times 10^{-3} \sim$ $6.3 \times 10^{-3}$	$2.0 \times 10^{-3}$
<b>CTE<sup>1</sup> (ppm/<math>^{\circ}</math>C)</b>	14 (x-axis) 13 (y-axis) 175 (z-axis)	0.5	0 ~ 40	6	0.5	-	69 (N) 35 (C)	5.8 ~ 8	0.3
<b>Young's modulus (psi)</b>	$3 \sim 3.5 \times 10^6$	$2.6 \times 10^7$	$1.5 \sim 6 \times 10^6$	$4.0 \sim 4.5 \times 10^5$	$4.6 \times 10^5$	144 ~ 838	$3.5 \times 10^5$ (N) $4.0 \times 10^5$ (C)	$1.7 \times 10^7$	$4.2 \times 10^5$
<b>Water absorption (% after 24 hrs)</b>	0.25	Negligible	0.4 ~ 2.5	0.16	< 0.1	2	< 0.1	Negligible	< 0.2
<b>Compound</b>	Fiber glass, Epoxy resin	Silicon dioxides	Polyester	Polyethylene terephthalate	Polyimide	Cellulose	Para-xylylene	Glass, Ceramic	B-staged bisbenzocyclobutene

CTE<sup>1</sup>: Coefficient of Thermal Expansion, LCP<sup>2</sup>: Liquid Crystal Polymer, LTCC<sup>3</sup>: Low-Temperature Co-fired Ceramic,  
BCB<sup>4</sup>: Bisbenzocyclobutene-based (BCB) monomer

## CHAPTER 4

# PRINTED WIRELESS COMPONENTS FOR AUTONOMOUS SENSOR PLATFORM

### 4.1 Introduction

High efficient autonomous microwave components, such as high gain wearable antennas and RF energy harvesters, are key factors to implement the autonomous wireless sensor platform. The autonomous wireless sensor platform needs to operate in a rugged environment, such as the human body, and also requires a robust power source to drive the whole system.

Wearable devices should be carefully designed because they interact with the human body. The human body affects the wireless electronics, such as antennas, because it is unavoidable for the wireless devices to expose the human body to electromagnetic radiation when they are mounted on the human body. The human body can be considered as a high dielectric material with a poor conductivity value. The poor conductivity value makes the human body a very lossy material, which significantly affects the radiation system of the on-body electronics resulting in a shifted resonant frequency or decreased antenna gain. The radiated waves tend to propagate to a dense material like the human body (high dielectric constant of 52.5), and they are dissipated as heat due to the high loss (low conductivity of 1.78 S/m). This physical phenomenon degrades the wireless performance of the on-body wireless electronics. Therefore, it is important to isolate or minimize the effect of the human body on the wireless system. Bio-compatibility and flexibility of the on-body electronic devices are also important factors as a contour of the

human body consists of curves and a human keeps moving. Wearable device cannot have any hazardous elements which cause health problems or are brittle. In addition, the cost issues with respect to the fabrication process or power efficiency should be accommodated. The Artificial Magnetic Conductor (AMC) plane is introduced to address this issue and its performance is measured in this chapter.

The Power issue is also critical to implement any kind of wireless sensors. A battery can provide sufficient power for most of wireless devices but it is usually bulky and has a finite life time. Also, batteries are not environmentally friendly when exposed to nature for a long time. Therefore, it is necessary to integrate a renewable environmentally friendly green energy source with the wireless sensor platform. A solar module can generate high power to turn-on the wireless sensor devices in daytime but cannot generate power after sunset. The RF energy harvesting technology utilizing antennas and rectifiers is a good power source candidate for the autonomous sensor platform because it generates power independent from the weather and time. However, the efficiency of this technology is low since there is not much available RF power to drive the wireless sensor. Both technologies (solar modules and RF energy harvesting) have trade-offs so that they can compensate for each other.

In this chapter, novel microwave designs for the autonomous wireless sensor system are presented in detail. Design steps and considerations of an antenna on AMC plane for wearable application, a solar-powered active antenna for wireless power transfer (WPT) and multi-band RF energy harvester are discussed.

## 4.2 Inkjet-printed AMC Ground

### 4.2.1 AMC Plane Design

Determining the magnitude and phase response of a Frequency Selective Surface (FSS) unit-cell over a ground plane is the first step to design the AMC. The phase of a reflected wave from the AMC plane is  $0^\circ$ , and the magnitude of reflection coefficient ( $\Gamma$ ) is 0 dB in the ideal case of a lossless AMC. The bandwidth of the AMC plane is determined by the  $\pm 90^\circ$  points in the phase of reflected wave.

It is well known that changing the unit-cell size with respect to wavelength, as well as cell spacing, affects the bandwidth and the resonant frequency. Each structure is illuminated with a normal incidence TEM wave. The geometry of the proposed unit cell is shown in Figure 4.1 [39]. The geometry of the AMC plane is also shown in Figure 4.2(a) and reflection phase of the structure is shown in Figure 4.2(b). To produce the optimized FSS layer for the inkjet printing process using these results, bandwidth, reflection loss, fabrication tolerances, and ink consumption are taken into account. Ink consumption is an important factor when producing low-cost antennas as ink is the highest cost of the entire fabrication process. Here, a single split ring resonator (SSRR) is chosen.

The circumference of the SSRR corresponds to one wavelength ( $\lambda_0$ ) at the central frequency (2.45 GHz), in free space, and the thickness of each side ( $t_2$ ) is adjusted to optimize the resonance frequency at 2.45 GHz. The distance between pins, ( $g$ ) and the cells are selected to be the same as the thickness of the top and bottom sides ( $t_1$ ) for design simplification. For the proposed design, the distance between the FSS structure and the copper sheet is chosen according to the thickness of the commercially available

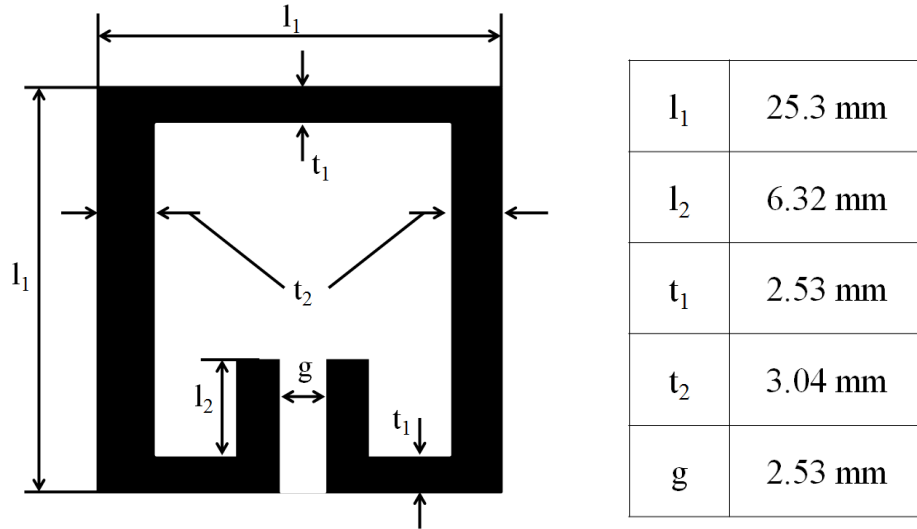
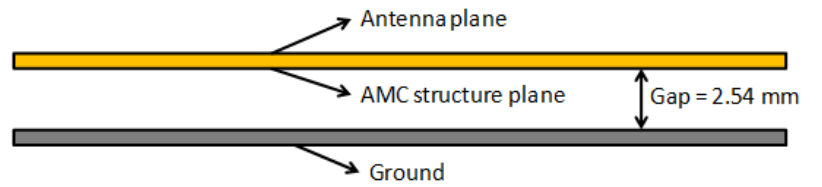
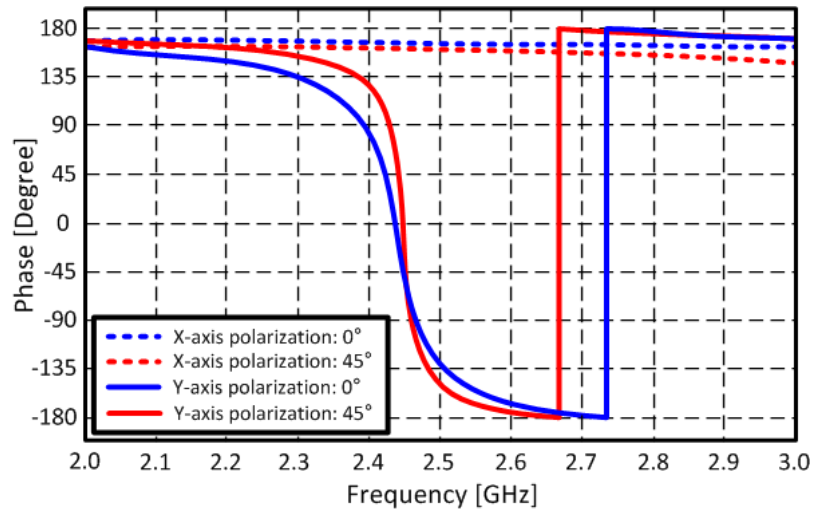


**Figure 4.1** Geometry of the single split ring resonator (SSSR).



(a)



(b)

**Figure 4.2** Geometry and phase response of AMC: (a) Geometry and (b) phase response



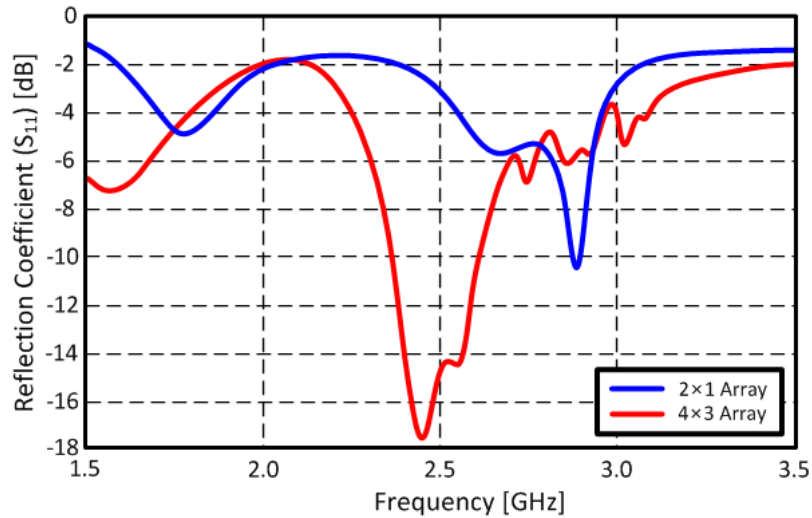


**Figure 4.3** Array size and reflection coefficient ( $S_{11}$ ) variation.

Styrofoam slabs. Figure 4.2(b) shows the calculated phase of the reflection coefficient ( $S_{11}$ ) on the surface of the infinite AMC reflector. The x- (horizontally) and y-axis (vertically) polarized plane waves are illuminated at the angles of  $0^\circ$  and  $45^\circ$  on the AMC plane to investigate its polarization properties. The y-axis polarized plane waves show in-phase responses at 2.45GHz while the x-axis polarized ones have out-of-phase responses. Therefore, the radiated waves from the antenna which have a cross-polarization will be suppressed by the AMC reflector. For the y-polarized wave, the reflection phase is  $0^\circ$  at 2.45 GHz and the reflection phase is between  $-90^\circ \sim 90^\circ$  at 2.4 ~ 2.48 GHz. Within this frequency range, the reflected wave exhibits constructive interference with the radiated wave in free space. However the practical array size needs to be determined since it is impossible to realize the simulated infinite array. A small size is generally desirable, however, the resonating frequency of the microstrip antenna/AMC reflector changes, and the antenna does not operate adequately when the AMC plane is too small. This is because the parasitic capacitance between the antenna and the AMC plane affects the performance of the whole structure. In Figure 4.3, simulated reflection coefficients

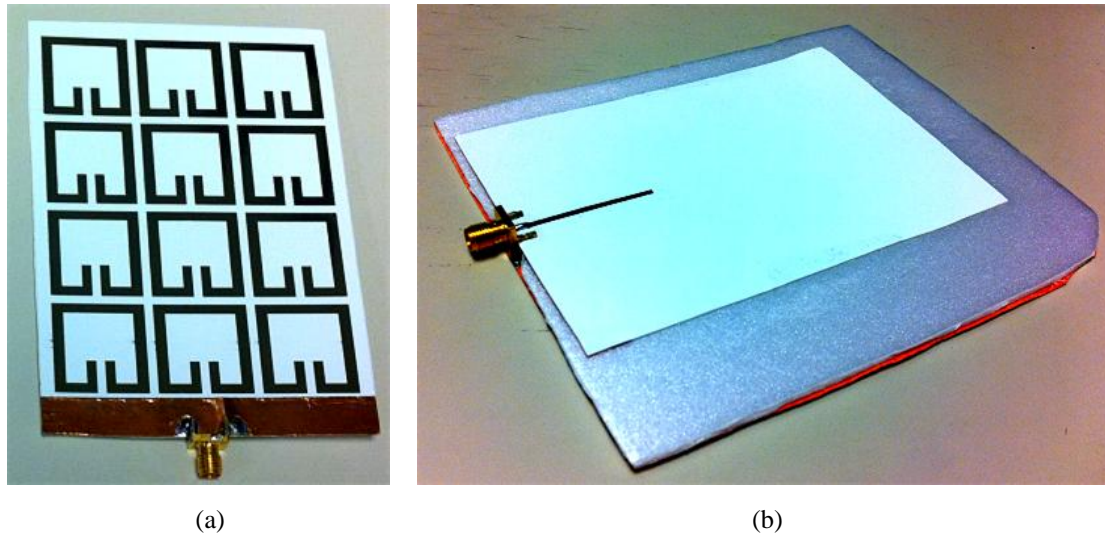
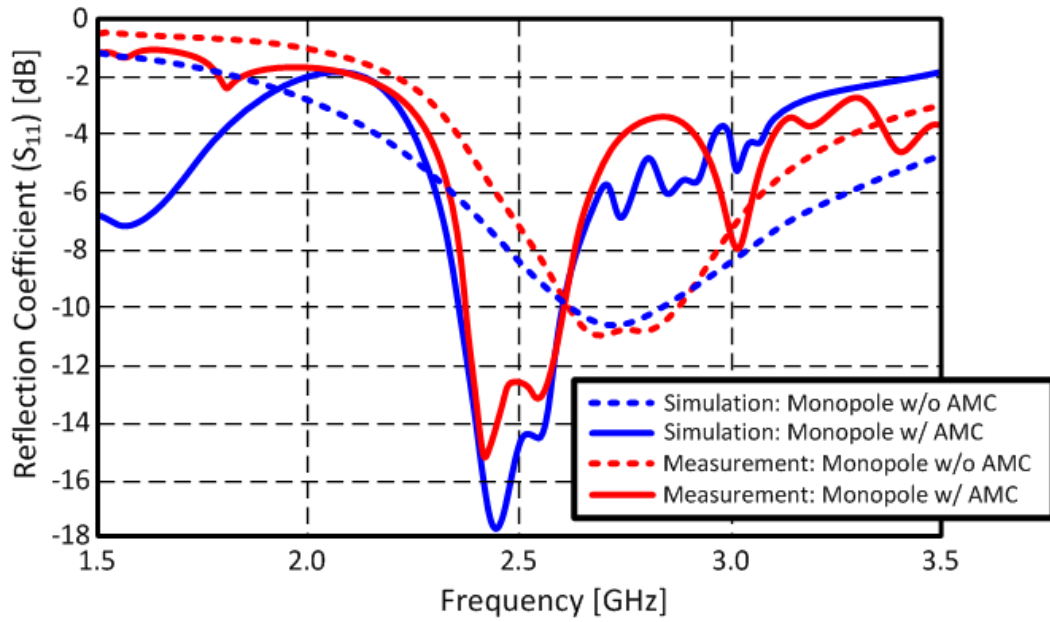


**Figure 4.4** Fabricated antenna: (a) AMC plane (4x3 array) and (b) a monopole antenna on AMC plane.

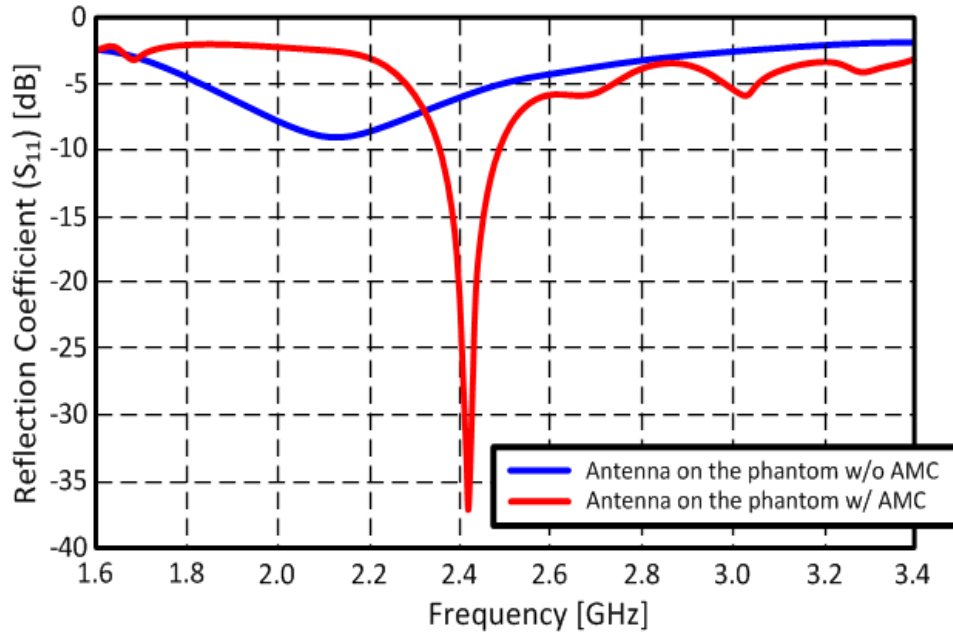
( $S_{11}$ ) of the antenna having different AMC size are presented in order to optimize the size of AMC plane. The  $2 \times 1$  AMC array doesn't cover the desired frequency range of 2.4 GHz ~ 2.5GHz. The antenna has low gain due to mismatch at desired frequency range. The array size is increased by one row and one column at a time until satisfactory performance is achieved. Finally the fabricated  $4 \times 3$  array size was chosen as a compensation between relatively small size and high gain at 2.40 ~ 2.48 GHz. Finally, the size of the copper sheet needs to be determined. A 20 mm wide rectangular of copper sheet is extended from each side of the antenna in order to block the backscattered waves more effectively, resulting in the copper sheet having overall dimensions of 150 mm  $\times$  130 mm as shown in Figure 4.4.

#### 4.2.2 Antenna Measurement

The simulated and measured reflection coefficient of the designed antenna with/without the AMC plane is shown in Figure 4.5(a). The simulation and measurement



(a)



(b)

**Figure 4.5** Reflection coefficient ( $S_{11}$ ) of a microstrip monopole antenna with/without AMC plane: (a) in free space and (b) on a phantom.

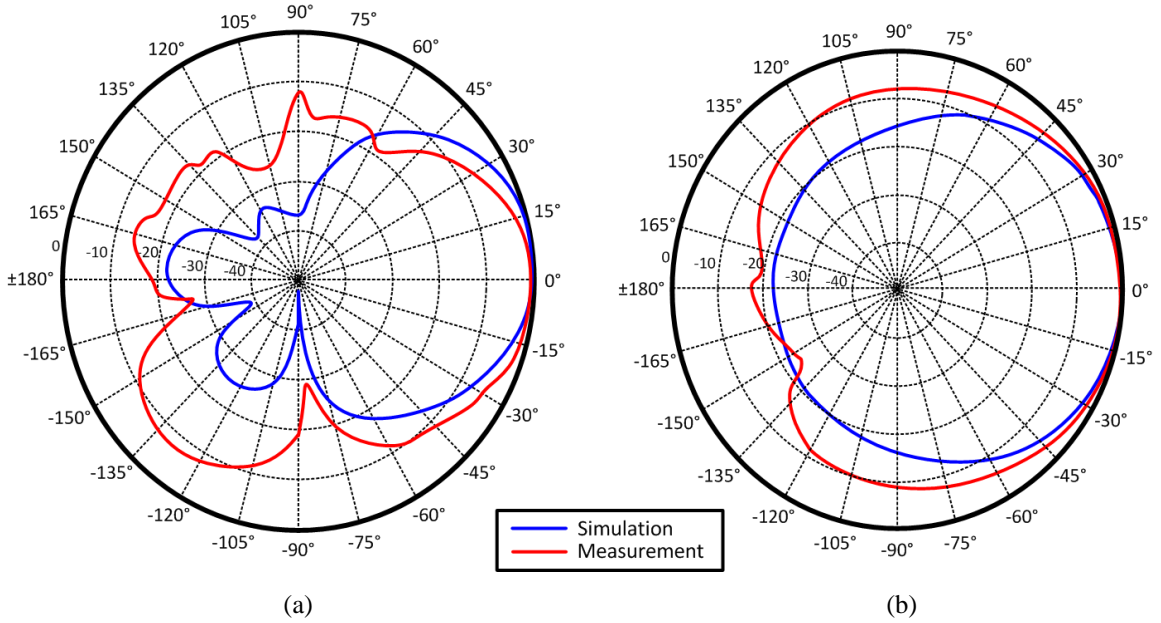


**Figure 4.6** Radiation patterns: (a) E-plane (b) H-plane

match very well and the antenna with the AMC plane has a relatively wide fractional bandwidth of 10.06 %. The antennas with/without the AMC plane were also measured on a human body phantom. The phantom is shaped like a human torso [40] and the antenna is placed in the middle of the phantom’s chest during the measurement. The relative permittivity ( $\epsilon_r$ ) and conductivity ( $\sigma$ ) of the phantom are 35.4 and 1.82 S/m, respectively. Measured reflection coefficients are shown in Figure 4.5(a). The antenna with the AMC plane maintains its resonant frequency while the antenna without the AMC plane is significantly affected by the phantom. The measured radiation patterns and realized gains are also shown in Figure 4.6 and Figure 4.7, respectively. It should be noted that the human body phantom deteriorates the gain of the antenna when the AMC is not implemented. The measured antenna gain with the AMC plane on a human body phantom is about 8 dBi higher than the gain of the antenna on the phantom without the AMC plane.

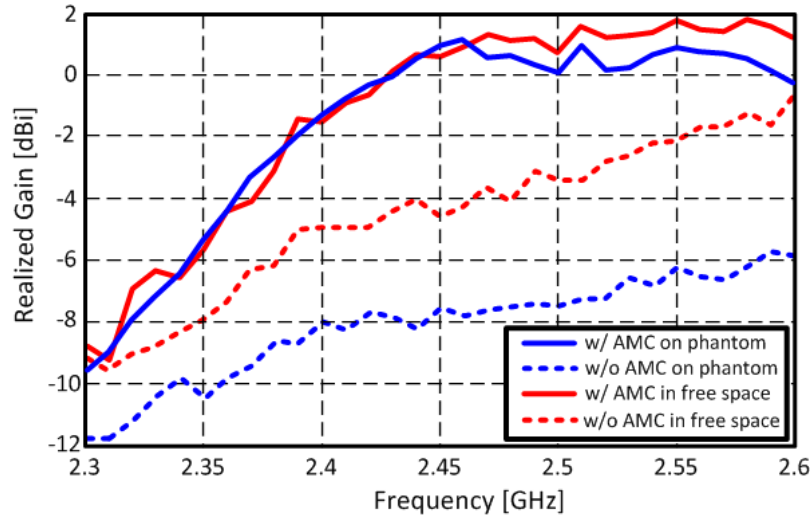


**Figure 4.7** Measured antenna gain

### 4.2.3 Communication Range Measurement

The monopole antenna on an inkjet-printed AMC plane is integrated with a commercial temperature sensor (Texas Instrument, eZ430-RF2500), and the complete system is mounted on the human chest [41] in order to demonstrate the antenna performance. For the monopole antenna, the transmitter was mounted on the chest, and the communication distance was defined as the distance when the receiver lost signal from the transmitter. The communication range of the on-body sensor module with a conventional chip antenna was 18.3 m, and it was 29.3 m with a printed meandered monopole antenna. However, the communication range was 82.8 m with the proposed antenna with the AMC plane as shown in Figure 4.8.

## 4.3 Inkjet-printed Beacon Oscillator

### 4.3.1 Passive Antenna Design and Measurement

The antenna design for a beacon oscillator should satisfy five conditions: simple layout, ease of integration with solar panels and active circuitry, omni-directional radiation pattern, frequency tuning capability or broadband performance, and mechanical

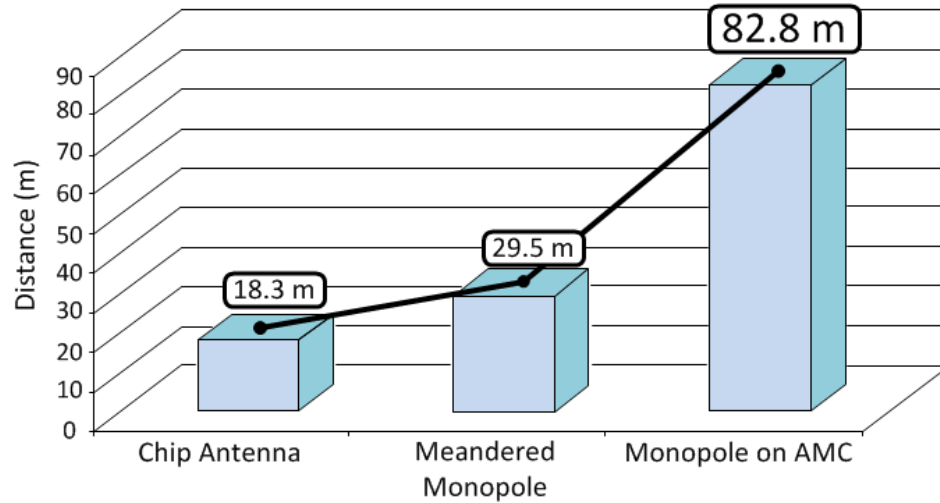


**Figure 4.8** Communication range comparison on body

flexibility. The first requirement allows low-cost, large volume production required for RFID or wireless sensor network applications. Coplanar waveguide technology utilizes a single conductive layer and therefore it is preferred to microstrip technology in terms of fabrication simplicity. Integration of solar panels with antennas allows for area reduction and consequently cost reduction. Slot antennas require a large ground plane, which is advantageous for solar cells as well as additional circuitry integration. Frequency tuning or broadband characteristic is sought in order to easily reconfigure the antenna to cover different frequency bands depending on geographic location or specific applications. Mechanical flexibility is desired in order to easily place the antenna on rugged structures.

Taking into account the above requirements a coplanar waveguide (CPW) slot antenna topology on a flexible paper substrate was chosen. A folded CPW multi-slot structure was selected because it provides the flexibility to achieve the desired impedance over a wider frequency range compared to a single slot antenna [42]. In a previous design [43], a grounded folded slot structure was used following [44], which allowed for a slight reduction in antenna size while somewhat reducing bandwidth and antenna efficiency. In

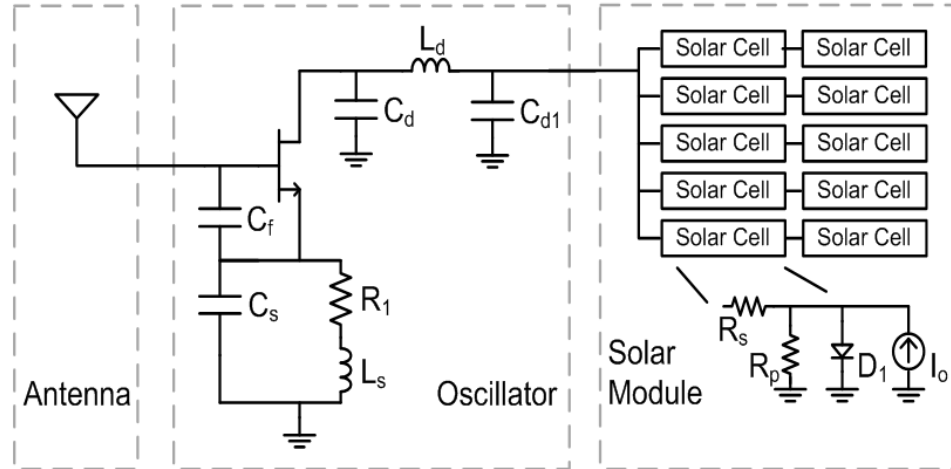


**Figure 4.9** Circuit schematic

this work, the shorting strip was not used, since size reduction was not a critical design goal, and furthermore, the folded slot structure provided sufficient bandwidth.

The antenna is the output load of the oscillator, as shown in Figure 4.9, as well as a resonator effectively controlling the oscillation frequency. The broadband folded slot antenna configuration was chosen due to its stable input impedance throughout its operation frequency range, effectively facilitating the design of the oscillator and enhancing its stability. In addition, it is common in wireless modules operating in rugged environments that the antenna resonant frequency may shift because of the surrounding environment. The oscillator can be minimally affected by this phenomenon by using a broadband antenna with relatively small input impedance variability contrary to narrow band antennas, such as patch antennas. Additionally, the active antenna will be still able to operate even in the case that the oscillation frequency may vary. Therefore, the proposed active antenna can generate a robust power level regardless of the ambient environment which is a critical feature in identification and power transmission applications.

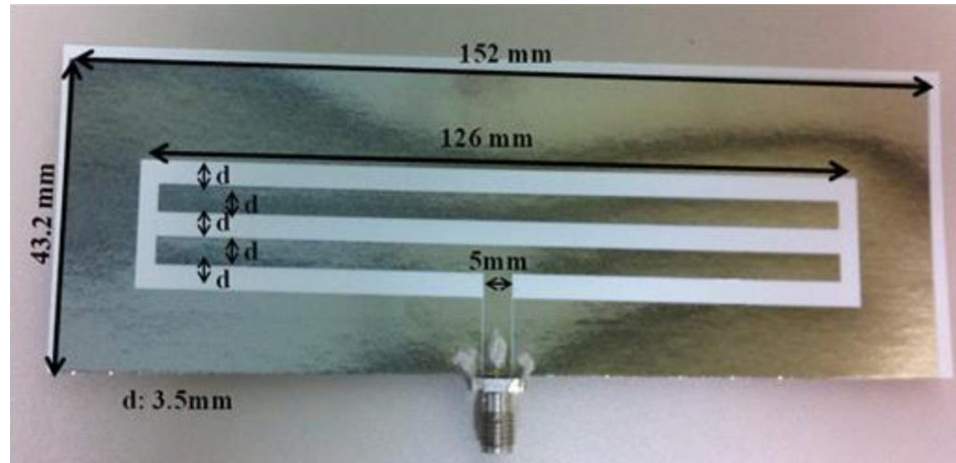


**Figure 4.10** Folded slot antenna (gap of the CPW line 0.2 mm)

Figure 4.10 shows the fabricated passive antenna with the corresponding dimensions. The slot length is 126 mm, and its width is 3.5 mm. The overall length of the antenna is 152 mm, width is 43.2 mm and thickness of the paper substrate is 228.6  $\mu\text{m}$ . The antenna is fed by a CPW line with 5 mm of signal line width and 0.2 mm of ground-to-signal line gap.

A full wave Finite Element Method (FEM) software tool (Ansys HFSS v11.1) was used to design and simulate the passive antenna. Simulated and measured results of the reflection coefficients ( $S_{11}$ ) of the antenna are presented in Figure 4.11, showing a good agreement over a bandwidth of approximately 41.5%. The antenna gains in free space and on the human body were evaluated in an anechoic chamber and a value of approximately -6 dBi at 960 MHz was measured, as shown in Figure 4.12. The gain of the antenna on the human body is about -5dB ~ -10 dB lower than that of the antenna in the free space due to the effect of the lossy human body. The obtained low gain is mainly attributed to the limited dimensions of the ground plane. Fluctuations in the measured gain profile and variation with respect to the simulated values are attributed to the outdoor setup measurement error.



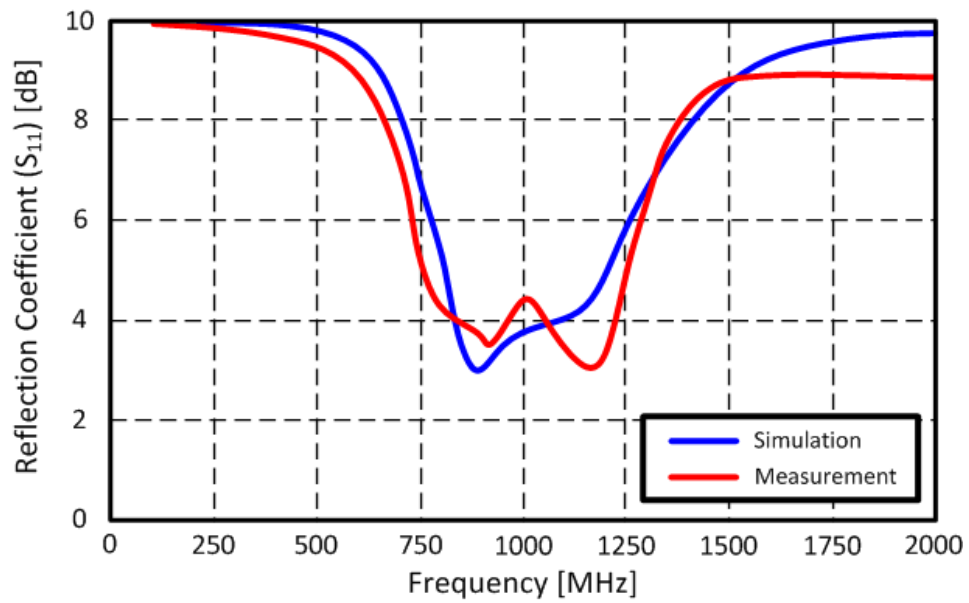


**Figure 4.11** Reflection coefficient ( $S_{11}$ ) of the folded slot antenna

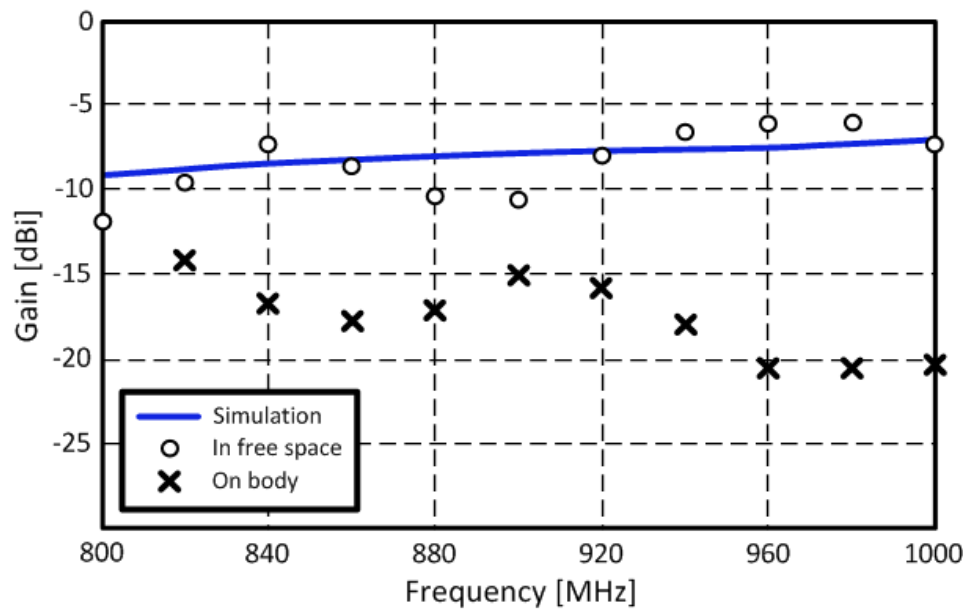


**Figure 4.12** Measured antenna gain

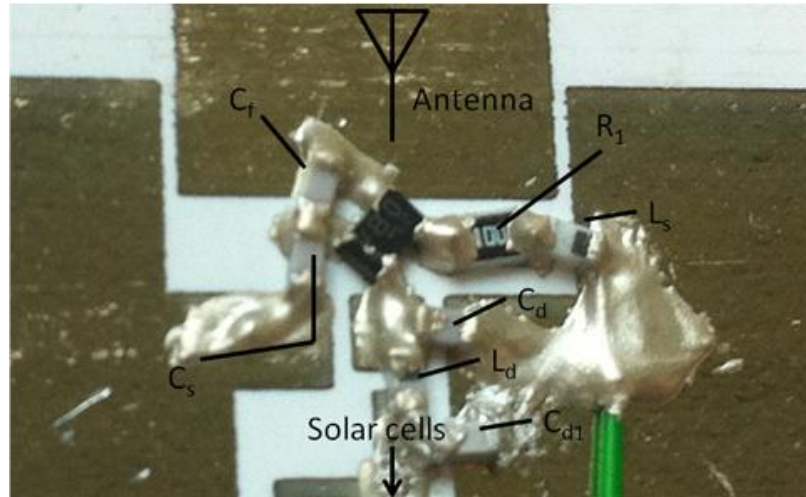


**Figure 4.13** Fabricated Circuit

#### 4.3.2 Active Antenna Oscillator Design

An active oscillator antenna combines an oscillator circuit with a passive radiating structure [45]. It allows for a simple circuit layout, utilizing one active device and a minimum number of passive components, which can be integrated on the antenna structure. In this work, the ground plane surrounds the radiating slot resulting in a low profile circuit design.

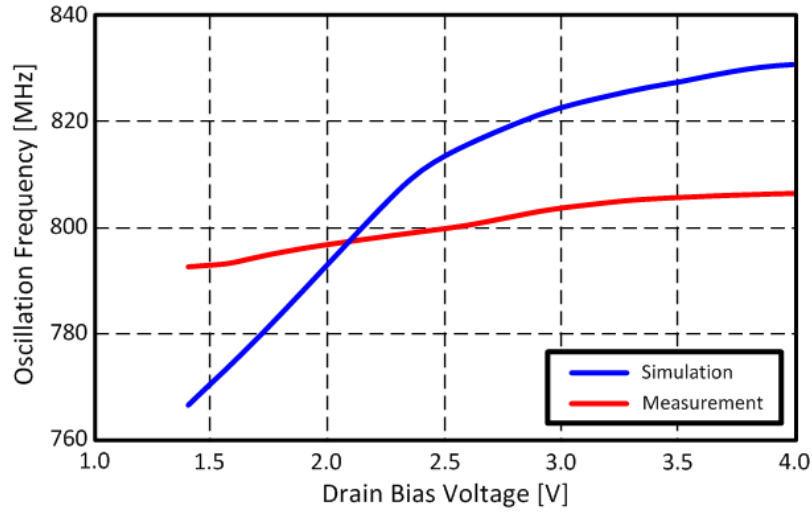
The oscillator circuit was designed using the NE3509M04 pHEMT. A one stage reflection type oscillator topology was selected with a simple passive LC tank ( $C_s$  and  $L_s$  in Figure 4.9). A multistage oscillator or an oscillator with a Phase Locked Loop (PLL) may increase the frequency stability of the active antenna oscillator, however such designs lead to an increased circuit complexity and power consumption, which are undesired in beacon circuits for identification and wireless power transfer applications. The designed oscillator is shown in Figure 4.13. The antenna is connected to the gate terminal of the active device, while a source resistor  $R_1$  is used to self-bias the device. Capacitors  $C_s$ ,  $C_f$  and  $C_d$  and inductors  $L_s$  and  $L_d$  tune the oscillation frequency around

**Table 4.1** Circuit component values.

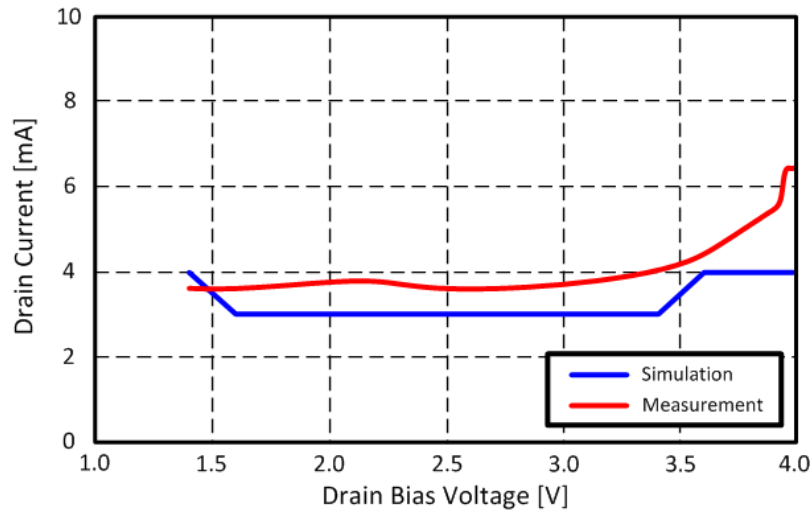
<b>Part</b>	<b>Value</b>	<b>Tolerance</b>
$C_d$ (pF)	1.5	$\pm 0.1$ pF
$C_{d1}$ ( $\mu$ F)	1.0	$\pm 10$ %
$L_d$ (nH)	12.0	5 %
$C_s$ (pF)	3.3	$\pm 0.1$ pF
$C_f$ (pF)	3.3	$\pm 0.1$ pF
$R_1$ (Ohm)	10.0	5 %
$L_s$ (nH)	18.0	5 %
$f_{osc}$ (MHz)	$\sim 800$	$\square$

800 MHz. Capacitor  $C_{d1}$  provides an RF short and isolates the DC feed from the oscillator circuit. The oscillator was initially designed without the solar cell power supply, using an operating DC power supply (HP/Agilent E3620A) voltage of 1.8V, and drawing a current of 4 mA. A commercial harmonic balance simulator (Agilent ADS) was used to simulate the oscillator circuit. A prototype oscillator was built and its performance was characterized. The frequency of the oscillator is in good agreement with simulation within an expected yield variation of the off-the-shelf component values (Table 4.1).

The oscillation frequency increases with the bias voltage as shown in Figure 4.14(a). Measurement of the oscillator frequency was made by capturing the radiated spectrum of the oscillator using a commercial broadband antenna and a spectrum analyzer. The frequency variation with the bias voltage can be utilized as a frequency tuning mechanism or alternatively it can be minimized by placing a regulator circuit following the DC supply. The fabricated prototype frequency was less sensitive to bias voltage variation than in simulation. This difference can be attributed to yield variations of the components and to associated layout parasitics not taken into account in the



(a)



(b)

**Figure 4.14** Active oscillator antenna performance versus DC-bias voltage: (a) Oscillation frequency and (b) current consumption.

simulation stage. In addition, the discrepancy of simulation and measurement in Figure 4.14(a) also result from imperfect modeling of active/passive devices like transistors, inductors and capacitors. Additional parasitic effects such as capacitances and inductances from the surface mount components significantly affect the oscillation frequency of the circuit. And the comparatively low conductivity of inkjet-printed silver traces is also one of the most significant error source. the actual oscillation

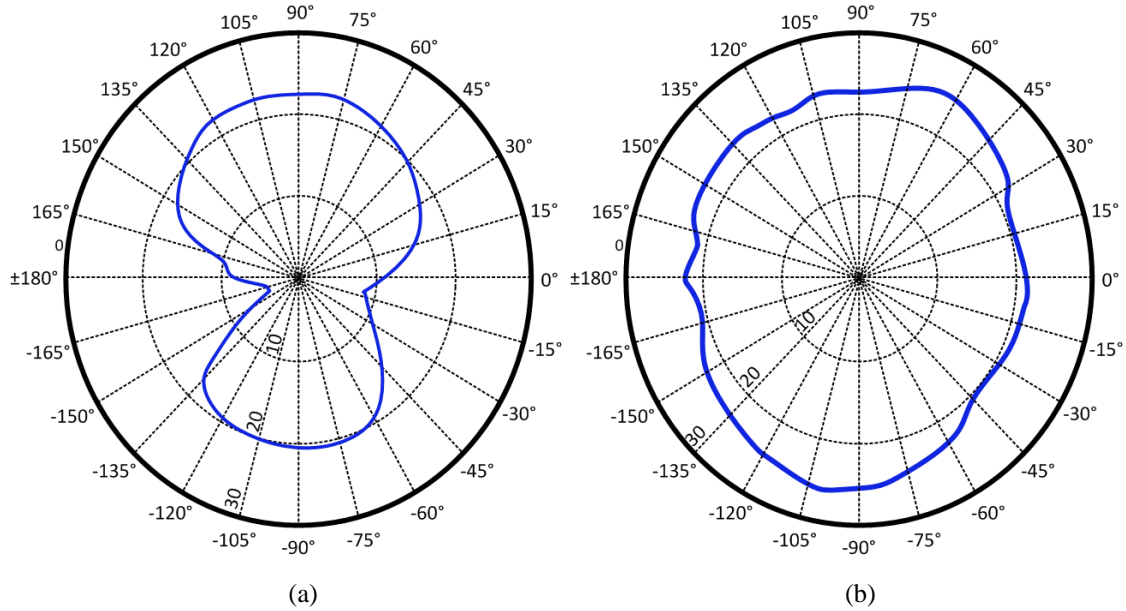
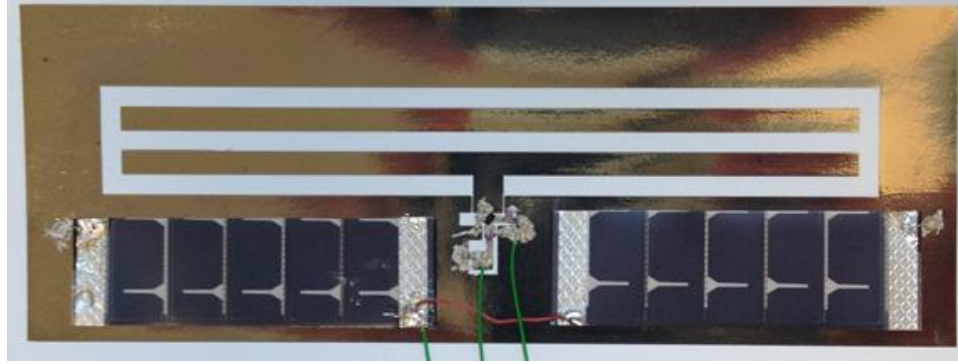
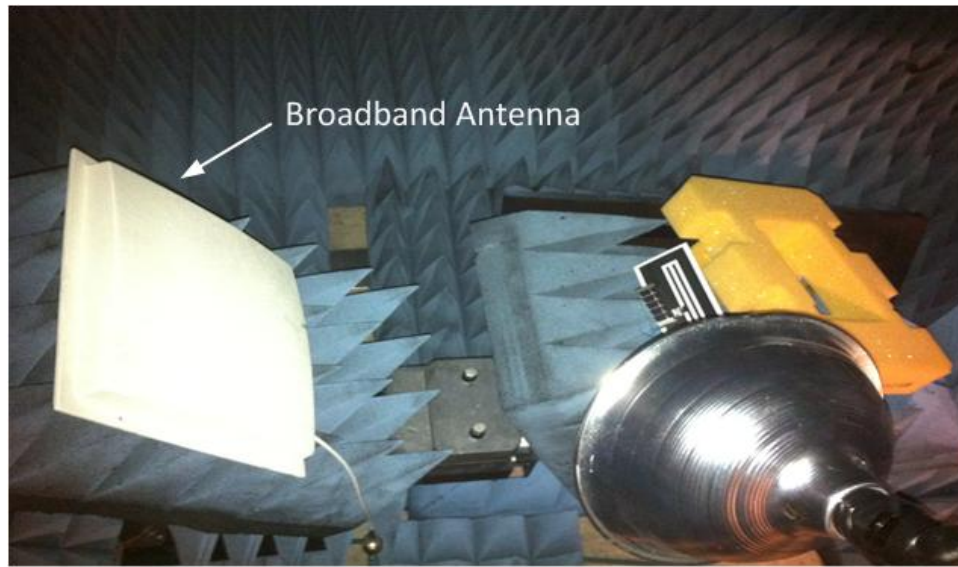


**Figure 4.15** Measured EIRP (dBm): (a) E-plane (b) H-plane

frequency is lower than the simulated value because the increased resistance and conductor loss cause an additional loading effects beside unwanted parasitic effect of the transistor. The measured oscillator drain current was approximately 4 mA for bias voltages up to 4.0 V (Figure 4.14(b)). Correspondingly, the DC power of the oscillator increases from 5.6 mW to 16 mW as the supply voltage ranges from 1.4 V to 4.0 V (Figure 4.14). The voltage regulator dissipates power about 1.2 mW ~ 8.8 mW as the supply voltage ranges from 2.1 V ~ 4 V. Measured EIRP (dBm) patterns of the active antenna oscillator are shown in Figure 4.15 showing a good agreement with the radiation patterns of the passive antenna as expected. The maximum EIRP on E-plane and H-plane is 22.88 dBm and 25.98 dBm while the minimum EIRP on both planes is 3.91 dBm and 20.34 dBm, respectively.



(a)



(b)

**Figure 4.16** Solar-powered active antenna: (a) fabricated prototype and (b) indoor measurement setup using a halogen lamp.

#### *4.3.3 Solar Power-enabled Autonomous Active Antenna*

Autonomous operation of the active antenna was achieved by utilizing amorphous silicon (a-Si) solar cells to harvest light energy as shown in Figure 4.16. One of the biggest challenges when integrating solar cells together with antenna elements is to select the optimum placement of the solar cell in order not to degrade the performance of the antenna. It is known in the literature that the solar cells have little effect on the radiation and input impedance characteristics of the antenna when properly placed, such as

covering areas where the antenna field distribution is weaker [46]. Additionally, the solar cells should generate enough power to power the active antenna and the power provided should be stable in order to avoid variations in the oscillation frequency and also to generate a stable low phase noise signal. The capacitor ( $C_{d1}$ ) is mounted as shown in Figure 4.13 to isolate the oscillator circuit from the DC feed and additionally the use of a voltage regulator at the output of the solar cell is considered in order to get a stable power from the solar cells and consequently obtain a more stable oscillation frequency from the active antenna.

An amorphous silicon a-Si solar module (SP3-37) with open circuit voltage 4.1 V and short circuit current 28 mA under  $100 \text{ mW/cm}^2$  (1 sun: a unit of power flux from the sun) solar irradiation was used as a DC power supply. The SP3-37 module internally consists of five a-Si solar cells with approximately 0.85 V open circuit voltage and 28 mA short circuit current in a series connection. In this work, one module was cut in two pieces across its long side and the two parts were properly placed on top of the active antenna ground plane and connected electrically in parallel as shown in Figure 4.16(a). Each solar cell piece has approximately 4.1 V open circuit voltage and 14 mA short circuit current. An equivalent circuit model of the solar cell consisting of an ideal current source, an ideal diode with saturation current  $I_s$ , a parallel resistance  $R_p$  and a series resistance  $R_s$  was created in [47] by measuring the DC I-V curve of the cell. The equivalent circuit model of the combined solar module is shown in Figure 4.9, where the parameters of the solar cell model are  $I_o = 1 \text{ nA}$ ,  $R_p = 110 \text{ } \Omega$ , and  $R_s = 7 \text{ } \Omega$ .

The active beacon antenna was first characterized in an indoor environment by using a halogen lamp to excite the solar module as shown in Figure 4.16(b). A luxometer was

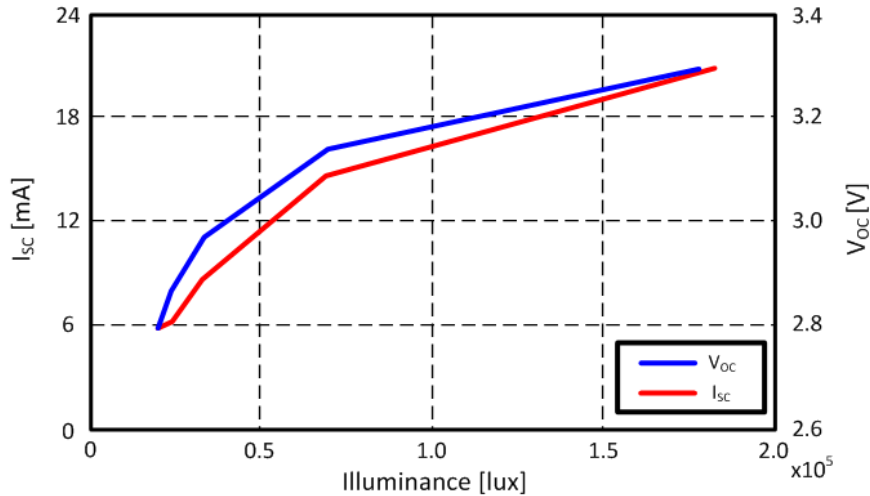


**Figure 4.17** Solar cell  $I_{sc}$  and  $V_{oc}$  versus illuminance

used to measure the illuminance at the active antenna position, while the distance of the halogen lamp was varied. Illuminance is typically used to characterize luminous sources at indoor environments. It is a photometric measure, which corresponds to the irradiance weighted by a luminosity function corresponding to the sensitivity of the human eye to light. Solar irradiance of  $100 \text{ mW/cm}^2$  (1 sun) corresponds to  $100 \text{ klux}$  illuminance. The measured illuminance at the solar cell location is about  $1.8 \times 10^5 \text{ lux}$ ,  $6 \times 10^4 \text{ lux}$ , and  $2 \times 10^4 \text{ lux}$  when its distance from the halogen lamp is 127 mm, 300 mm, and 500 mm respectively. The short circuit current ( $I_{sc}$ ) and the open circuit voltage ( $V_{oc}$ ) of the solar cell depending on illuminance are shown in Figure 4.17. It shows that the oscillation frequency can be stabilized by introducing a voltage regulator circuit since it supplies stable DC power to the oscillator. The stable oscillation frequency results in ease of matching between the antenna and the oscillator output, which are also due to the broadband property of the antenna. Figure 4.14, 4.17, and 4.18 show that the oscillation frequency can be stabilized when the illuminance is higher than  $3.3 \times 10^5 \text{ lux}$  since the solar cell is able to produce enough power to operate the circuit. The solar cell generates



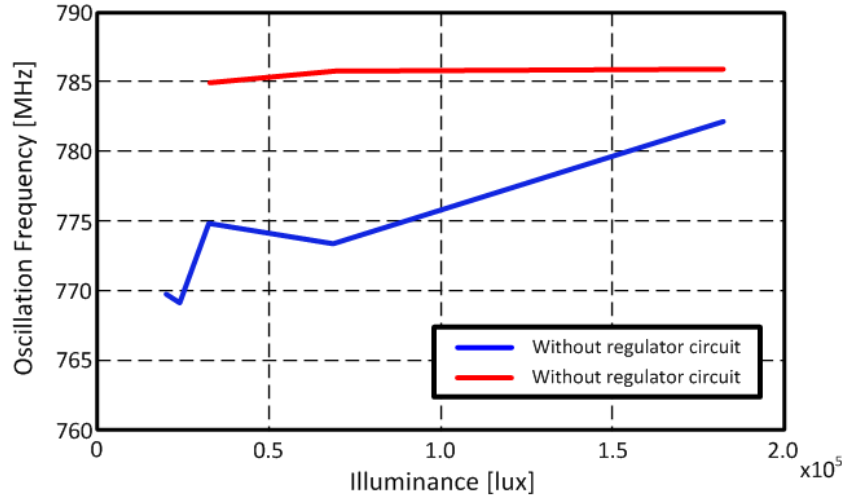


**Figure 4.18** Oscillation frequency versus illuminance with/without voltage regulator circuit.

16.2 mW ~ 28.6 mW depending on illuminance but the active antenna requires 6 mW ~ 28 mW which is affordable power from the solar cell providing the illuminance is higher than  $3.26 \times 10^4$  lux. The variation of the oscillator frequency with the illuminance is shown in Figure 4.18. For illuminance values less than  $2 \times 10^4$  lux, it was not possible to power up the oscillator. The frequency of oscillation is reduced compared to Figure 4.14(a), due to the loading effect of the solar modules.

The observed frequency variation is also due to the measurement setup as the lamp structure includes a metallic reflector (Figure 4.16(b)) that is affecting the antenna impedance and subsequently the oscillator frequency. A commercial regulator LT1763-1.8 with 1.8 V output voltage by Linear Technology was additionally used to minimize the DC supply variation due to the illuminance variation. The dissipated power of the regulator is in the range of 4.05 ~ 6.05 mW including quiescent power when it is powered by the solar cell providing the illuminance is stronger than  $3.26 \times 10^4$  lux. Measurements are included in Figure 4.18, demonstrating a significantly reduced frequency dependence on the illuminance. It was not possible to properly power the regulator for illuminance

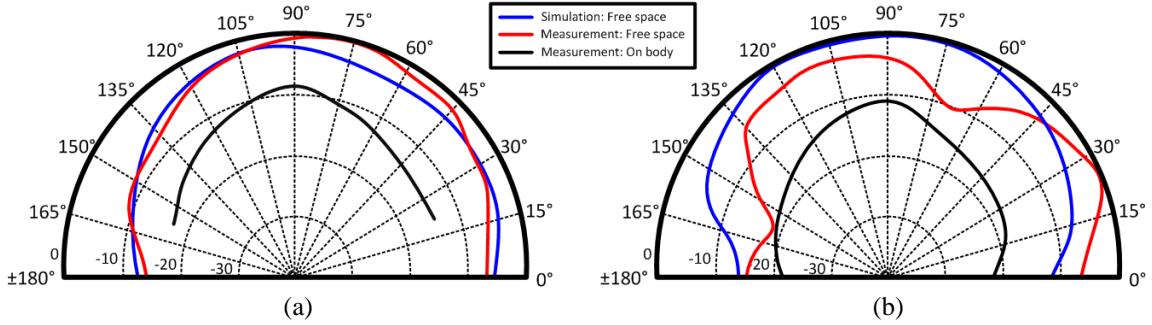


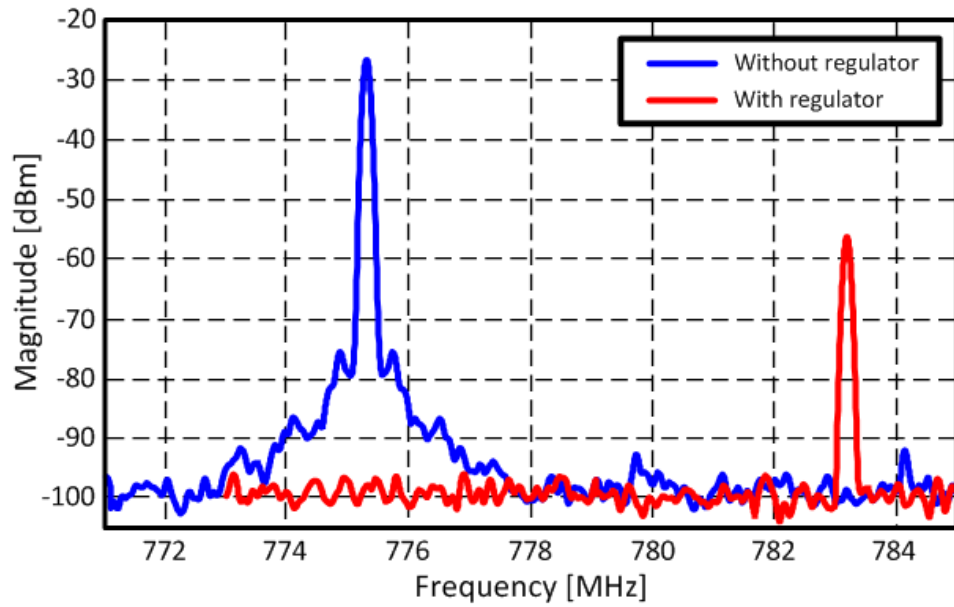
**Figure 4.19** Radiation patterns of active antenna under sun light: (a) E-plane (b) H-plane values less than  $3.26 \times 10^4$  lux. Finally, a slight increase of the oscillating frequency was observed when using the regulator. This is also attributed to the loading effect of the regulator on the active circuit.

Radiation patterns of the solar powered active antenna were obtained outdoors for a measured illuminance of  $1.6 \times 10^5$  lux. The radiated power from the solar-powered active antenna with the regulator circuit is measured, and the measured power patterns are shown in Figure 4.19. In order to test the effect of the flexing of the paper substrate on the radiation performance of the autonomous beacon, H-plane on-body measurements were also performed by placing the antenna on top of a cotton shirt and at the chest of a person showing an approximately 10 dB reduction in antenna gain (Figure 4.19). Similar omnidirectional radiation patterns in free space in Figure 4.19 suggest noteworthy results that the solar-powered active antenna has similar radiation patterns to that of the passive antenna. In addition, it loses omnidirectionality when the active antenna is mounted in the human body due to power absorption of the human body since a human body is a high dielectric material with a poor conductivity value (high loss tangent).

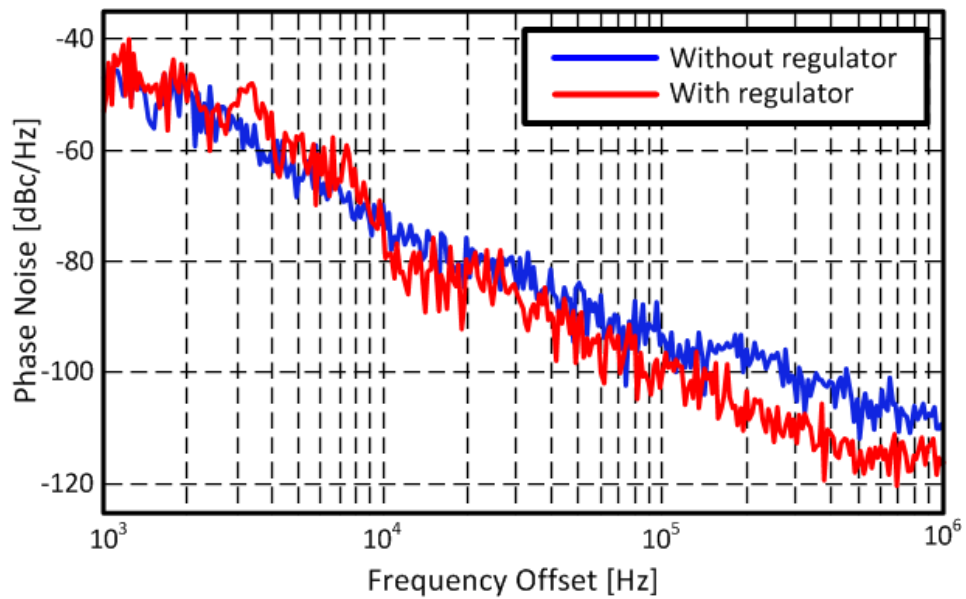
Finally, the power spectrum and the phase noise of the solar powered active antenna was measured. The blue line in Figure 4.20(a) shows the power spectrum of the antenna powered by the solar cell without the voltage regulator circuit, while the solid line shows

the spectrum of the solar-powered active antenna with the regulator circuit in the outdoor environment. It should be noted that solar illuminance with the voltage regulator leads to a cleaner spectrum than the one obtained without the regulator circuit. It is because the output voltage of the solar cell is fluctuating depending on the illuminance of the sun. The magnitude difference of the spectra is due to measurement error. The commercial broadband antenna previously shown in Figure 4.16(b) can't be used to get the power spectrum in the outdoor environment because it captures unwanted noises such as TV or other wireless signals, too. An open coaxial cable was placed near the antenna to catch a signal from the antenna, which resulted in the magnitude difference of the spectra. The observed frequency shifting of the antenna when it's connected to the regulator is due to the loading effect of the regulator circuit which includes capacitors and the regulator chip.

The blue line in Figure 4.20(b) shows the phase noise of the antenna for an illuminance of  $1.6 \times 10^5$  lux without the regulator, while the red line in Figure 4.20(b) shows the same measurement by including the regulator circuit. A phase noise value of -116.6 dBc/Hz at 1MHz offset was measured for the circuit that includes the voltage regulator showing an improvement in the phase noise of around 5 dB due to the better frequency stability when using the voltage regulator. The phase noise of the antenna with the regulator is slightly higher than that of the antenna without the regulator at the frequency offset band of 3 kHz ~ 4 kHz. It can be considered as an measurement error. This error can be caused due to fluctuation of intensity of sunlight and interference of unwanted signal since the measurement took place in outdoor environment.



(a)



(b)

**Figure 4.20** Measured (a) power spectra and (b) phase noise of active antenna under sunlight conditions with/without voltage regulator circuit.

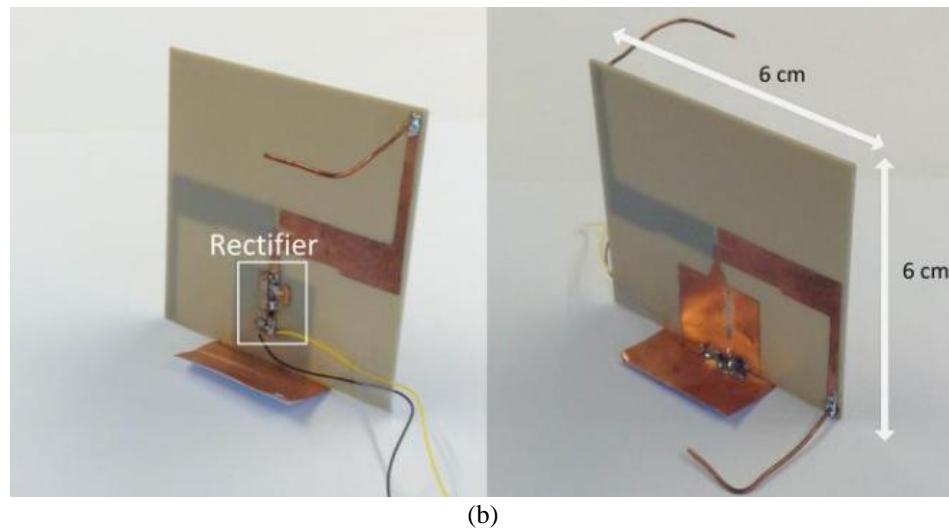
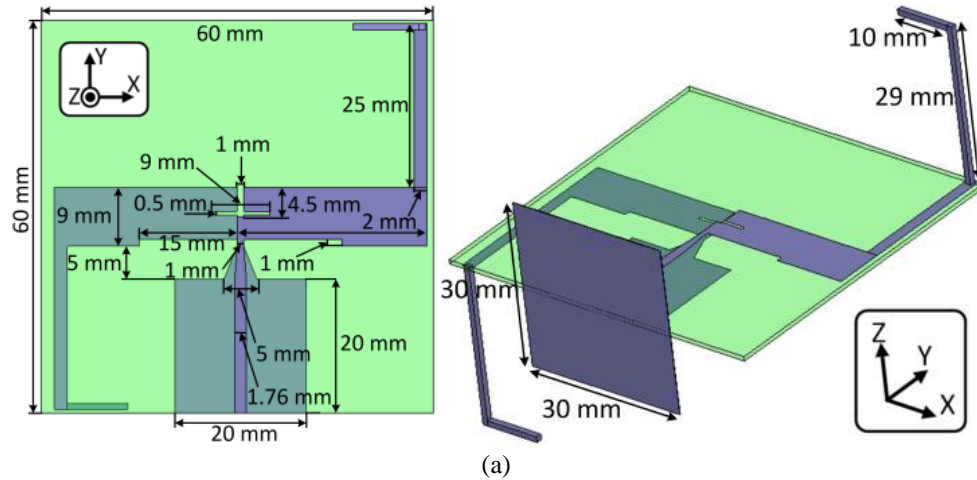


**Figure 4.21** Dual-band folded dipole antenna: (a) antenna geometry and (b) fabricated antenna

## 4.4 Dual-band Energy Harvester

### 4.4.1 Dual-band Dipole Antenna Design

A dual-band antenna for the dual band ambient energy harvester is designed using a full wave finite element method (FEM) software tool (Ansys HFSS) aside from a rectifier. A slot-loaded dual band folded dipole antenna was designed and it was fabricated on Arlon 25N which has relative permittivity ( $\epsilon_r$ ) of 3.38 and loss tangent ( $\tan \delta$ ) of 0.0025. A simple half-wavelength ( $\lambda_0/2$ ) dipole antenna at 915 MHz is folded to

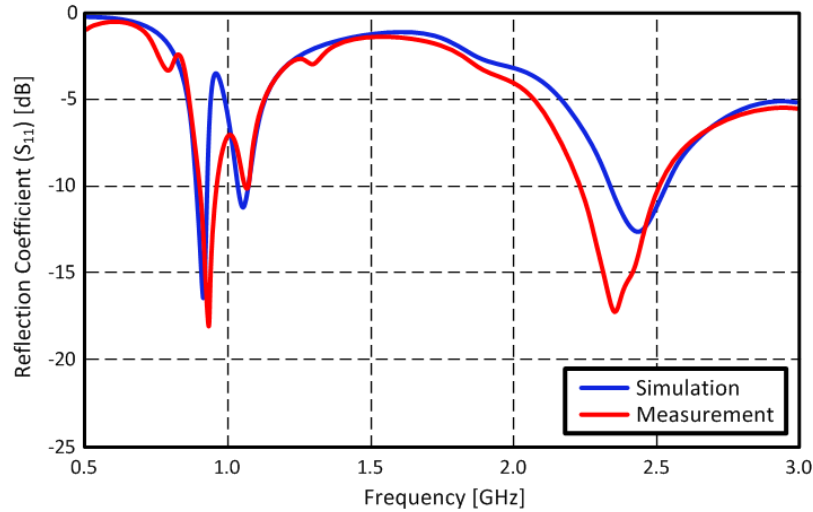


**Figure 4.22** Simulated and measured reflection coefficient ( $S_{11}$ ) of the dual-band antenna miniaturize the antenna and a slot is loaded in the middle of the antenna to introduce the second resonant frequency at 2.45 GHz. The geometry of the designed antenna and the fabricated prototype are shown in Figure 4.21.

The simulated and measured reflection coefficients ( $S_{11}$ ) of the linearly polarized antenna are presented in Figure 4.22 and the antenna covers the desired operation frequencies of 915 MHz and 2.45 GHz. The final size of the designed antenna is  $6 \times 6 \times 6$  cm<sup>3</sup> in a substrate thickness of 0.76 mm. The measured antenna gains are 1.87 dBi and 4.18 dBi at 915 MHz and 2.45 GHz, respectively. The measured and simulated radiation patterns for the XZ and YZ plane at 2.45 GHz and 915 MHz are shown in Figure 4.23 and Figure 4.24.

#### 4.4.2 Dual-band Rectenna Design

A single stage rectifying circuit has been chosen in order to get as high conversion efficiency as possible because the input power level at each frequency is low [48][49]. The whole system is shown in Figure 4.25. Agilent ADS harmonic balance (HB) simulation was used to maximize the RF to DC conversion efficiency at 915 MHz and

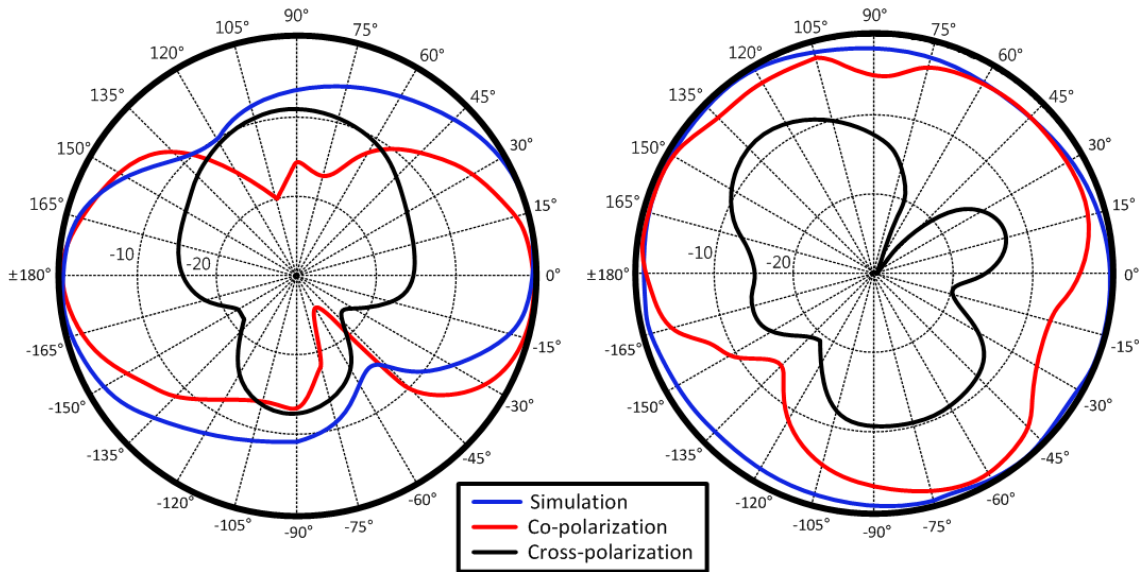


**Figure 4.23** Simulated and measured radiation patterns at 2.45 GHz: (a) XZ plane and (b) YZ plane.

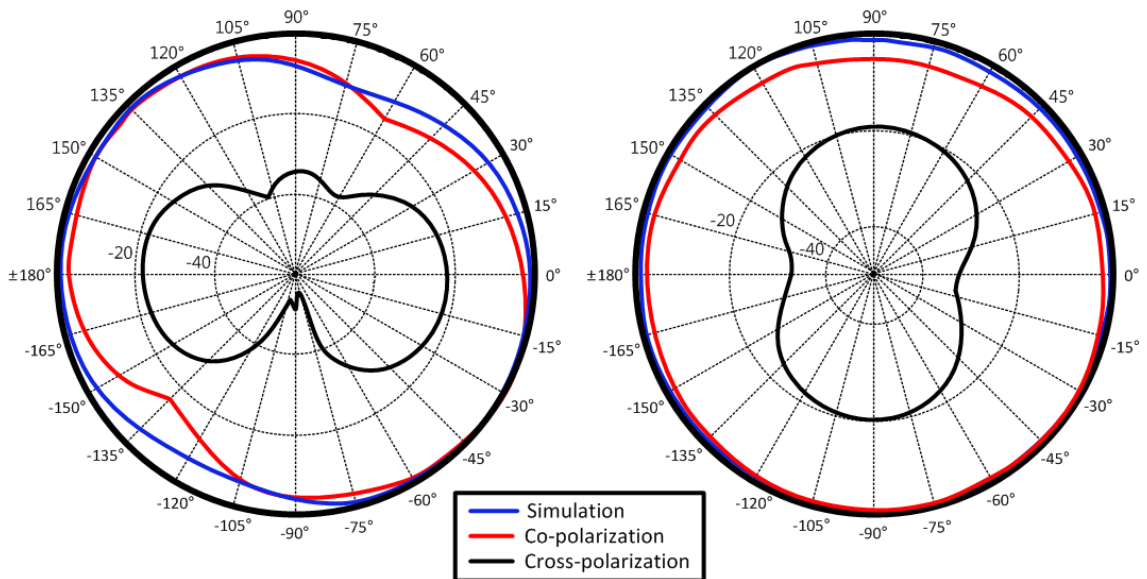


**Figure 4.24** Simulated and measured radiation patterns at 915 MHz: (a) XZ plane and (b) YZ plane

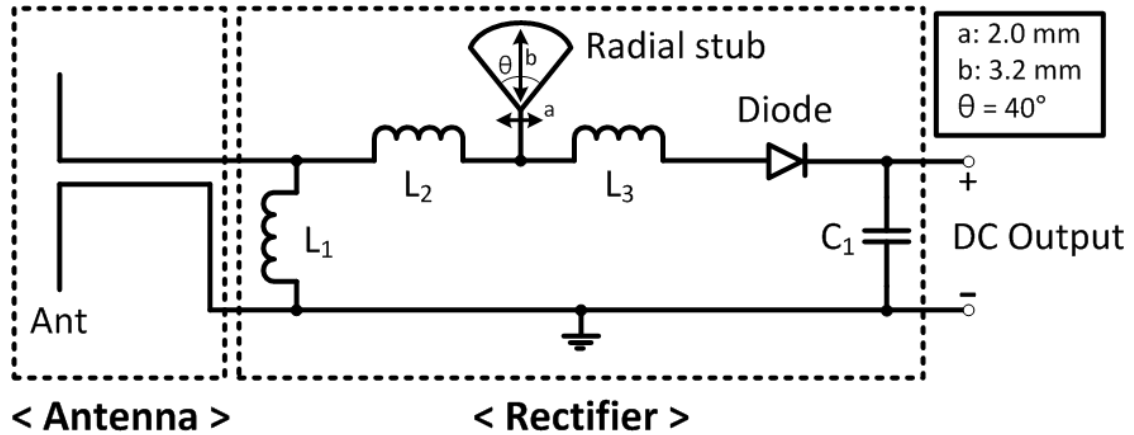


**Figure 4.25** Schematic of the proposed dual band rectifier. Component values are  $L_1 = 7.5$  nH,  $L_2 = 10$  nH,  $L_3 = 8.7$  nH,  $C_1 = 100$  pF and  $R_{load} = 2.2$  k $\Omega$ .

2.45 GHz. The goals are used to define the minimum RF-DC efficiency at 915 MHz and 2.45 GHz for a selected input power level and for an output load of 2.2 k $\Omega$  [49]. The optimum matching network consists of three inductances ( $L_1 = 7.5$  nH,  $L_2 = 10$  nH and  $L_3 = 8.7$  nH) and a radial stub. The input impedance of the rectifier is matched to a 50  $\Omega$  representing the dipole antenna. The Skyworks SMS7630 Schottky diode is used for the design of the rectifier circuit. A prototype is built, and its performance is evaluated using single tone as well as dual tone signal measurements. The total size of the rectifier is about  $1.9 \times 2.1$  cm<sup>2</sup>. Simulated and measured reflection coefficients ( $S_{11}$ ) of the rectifier are shown in Figure 4.26.

The RF-DC conversion efficiencies at operating frequencies (915 MHz and 2.45 GHz) with different input power levels (-15 dBm, -9 dBm, and -3 dBm) were measured. The system has a 25 %, 37 %, and 45 % conversion efficiency at 915 MHz while 20 %, 30 % and 37 % efficiency at 2.45 GHz with input power levels of -15 dBm, -9 dBm, and -3 dBm, respectively. The performance of the rectifier for a single tone signal and a two-tone signal at the frequencies of interest is also tested. The two single tone signals are



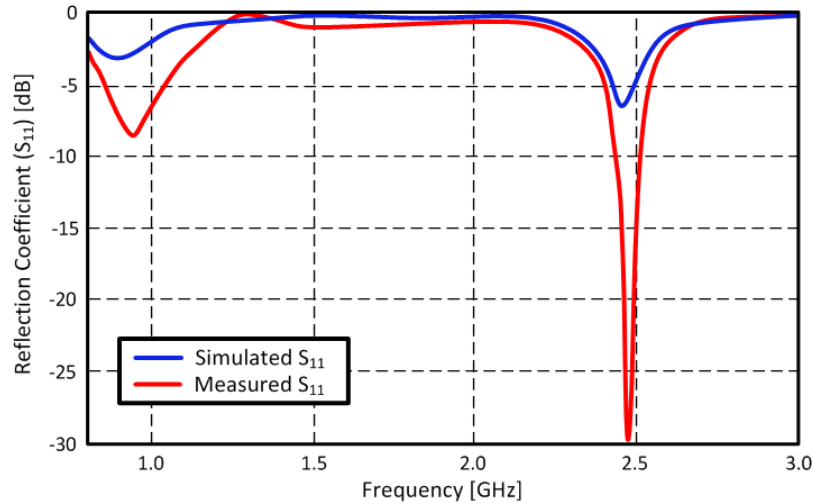


**Figure 4.26** Simulated and measured input reflection coefficient ( $S_{11}$ ) of the dual band rectifier.

combined to generate a two tone signal. This resulted in an RF-DC conversion efficiency of 48 % and 39 % for an input power level of 0 dBm at 915 MHz and 2.45 GHz, respectively, while it has 48 % of conversion efficiency for two-tone signal. Additionally, it can be seen that the rectifier RF-DC conversion efficiency is less than 1 % for an input power level lower than -33 dBm, as for low input power levels the Schottky diode is not operating in its optimum zone for maximum RF-DC conversion.

The rectenna is also evaluated for an incident power density of  $1 \text{ uW/cm}^2$ . Considering the measured antenna gain at 915 MHz and 2.45 GHz, the antenna effective area is calculated as  $132 \text{ cm}^2$  and  $31 \text{ cm}^2$ , respectively. For a power density of  $1 \text{ uW/cm}^2$ , the input power is -9 dBm and -15 dBm at 915 MHz and at 2.45 GHz, resulting in an RF-DC conversion efficiencies of 37 % and 20 %, respectively.

## 4.5 Summary

Printed microwave components for autonomous wireless sensor platforms, such as an antenna on an AMC for wearable applications, a beacon oscillator for wireless power

transfer (WPT) and identification, and a dual-band rectenna for RF energy harvesting, are presented in this chapter. The AMC plane was inkjet-printed on flexible organic paper and a monopole antenna was mounted on the AMC plane to test the AMC. The antenna parameters like gain and radiation patterns were significantly modified when it was placed on a human body phantom. The AMC plane successfully isolated the RF system from the human phantom which is a lossy high dielectric material. The communication range of a wireless sensor on the human body is increased by a factor of 3 compared to other antennas without the AMC plane. This suggests that only 1/9 of the power is required to maintain the same communication range resulting in low-power wireless sensor networks.

Design considerations and steps for a beacon oscillator for wireless power transfer (WPT) and identification are discussed. The beacon oscillator consists of a reflection type oscillator, solar module, folded slot antenna, and DC regulator. Each component is discussed in detail and its performance is experimentally verified. The proposed beacon oscillator can be utilized as a power broadcaster to transfer power to turn-on autonomous sensor nodes.

Lastly, a dual-band rectenna design is presented. A dual-band antenna and rectifier are integrated together and its performance is measured. The measured conversion efficiency of the rectifier was 37 % at 915 MHz and 20 % at 2.45 GHz in a  $1\mu\text{W}$  power density environment. The multi-band RF energy harvesting technology is a critical feature to implement the autonomous wireless sensor platform.

## CHAPTER 5

### PRINTED RFID-ENABLED SENSORS

#### 5.1 Introduction

Over the last decade RFID-enabled sensing systems have received an increasing level of attention mostly due to their relative simple system architecture, that typically consist of simple sensing tags and interrogation readers facilitating their integration with other existing Wireless Sensor Networks (WSN) and RFID infrastructure [50][51]. In addition, a passive RFID sensing system's life time is longer and its cost is much lower compared to active sensing systems, while RFIDs can constitute low-power wireless platforms [52] with broad sensing capabilities including temperature, gas, strain and humidity sensing [53]-[57]. It is possible to utilize on-demand sensor systems as a smart skin for strain, ambient conditions and biomonitoring sensing applications or a bio-monitoring sensor as well as a Machine-to-Machine (M2M) communication node when it is integrated to the WSNs. Plus, the RFID-enabled sensor systems could potentially be one of the most enabling factors to implement realistic large-scale topologies of Internet of things (IoT) in the future [58].

Nevertheless, there are still numerous challenges on implementing the proposed RFID-enabled sensor with the dual tag sensing topology. First of all, the crosstalk between the multiple tags utilized in the sensor should be considered. A higher amount of power is required to activate the dual-tag sensor compared to typically used single-tag sensor topologies since multiple RFID IC's should be activated by the reader, otherwise the same amount of interrogation power result in shorter reading ranges. It is important to

find an optimal distance between the two dipole antennas in order to minimize the size of the sensor as well as the crosstalk level, thus preventing unwanted power losses. The cost of the RFID-enabled sensor is also a critical factor for large-scale practical implementations.

In this chapter, an inkjet-printed RFID-enabled dual-tag sensor and chipless sensor are presented. Preliminary results of a prototype sensor tag and a proof-of-concept demonstration of the sensors are discussed.

## **5.2 RFID and RFID-enabled Sensors**

RFID systems have a lot of attractive advantages and great potential for wireless sensor applications as shown in Figure 5.1. First of all, the cost of an RFID tag is very low. The cost of an RFID tag can be further reduced by introducing cost efficient fabrication technologies such as inkjet printing technology on low cost substrate such as paper or plastics. Implementing a low cost RFID-enabled sensor tag is important because wireless sensor networks systems utilize a large amount of sensor nodes rather than the number of readers or receivers. The RFID system has a simple architecture which consists of tags and readers whereas the conventional wireless sensor networks consists of sensor/relay node, lots of electronic components and mixed-signal interfaces. In addition, RFID systems are compatible with a conventional WSN. The life time of a passive RFID is relatively longer than other active sensor devices. Moreover, recently reported research works show the broad sensing capability of RFID-enabled sensors. RFID-enabled temperature, gas, strain, water quality and humidity sensors have been demonstrated.

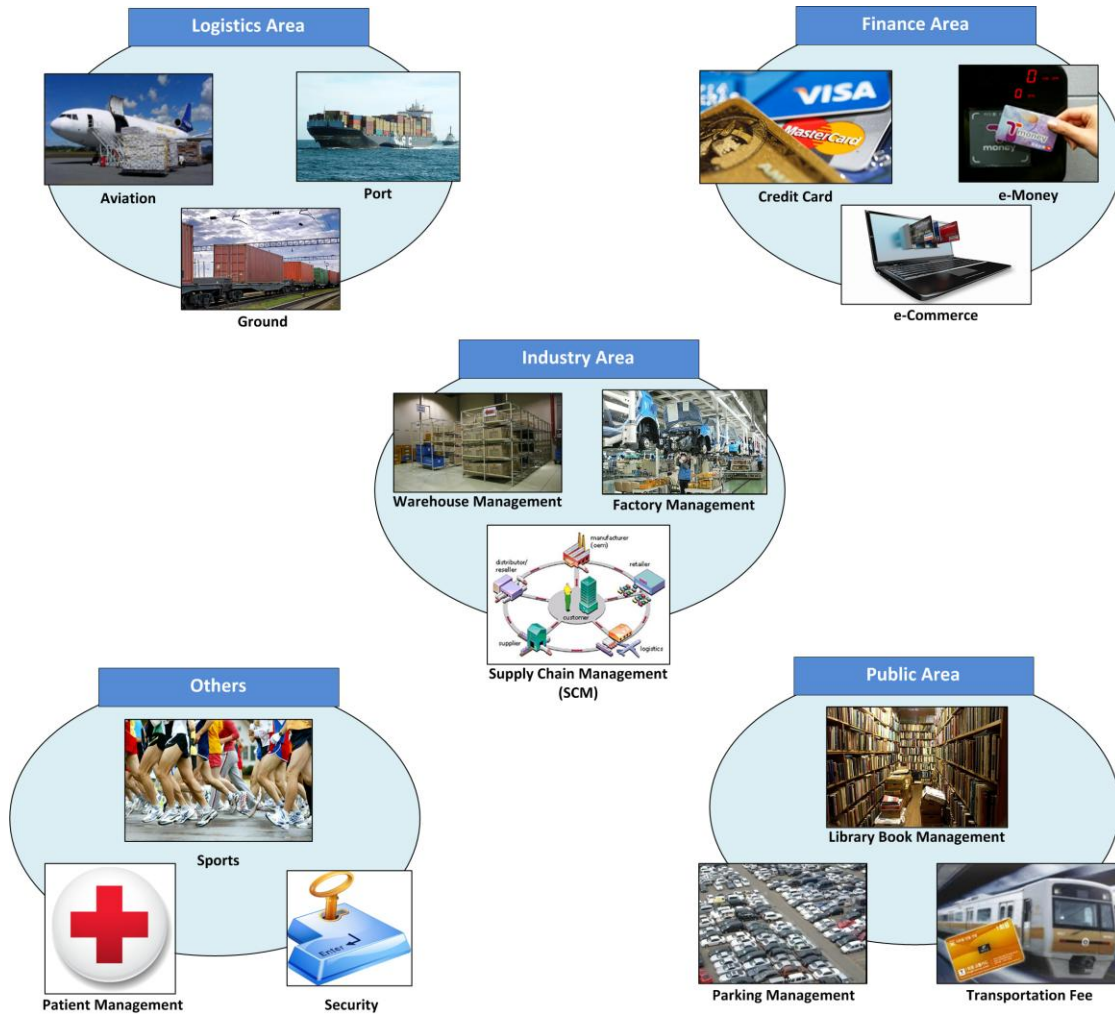


**Figure 5.1** RFID application areas

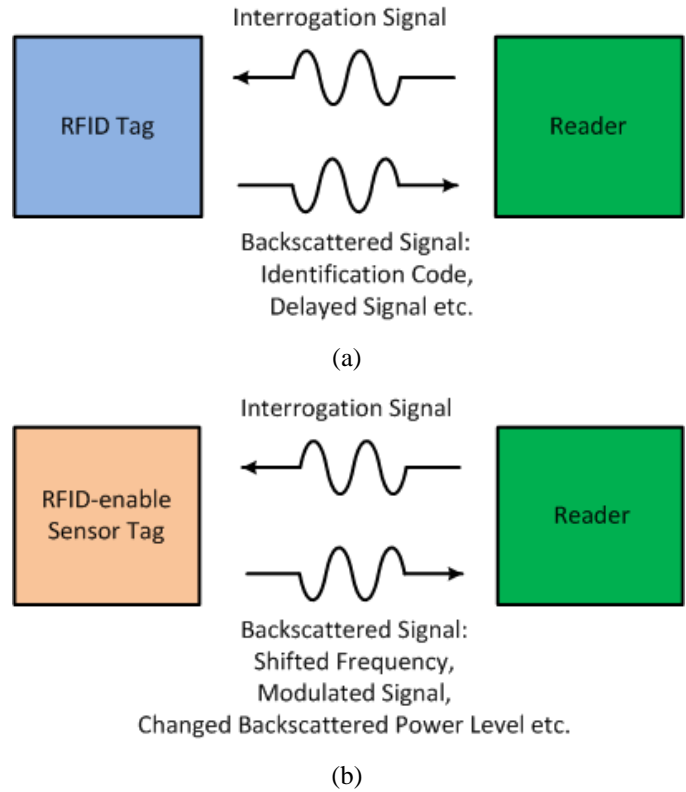


**Figure 5.2.** (a) RFID tag and (b) RFID-enabled sensor tag

Most of RFID-enabled sensors are integrated with selected sensing materials depending on the sensing target such as water absorbing materials for humidity sensors or carbon nano-structures for gas sensors. The chemical, physical, or electrical reaction of the sensing materials under changes in the sensing target produce changes in the impedance of the sensing materials which results in a shift of the resonant frequency of the RFID tag antenna as shown in Figure 5.2. This approach is one of the simplest low cost, power efficient architecture to implement the RFID-enabled sensors.

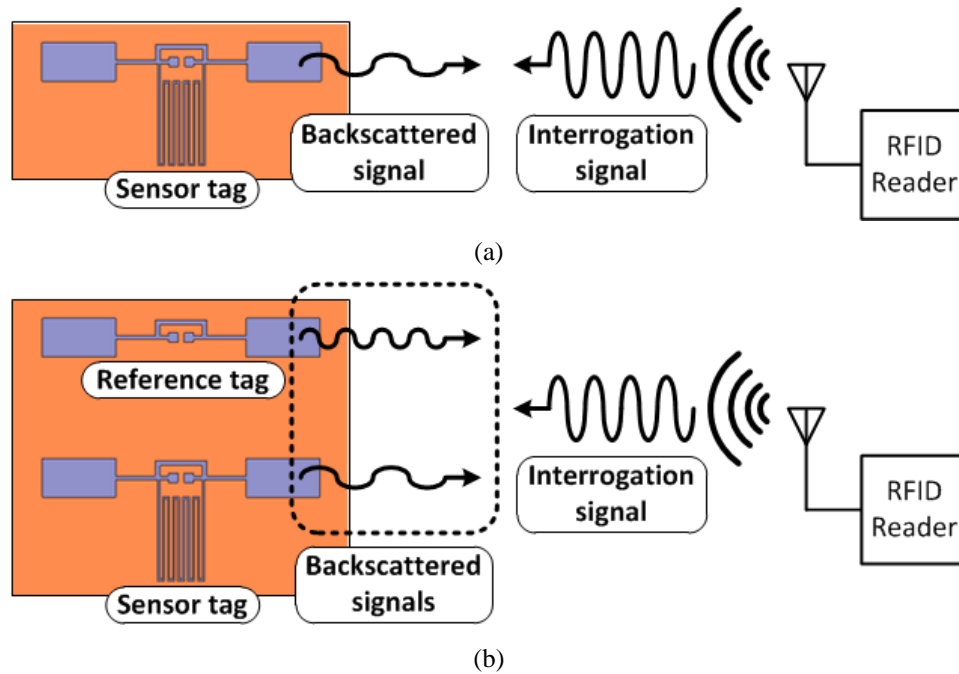


**Figure 5.3** RFID-enabled sensor topologies: (a) single-tag and (b) dual-tag sensing topology

## 5.3 Inkjet-printed Dual-tag RFID-enabled Haptic Sensor

### 5.3.1 Dual-tag Sensing Topology

There are two types of passive RFID-enabled sensing topologies: single-tag sensing and dual-tag sensing. The basic concept of those RFID-enabled sensing topologies is introduced in Figure 5.3. The single-tag topology utilizes one RFID tag integrated with an inductive or a capacitive sensing component [59]. The backscattered signal from such a sensor tag experiences changes, such as frequency shift or modulation, in the event of the detection of different quantities of a sensed parameter, that affect the impedance of the RFID sensor-antenna combination, as shown in Figure 5.3(a). This type of RFID-enabled sensor topology is relatively easy to implement due to the simplicity of the sensor system. However, the resonance frequency of the RFID antenna or a sensing component can also be affected by its surrounding environment. It results in an unwanted shift of the resonant frequency of the sensor tag or a false alarm when the RFID antenna

is utilized as a sensor. In this case, it is hard to determine if the sensing event detection from the sensor tag is true or false and a typically cumbersome calibration process has to be implemented.

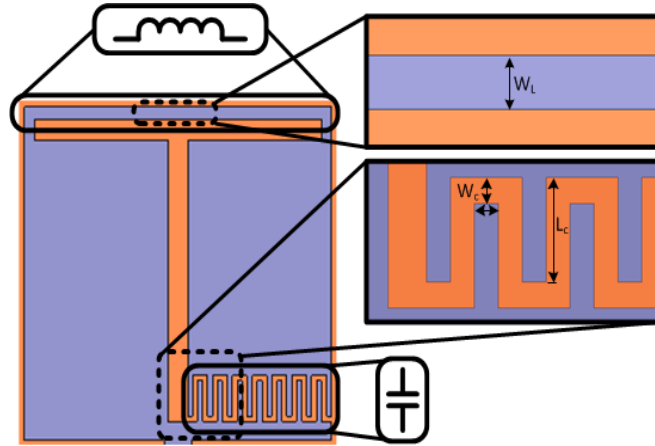
Unlike the single RFID tag sensing system, the dual-tag sensing topology utilizes two RFID tags (a sensor tag and a reference tag) for a calibration-free detection and decision process as shown in Figure 5.3(b) [60]. A reader can distinguish two tags because each RFID chip of the tag returns their identification code when a tag is excited. The sensing tag of the dual-tag sensing topology is similar to the sensing tag of the single tag sensing topology while the reference tag is an identical RFID tag excluding the sensing component. The individual backscattered/response signals from the two tags of the dual sensor tag configuration are almost identical when no sensing event is detected, due to the fact that the effect of the surrounding environment is approximately the same on the two closely spaced tag antennas, thus eliminating the need for calibration and filtering. Nevertheless, the response of the two tags becomes different when a sensing event is triggered (e.g. in the presence of a sensed substance), and a decision process can be defined by comparing the backscattered signals from the two tags. For example, the required minimum transmitted (Tx) power curves of the two RFID tags are almost the same if there is no presence of the detected substance because the RFID chip and the antenna are matched at the same frequency. However, the resonant frequency of the sensor tag experiences a change due to the presence of the detected substance which results in different required minimum Tx power curves for each antenna. Finally, it should be noted that the orientation of the antennas affects the readability minimally when a circularly polarized antenna is utilized for the interrogation. This type of sensing



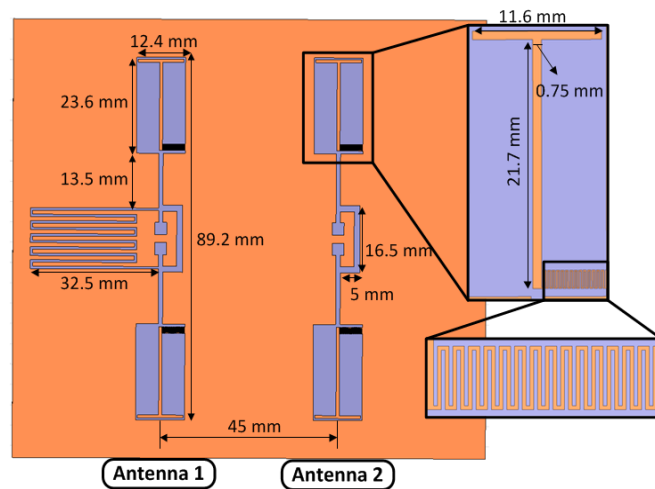
topology is operating in a robust way compared to the single-tag sensing system because the event decision is made utilizing the difference of the backscattered signals between the sensor tag and the reference tag or the backscattered signal from the reference tag as a calibration signal. Therefore, the effects of unwanted reflections from surrounding objects and of different mounting substrates can be easily calibrated out. However, introducing an additional reference tag increases the total size of the sensor and may also cause crosstalk issues between the individual tags. The crosstalk level typically increases as the distance between the sensor tag and reference tag decreases, which commonly results in short read range and poor readability due to increased minimum required power to activate the passive dual sensor tag. Therefore, when designing a dual-tag sensor, it is important to find the optimum distance between the two antennas (sensor tag and reference tag) in order to satisfy simultaneously the requirements of a minimal crosstalk level and of a miniaturized size.

### *5.3.2 Isolation Structure: Series LC Resonator*

An isolation structure consisting of a series LC resonator is utilized in order to both suppress the crosstalk level and reduce the spacing between the two RFID tags [61]. In this work, LC resonator structures that consists of a thin-strip inductor and an interdigitated capacitor [61] are introduced in the RFIDs' dipole antennas as shown in Figure 5.4. The inductance of the proposed isolator is a function of the width ( $W_L$ ) and the length of the inductor line. The unit inductance of a flat rectangular line has been reported in [62] showing that its width is the dominant design parameter when its metal thickness is much smaller than the width. The full 3D simulator, Ansys HFSS v11.1, is utilized for this analysis. The crosstalk level variation as a function of the width ( $W_L$ ) of



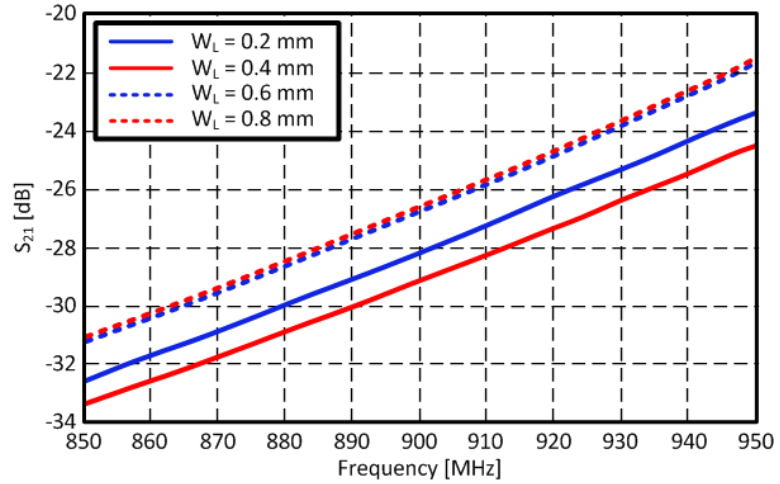
(a)



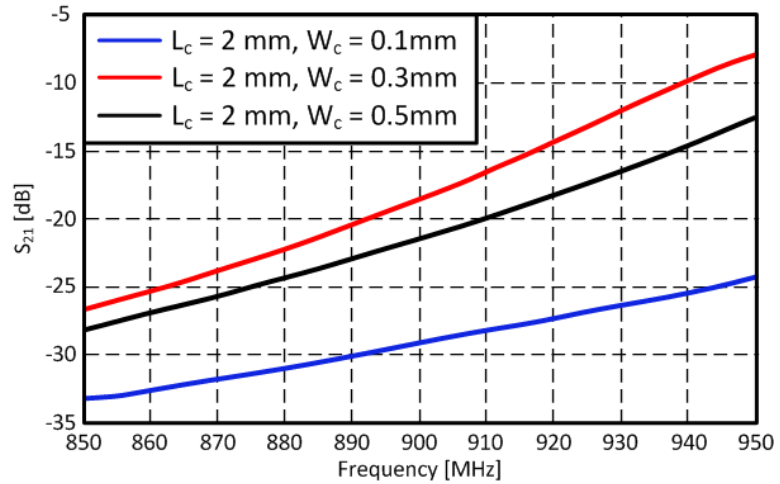
(b)

**Figure 5.4** (a) Structure of the LC resonator and (b) a geometry of the proposed RFID-enabled sensor.

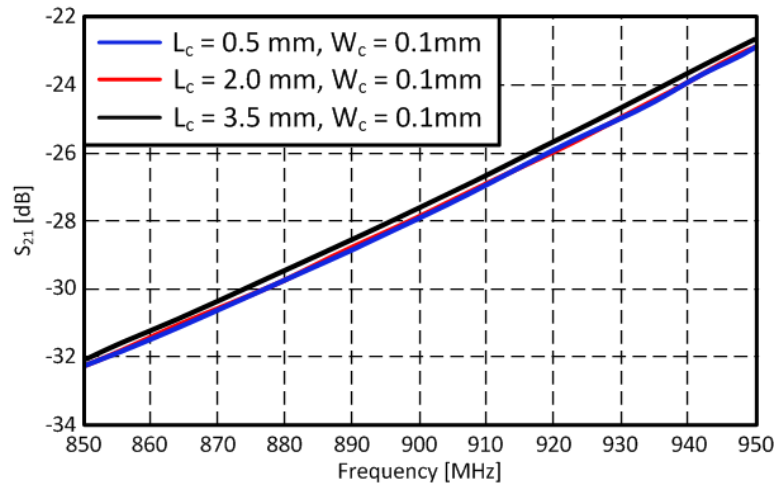
the inductor line while fixing the design parameters of the interdigitated capacitor ( $W_C = 0.1$  mm,  $L_C = 2.0$  mm) is shown in Figure 5.5(a). The crosstalk level between the antenna 1 and antenna 2 in Figure 5.4(b) is shown in terms of  $S_{21}$  for a fixed distance between the antennas of  $d = 45$  mm. Its variation versus the changes of the unit inductance of the isolator is relatively small compared to the variation of the crosstalk level versus the capacitance change as shown in Figure 5.5(a), (b). Based on the analysis shown in Figure 5.5, the most important design parameters are the width and the gap of the interdigitated capacitor ( $W_C$ ) compared to the length of the fingers ( $L_C$ ) as the fringing capacitance



(a)



(b)



(c)

**Figure 5.5** Parameter sweep of the LC resonator structure: (a) width ( $W_L$ ) of the inductor, (b) width ( $W_C$ ) and (c) length ( $L_C$ ) of the interdigitated capacitor.

plays a significant role in the value of the total capacitance [63]. Given the area of the patch termination of the RFIDs' dipole antennas, the dimensions of the LC resonator are chosen to minimize the crosstalk level ( $W_L = 0.4$  mm,  $W_C = 0.1$  mm,  $L_C = 2.0$  mm) which results in 29 fingers of the interdigitated capacitor. The LC resonators are placed asymmetrically along the dipole axis (X-axis) to induce out-of-phase near-field current to suppress mutual coupling [61]. The various features of the interdigitated capacitor and of the strip inductor are easily met by inkjet printing fabrication technology, which has a demonstrated resolution of 25  $\mu\text{m}$  [64]. Furthermore, the isolating structure results in eliminating ink from certain regions of the original antenna structure and consequently leads to further cost savings.

### *5.3.3 RFID-enabled Sensor Tag with LC Resonators*

The smallest distance value ( $d$ ) between the antennas is chosen in order to minimize the total size of the RFID-enabled sensor tag while satisfying the desired crosstalk level at the operation frequency range. In this paper, the crosstalk level of -25 dB throughout the bandwidth of operation (850-950 MHz) is chosen as a design example. The two RFID tags with the dipole embedded LC resonator are placed side-by-side. The distance ( $d$ ) of 45 mm ( $0.137\lambda_0$ ) is chosen and the crosstalk level without the isolation structure (series LC resonator) is shown in Figure 5.6 as a reference. The crosstalk level of the antennas with the isolator is about 4 ~ 5 dB lower than the antennas without the isolator at the operation frequency range. The length of the RFID antennas is also miniaturized due to the loaded LC resonator. The length of the proposed inkjet-printed antenna on paper substrate is 89.2 mm ( $0.27\lambda_0$ ) which is 28.4 % shorter than the length of the inkjet-printed

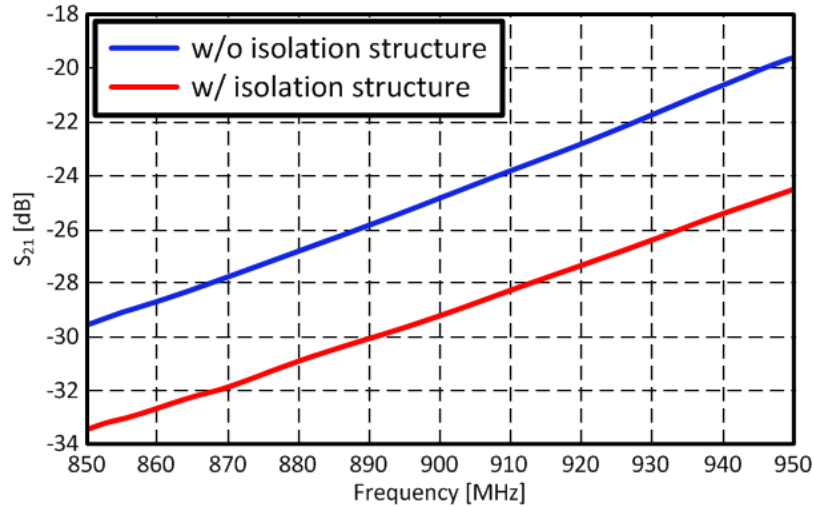


**Figure 5.6** Crosstalk level between the antenna 1 and the antenna 2 with/without the LC resonators.

dipole antenna on paper substrate without any miniaturization (125 mm, [65]) at the operation frequency of 915 MHz.

The final design step involves the integration of a sensing/event detecting meandered line with the antenna of the sensing tag, featuring a frequency response that is dependent on the presence of the sensing target. The size of the proposed RFID-enabled sensor including the meandered line is 84 mm × 95 mm. The antenna with the meandered line is the sensing configuration with a frequency response depending on the presence of the sensing target. The meandered line should not affect the antenna's resonant frequency while at the same time it should be sensitive enough to be able to sense the target event. The meandered line is designed to have the high impedance at the resonant frequency of the antenna by optimizing the width (inductance) and the pitch (capacitance) of the meandered line [66]. Thus, it is designed to feature a high impedance (open-circuit) in the absence of a sensing event and a gradually lower impedance value eventually affecting the resonant frequency of the sensing tag in the presence of a sensing target. The optimal

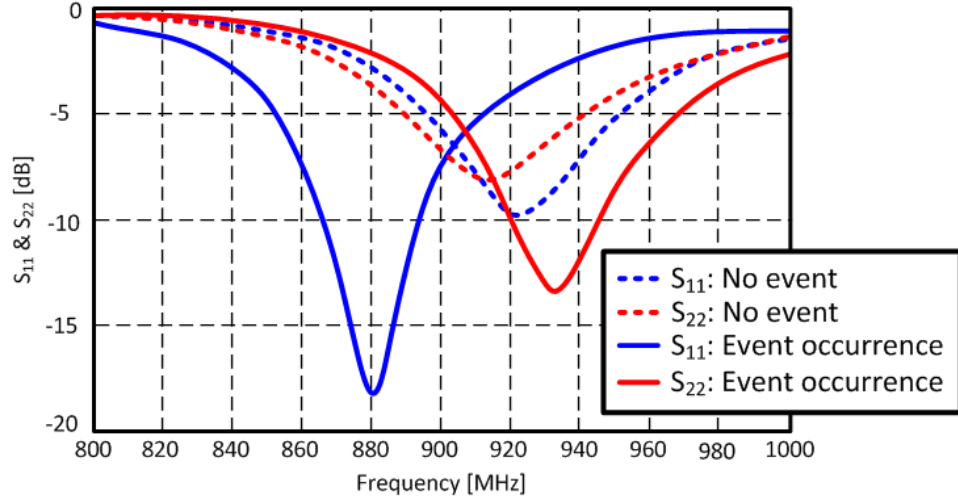


**Figure 5.7** Simulated scattering parameters ( $S_{11}$  &  $S_{22}$ ) of the sensor tag (antenna 1) and the reference tag (antenna 2)

value for the width of the meander line is 0.6 mm and the pitch of the line is 3.2 mm and the detailed dimensions of the proposed RFID-enabled sensor are shown in Figure 5.3(b).

The resonant frequency of the sensor tag (antenna 1 in Figure 5.3(b)) is strongly affected by the capacitance variation of the sensing meandered line (capacitive sensing) due to the loading effect when a high dielectric constant ( $\epsilon_r$ ) and loss tangent ( $\tan \delta$ ) material, such as a human finger (haptic sensing), approaches or touches the meandered line. The peak frequency of the reference tag's (antenna 2 in Figure 5.3(b))  $S_{11}$  curve is also shifted due to the change of the mutual impedance when the human finger acts as an additional load to the sensor tag resulting in a different matching point. Initially (lack of the finger presence) the two antennas have similar frequency responses ( $S_{11}$  (antenna 1) &  $S_{22}$  (antenna 2)) before the human finger touches the meandered line (no event). The resonant frequency of the sensor tag (antenna 1) is shifted to a lower frequency due to the loading (higher capacitance) effect of a touching finger (event occurrence) although the reference tag (antenna 2) keeps almost the same frequency response. In our benchmarking case, the resonant frequency of the sensor tag shifted by 43 MHz while the

that of the reference tag shifted by 9 MHz as shown in Figure 5.7. The human finger has been modeled as a rectangular box which has the dielectric constant ( $\epsilon_r$ ) of 21.14 and the conductivity of 0.36 S/m. The values of the dielectric constant and the conductivity were chosen to the mean values of those of the human skin, the flesh, and the bone [67]. The RFID chip (NXP's SL3ICS1002/1202) is modeled as a parallel resistor-capacitor (R-C) network to model the frequency dependence of the input impedance of the chip. The modeled resistor value (R) is 1.13 k $\Omega$  and the capacitance value (C) is 1.41 pF, which results in the input impedance of  $13.3 - j122 \Omega$  at 915 MHz. At 915 MHz, the magnitudes of the reflection coefficients ( $S_{11}$  &  $S_{22}$ ) have very similar values, but they become different after the event occurrence, which results in two different required transmitted (Tx) power curves to excite each tag over the simulated frequency range. The two different required Tx power curves to excite the tags are utilized to make an event decision.

#### *5.3.4 Read Range Estimation*

Figure 5.8 shows the inkjet-printed RFID-enabled sensor on paper and Figure 5.9 shows the simulated radiation patterns of the designed RFID-enabled single and dual tag sensors along the E- (XZ) and H- (YZ) planes. The patterns are normalized by that of the reference tag. In the case of the dual tag sensor, the radiation patterns of each tag antenna are plotted by exciting one antenna while leaving the other open circuited. Furthermore, Figure 5.9 includes the radiation patterns of the dual tag sensor when a human finger touches the sensor tag. It can be observed that both the single and dual tag sensors have very similar radiation patterns with an omni-directional shape. The individual gain values of the antennas of the dual-tag sensor are 3.3 dBi (sensing tag antenna) and 3.71 dBi

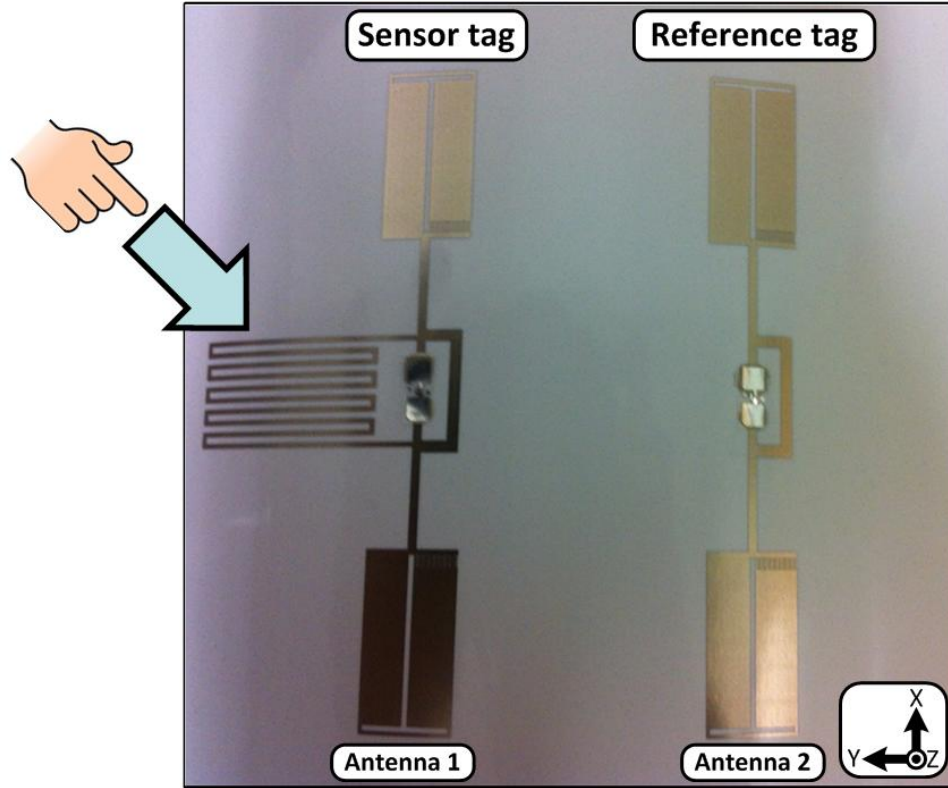


**Figure 5.8** Inkjet-printed RFID-enabled sensor on paper substrate.

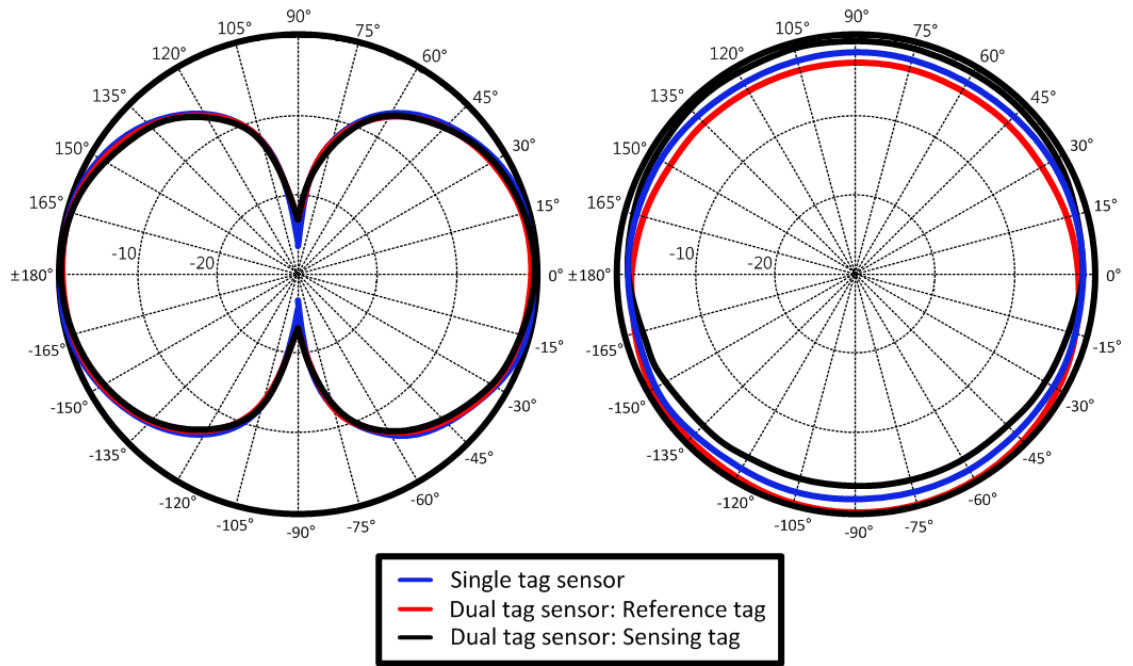
(reference tag antenna) at 915 MHz, which become 0.0 dBi (sensing tag antenna) and 3.47 dBi (reference tag antenna) when a human finger touches the sensor. In comparison the single tag sensor demonstrated a gain of 1.94 dBi at 915 MHz for the single tag sensor, which became -1.21 dBi when a human finger touches the sensor.

The read range of a single antenna tag can be estimated using (5.1) based on the antenna gain values, the input impedance of the antenna, and the impedance of the RFID chip, using the Friis free-space transmission formula as shown in [68].

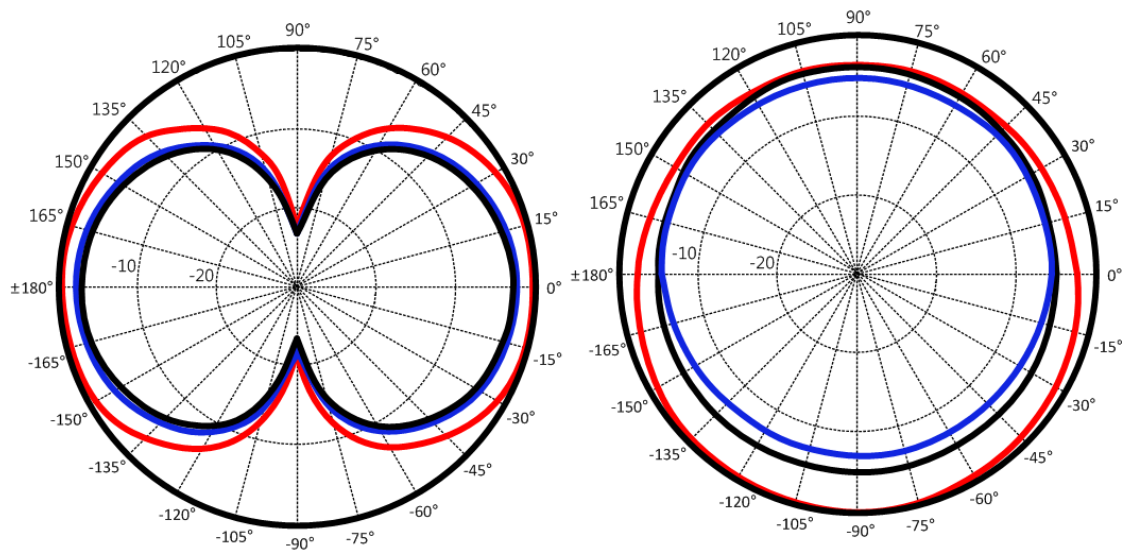
$$R = \frac{\lambda_0}{4\pi} \sqrt{\frac{P_t G_t G_r \tau}{P_{th}}} \quad (5.1)$$

$$\tau = \frac{4R_a R_c}{|Z_c + Z_a|^2} \quad (5.2)$$





(a)



(b)

**Figure 5.9** Simulated radiation patterns of the RFID-enabled single-tag and double-tag sensors (a) without touch and (b) with touch.

where  $\lambda_0$  is the wavelength in the free-space,  $P_t$  is the transmitted power by the reader,  $G_t$  is the gain of the transmitting antenna of the reader,  $G_r$  is the gain of the receiving RFID tag antenna,  $P_{th}$  is the minimum required power to excite the RFID chip, and  $\tau$  is the power transmission coefficient [68].  $Z_c = R_c + jX_c$  and  $Z_A = R_A + jX_A$  are the complex impedances of the RFID chip and the antenna, respectively. The read range  $R$  of an RFID tag is proportional to the square root value of the transmitted power  $P_t$  as shown in (5.1), because the other parameters such as the wavelength, the gain of the Tx and Rx antennas, the threshold power level to excite a RFID chip  $P_{th}$ , and the power transmission coefficient  $\tau$  [69] are fixed once the antenna measurement system is established at each interrogation frequency. The range equation (5.1) can be normalized to a reference range factor,

$$R_0 = \frac{\lambda_0}{4\pi} \sqrt{\frac{P_t G_t}{P_{th}}} \quad (5.3)$$

$R_0$  is the estimated range of a tag which has a gain of 0 dBi and which is matched to the RFID chip at the operation frequency. The normalized range (1) can therefore be written as

$$\frac{R}{R_0} = \sqrt{G_r \tau} \quad (5.4)$$

In the case of a two port system such as the dual tag sensor or generally a multiport system, the formulation needs to be modified to reflect the fact that the received power at each antenna is affected by the mutual coupling among the different antennas. The theory

of loaded multiport scatterers has been presented in [70]. The theory of [70] combined with reciprocity theory [71] was used in [72] to optimize the RF-DC conversion efficiency of a two-port dual polarized rectenna. Furthermore, [72] applied [69] and presented a formulation deriving the estimated tag range in the case of multi-port (grid) RFID systems.

The received power  $P_{r,n}$  at port  $n$  is expressed as in [72]

$$P_{r,n} = \left( \frac{\lambda_0}{4\pi R_n} \right)^2 P_t G_t G_{r,n} \quad (5.5)$$

where  $G_{r,n}$  is an embedded realized gain at port  $n$ . Setting the received power equal to the threshold power  $P_{th}$  to activate the tag chip, and using the definition of the reference range factor  $R_0$ , equation (5.5) can be solved to derive the range of a chip placed at port  $n$

$$\frac{R_n}{R_0} = \sqrt{G_{r,n}} \quad (5.6)$$

which is similar to (5.4).

The embedded realized gain  $G_{r,n}$  is given by [73]

$$G_{r,n} = 4R_c |[\mathbf{Y}]_n \mathbf{g}|^2 \quad (5.7)$$

where  $\mathbf{Y} = (\mathbf{Z}_C + \mathbf{Z}_A)^{-1}$  with  $\mathbf{Z}_A = \mathbf{R}_A + j\mathbf{X}_A$ , the impedance matrix of the  $n$ -port (here two-port) antenna system and  $\mathbf{Z}_C = Z_c \mathbf{I}_n$  ( $\mathbf{I}_n$  is the identity matrix of dimension  $n$ ), the impedance of the RFID chip. The operator  $[\mathbf{Y}]_n$  denotes the  $n$ -th row (vector) of matrix

**Y**. The definition of  $\mathbf{g}$  (column vector of normalized antenna gain) in (5.7) is slightly different than the one presented in [22] in that it includes a  $\sqrt{\eta}$  factor ( $\eta = 120\pi$ ). The elements  $g_n$  of column vector  $\mathbf{g}$  are proportional to the radiated fields  $F_n$  at port  $n$  when a unit current excitation is applied at port  $n$  with all other ports open.

$$g_n = \sqrt{\frac{4\pi}{\eta}} F_n \quad (5.8)$$

Assuming a unit current excitation, the input power at port  $n$  is  $P_{in,n} = R_{A,nn}/2$ .

Considering the definition of antenna gain [73], the gain  $G_n$  is computed as follows

$$G_n = \frac{4\pi}{\eta R_{A,nn}} |F_n|^2 = \frac{|g_n|^2}{R_{A,nn}} \quad (5.9)$$

$R_{A,nn}$  denotes the self-resistance at port  $n$ . Using (5.9) and (5.7) one may write (5.6) as:

$$\frac{R_n}{R_0} = \sqrt{G_n \tau_n} \quad (5.10)$$

with

$$\tau_n = 4R_c R_{A,nn} \frac{|[Y]_n \mathbf{g}|^2}{|g_n|^2} \quad (5.11)$$

where  $\tau_n$  is the power transmission coefficient at port  $n$ , of the multiport system. One can easily verify that (5.11) reduces to (5.2) in the case of a single antenna.

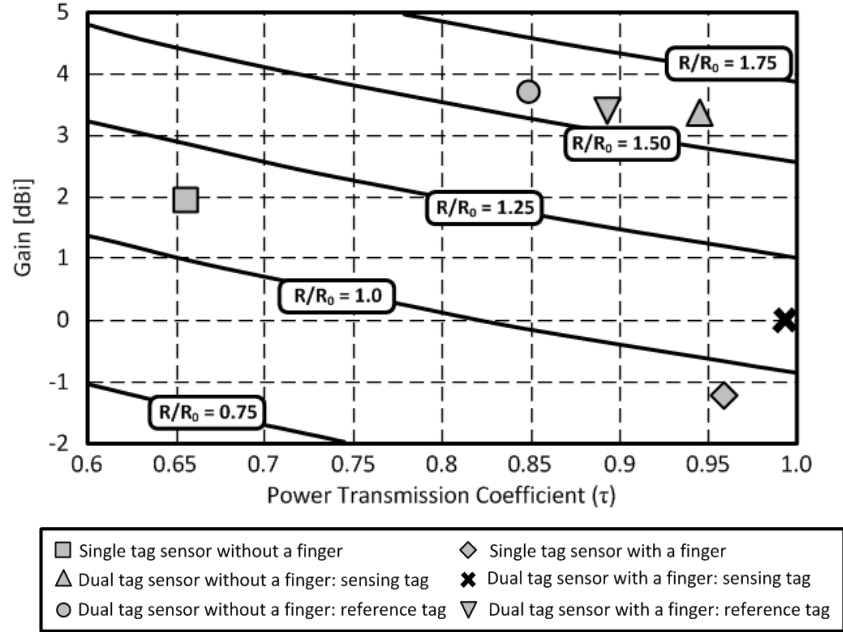


**Figure 5.10** Read range of the RFID-enabled sensor tags at 915 MHz.

The antenna impedance matrix  $\mathbf{Z}_A$  and far-field components  $F_n$  and consequently  $g_n$  can be obtained for example from a commercial EM simulator considering the tag antenna in the transmitting mode. In the case of the dual tag antenna presented in this work the matrix  $\mathbf{Z}_A$  is not symmetric due to the difference between the sensing and reference tag layouts. The estimated read range of the proposed RFID-enabled sensor tag is shown in Figure 5.10. The performance of the sensing tags (dual- and single tag sensors) has been significantly affected by the event while the reference tag of the dual tag sensor maintains its performance.

## 5.4 Experimental Results

### 5.4.1 Sensor Integration

As a proof-of-concept, the designed RFID-based haptic sensor tag was inkjet-printed on a commercially available photopaper, which was then sintered at 120 °C for 2 hours as

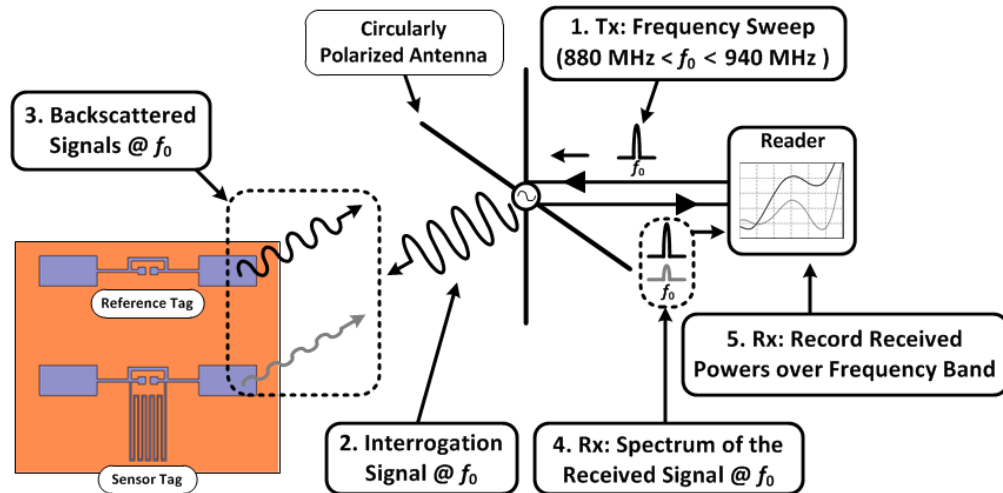


**Figure 5.11** Measurement procedure.

shown in Figure 5.8. The Voyantic Tagformance reader [74] was utilized in all measurements in the anechoic chamber. A circularly polarized panel antenna which has 8 dBi gain was utilized as the transmission (Tx) antenna of the RFID reader and the distance between the Tx antenna and the fabricated RFID-enabled sensor tag was about 60 cm (2 feet). The required minimum transmitted (Tx) power levels from the reader for the excitation of the RFID tags of the RFID-enabled sensor were recorded and plotted. The resolution of the frequency sweep was 1 MHz and the resolution of the Tx power was 0.1 dB. In this paper, an event occurrence is defined when a finger touches the meandered line of the antenna 1 (sensor tag).

The measurement setup and procedure are shown in Figure 5.11. A narrow band signal is transmitted to the RFID-enabled sensor and backscattered signals from the each tag are recorded at the frequency band of interest (820 MHz ~ 940 MHz). The whole procedure including frequency sweep and recording the received power takes less than 10 seconds with 1 MHz frequency step when the Voyance Tagformance reader is utilized. The received signals from each tag can be distinguished without collision because the reader can handle multiple tags when the RFID system follows EPC Gen2 protocol. The

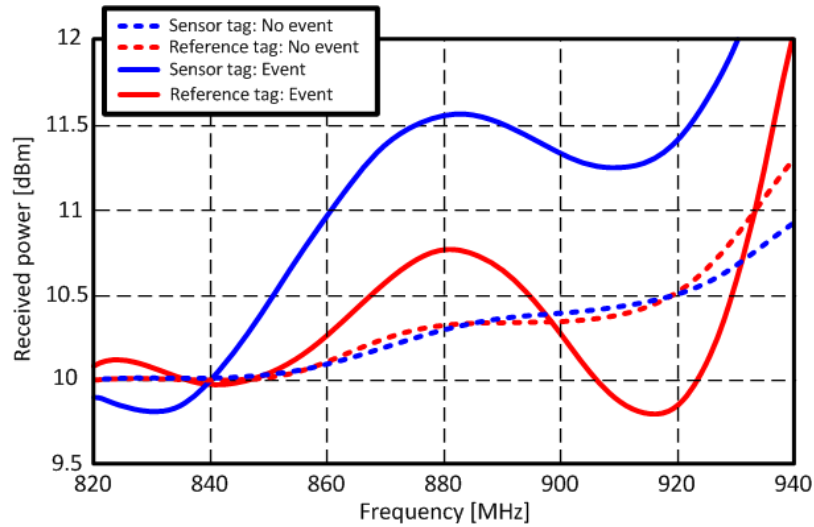


**Figure 5.12** Measured backscattered power from the each tag (antenna1, antenna2) before/after event occurrence.

received backscattered power level at the circularly polarized reader antenna was measured as shown in Figure 5.12. The RFID-enabled sensor which consists of two RFID tags was interrogated with 30 dBm power (FCC part 15 [75]) and the received power of the backscattered signal from each RFID tag by the reader was measured before/after an event occurrence. The gain of the RFID-enabled sensor is about 3 dBi, the interrogation distance is 0.6 m, and the required minimum power to activate the RFID chip is -15 dBm. The received power at the reader can be calculated using (5.1) with these link budget, giving the value of about 10.2 dBm at the center of the operation frequency range (880MHz), which is consistent. The calculated received power at the reader is about 10.2 dBm at the center of the operation frequency range (880 MHz) which is consistent with the data shown in Figure 5.11. The received power levels of the backscattered power from each antenna were almost the same when there was no event. However, a significant difference (up to 1.6 dB around 920 MHz) in the backscatter power level of the two

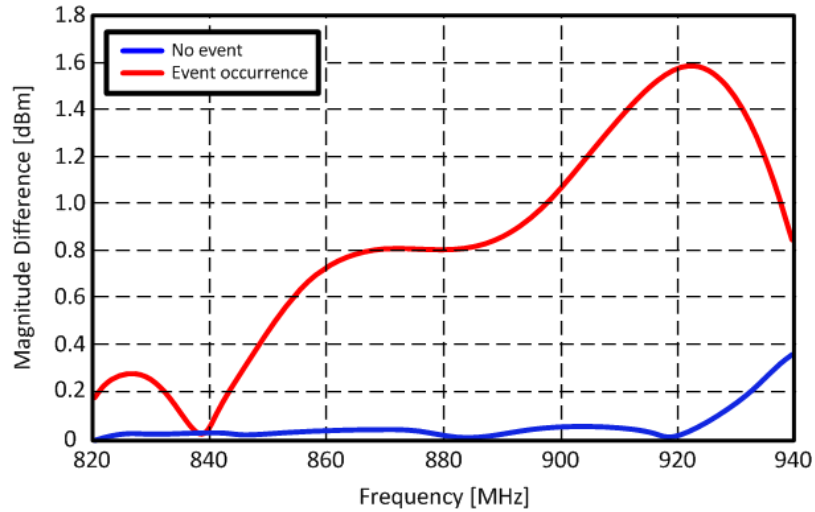


**Figure 5.13** Absolute power level difference between the antenna 1 (sensor tag) and the antenna 2 (reference tag) before/after the event occurrence.

antennas of the dual-tag sensor was observed upon the occurrence of an event such as touch. This response successfully demonstrates the feasibility of the proposed differential sensing mechanism through the use of very simple signal processing.

#### 5.4.2 Event Decision (Detection)

An event decision can be made based on the measurement curves shown in Figure 5.12. The absolute value of the magnitude difference between the two measured received power level curves after the event occurrence is much higher than that in the absence of any event as shown in Figure 5.13. For a more accurate event detection various sample data are collected over different frequency points. The sampled data correspond to different frequency values. The mean value ( $\mu$ ) and the standard deviation ( $\sigma$ ) of the sampled dataset experience significant changes before/after the event occurrence. The mean value ( $\mu$ ) and the standard deviation values ( $\sigma$ ) of the sampled absolute power level difference curves from the sensor tag (antenna 1) and the reference tag (antenna 2) before the event occurrence are almost identical due to the small differences between the



received power level curves (blue line in Figure 5.13) while those values are different after the event occurrence due to the noticeable differences between the received power level curves (red line in Figure 5.13). The correlation coefficient ( $\rho$ ) of the two datasets of the recorded (sampled) received power levels by the reader changes dramatically due to the significant changes of the mean values ( $\mu$ ) and standard deviation values ( $\sigma$ ) in the event of a touching incident. The Pearson product-moment correlation coefficient of the variable X and Y (PPMCC,  $\rho_{X,Y}$ ), which is commonly used to quantify the degree of the linear dependence and similarity of two variables in a simple way, indicates the linear dependence of two variables can be calculated as shown in (5.12) [76]. In addition, the PPMCC value is the same regardless of the magnitude of the curves, enabling a rugged sensing performance that is almost independent from the interrogation range and angle despite the fact that received power levels may vary significantly. It enables robust sensing because the behavior of each tag is independent from the interrogation distance and angle although the received power level may vary depending on those. In this work, the variable set X is the received power from the sensor tag (antenna 1) and the variable set Y is that from the reference tag (antenna 2) at the reader which are shown in Figure 5.12.

$$\rho_{X,Y} = \frac{cov(X,Y)}{\sigma_X\sigma_Y} = \frac{E[(X-\mu_X)(Y-\mu_Y)]}{\sigma_X\sigma_Y} \quad (5.12)$$

where  $cov(X, Y)$  is the covariance of the variables X and Y,  $\sigma_X$  and  $\sigma_Y$  are the standard deviation values of the variables X and Y,  $\mu_X$  and  $\mu_Y$  are the mean values of the variables X and Y, and  $E[\cdot]$  denotes the expectation value of the variable. The coefficient  $\rho_{X,Y}$  can

take any values between +1 and –1 inclusive according to the depending on the similarity of the variables. In case of a discrete dataset, which is the most common data form in most of the sensor systems, the correlation coefficient of (5.12) can be re-written as the sample correlation coefficient,  $r$ , (5.13) [76].

$$r = \frac{\sum_i^N (X_i - \bar{X})(Y_i - \bar{Y})}{\sqrt{\sum_i^N (X_i - \bar{X})^2} \sqrt{\sum_i^N (Y_i - \bar{Y})^2}} \quad (5.13)$$

where  $N$  is the number of the sample dataset,  $\bar{X}$  and  $\bar{Y}$  are the mean values of the datasets  $X$  and  $Y$ , respectively. In this paper, the magnitude of the correlation coefficient of the received power level curves can be considered as the similarity of the two curves [76]. The correlation coefficient value is close to +1 when the two curves are very similar while the value is getting lower as the absolute difference of the curves increases over the frequency of operation. The minimum required number of the sampled data points can be estimated based on the confidence interval ( $\beta$ ) and the chance of successful event detection ( $p$ ) as shown in (5.14) [77].

$$N \geq \frac{\ln(1-\beta)}{\ln(1-p)} \quad (5.14)$$

In this work, the 99% of confidence interval and 95 % of successful event detection are assumed and it requires more than 90 sample points, which is smaller than the number of data points used in calculating the correlation coefficient ( $r$ ). Typically, the sample correlation coefficient value before an event occurrence is 0.97, while it drops to 0.68

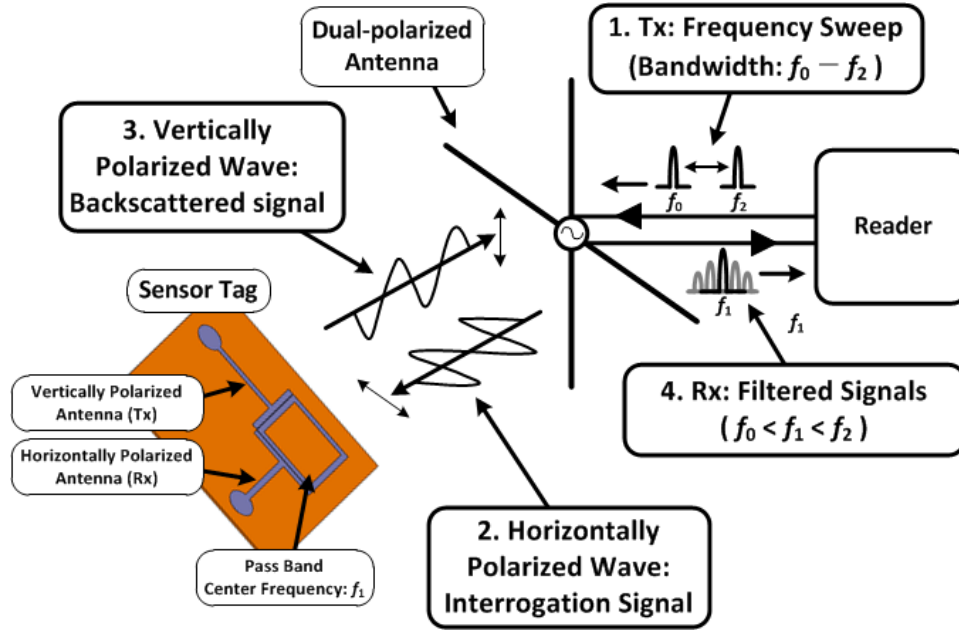


**Figure 5.14** Operation principle of the proposed RFID-based sensor platform.

after an event occurrence. The event occurrence decision can be made based on the abrupt change of the sample correlation coefficient at the reader side, with a value around 0.75 ~ 0.85 being used as the threshold for the detection.

## 5.5 Chipless RFID-Based Passive Fluid Sensor Platform

### 5.5.1 Operation Principle

The operation principle of the proposed RFID-based passive sensor system is depicted in Figure 5.14. The frequency band of 2.2 GHz ~ 2.6 GHz has been chosen because it includes the ISM band around 2.4 GHz, whereas the proposed design can be easily scaled up to any other frequencies. Due to the liquid-dependent capacitance change of the loaded capacitive gap of a microstrip square-ring resonator filter, the center frequency of the filter's pass band shifts lower when a high-dielectric material, such as water, is loaded on the gap. Two orthogonally polarized broadband microstrip monopole antennas are integrated with the filter to enable wireless interrogation by exploiting the

dual-polarization property. The horizontally polarized antenna (Rx antenna) receives a broadband pulse signal (bandwidth:  $f_2 - f_0$ ) in the frequency domain while the vertically polarized antenna (Tx antenna) reradiates a filtered broadband signal (narrowband signal at  $f_1$ ), and vice versa. The reader also utilizes a broadband antenna with the dual polarization to interrogate the dual polarized sensor platform. It interrogates the sensor platform with a broadband signal which has a bandwidth of  $f_2 - f_0$ , and receives the backscattered narrowband signal from the sensor platform at the frequency of  $f_1$ . The loaded material on the sensor platform can be detected by observing the shift of the center frequency of the backscattered narrowband signal that is strongly dependent on the relative dielectric constant ( $\epsilon_r$ ) of the loaded material on the filter's capacitive gap.

### *5.5.2 Capacitive Gap-loaded Tunable Filter*

The capacitive gap-loaded microstrip square ring resonator is the main sensing component of the proposed passive sensor tag. A square-shaped ring resonator has been chosen to achieve a dual polarization property by placing two linearly polarized antennas in an orthogonal configuration, while it allows for an easy fabrication. The perimeter of the resonator has been chosen to be equal to one wavelength ( $\lambda_0$ ) at the operation frequency of 2.6 GHz (center frequency for air-filled capacitive gap), and it should be optimized to resonate at desired operation frequency when the capacitive gap is introduced in the ring resonator. The capacitance introduced by the gap decreases the total capacitance of the ring resonator which results in shift of the resonant frequency to higher frequencies [78]. The chosen perimeter of the square-shaped ring resonator operating at 2.6 GHz is 198.8 mm which results in an edge length of 49.7 mm. The width (G) of the coupled feeding gap, that serves as the capacitive sensor, is the most

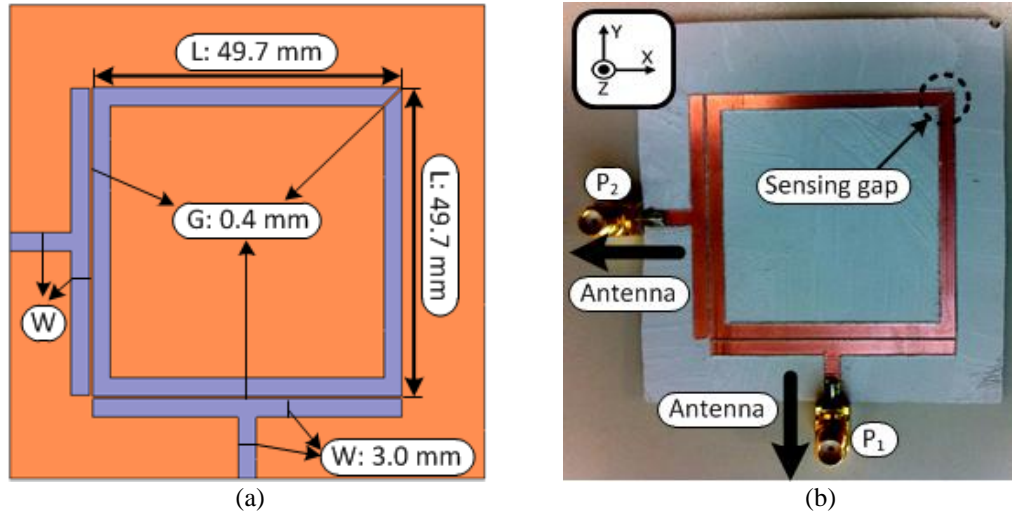


**Figure 5.15.** (a) Dimensions of the capacitive gap-loaded tunable ring resonator filter for capacitive sensing and (b) the fabricated prototype.

critical design parameter because it determines the center frequency of the filter's pass band. A narrower gap is better for low insertion loss (IL) because the coupling coefficient is inversely proportional to the width of the gap. Furthermore, the width of the capacitive sensor gap significantly affects the sensitivity of the sensor. Narrower gaps result in larger variation range of the capacitance depending on the loaded material as the capacitance increases. Thus, it is desirable to make the gap as narrow as possible in this kind of application. The chosen width of the coupled feeding and the capacitive sensor gap is 0.4 mm because of the fabrication limitations. The width of the feeding line and the ring resonator is chosen to be equal to 3 mm to keep the impedance of the microstrip line to  $50 \Omega$ . Figure 5.15 shows the geometry and the fabricated capacitive gap-loaded tunable filter. The filter is fabricated on RO3003 which has a relative dielectric constant ( $\epsilon_r$ ) of 3.0 and a loss tangent ( $\tan \delta$ ) of  $1.3 \times 10^{-3}$  utilizing a milling machine (LPKF ProtoMat S61).

The simulated and measured reflection coefficient ( $S_{11}$ ) and transmission coefficient ( $S_{21}$ ) are shown in Figure 5.16. The 3D full wave simulator, ANSYS HFSS v11.1, was

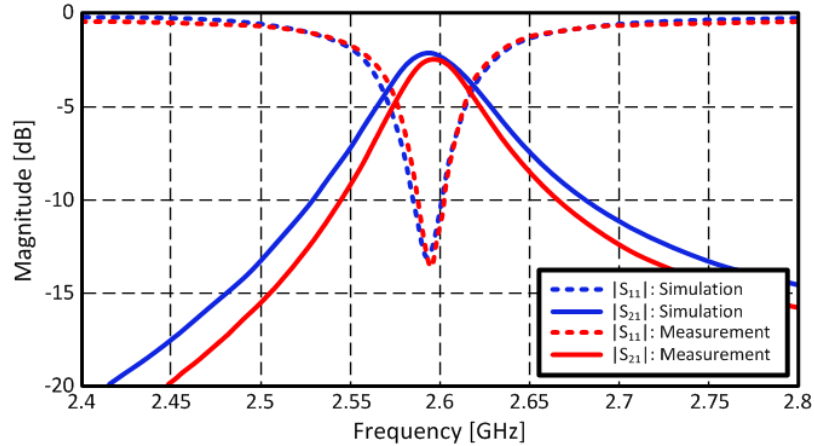


**Figure 5.16** Simulated and measured S-parameters ( $S_{11}$  &  $S_{21}$ ) of the tunable filter without fluid sample.

utilized to design the circuit. The measurements agree with the simulation result very well. The measured center frequency ( $f_0$ ) of the filter is 2.6 GHz and the 3 dB bandwidth is 54 MHz. The insertion loss (IL) of the filter at the center frequency ( $f_0$ ) is 2.47 dB. It can be improved by realizing a smaller gap between the tightly coupled feeding line and the square-ring resonator. Various fluid samples like acetone and water were loaded on the capacitive sensing gap to verify the performance of the designed filter as shown in Figure 5.17. The complex relative dielectric constants of acetone (99 % purity) and tap water are 19.1 ( $\tan \delta = 0.042$ ) and 73.0 ( $\tan \delta = 0.11$ ) at room temperature (300 K), respectively.

### 5.5.3 Broadband Antenna Design

A broadband linearly polarized antenna is required to receive and transmit a broadband signal from/to the reader. A microstrip monopole type antenna has been chosen because it features high axial ratio (AR) as well as it is easy to integrate with the designed microstrip square ring resonator filter without any transition. Plus, it has a relatively wide bandwidth compared to resonator-type antennas, such as a patch antenna.

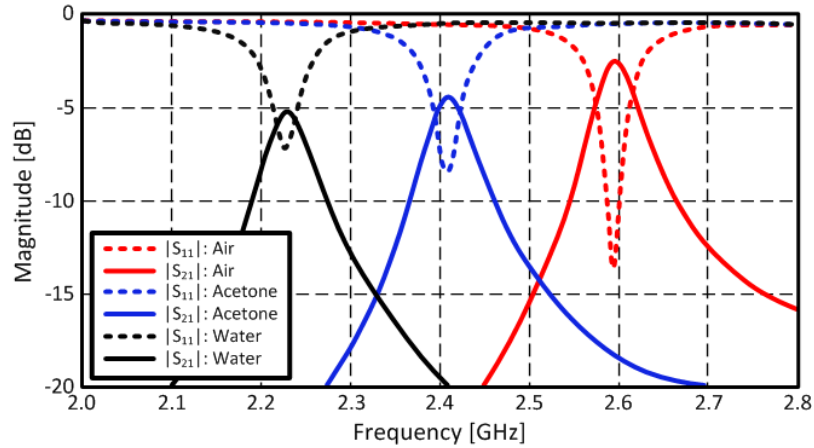


**Figure 5.17** Measured scattering parameters ( $S_{11}$  &  $S_{21}$ ) of the tunable filter with various fluid samples: acetone and water.

A circular disk is used as a load at the end of the monopole antenna to improve the bandwidth. The width of the monopole antenna is 3 mm which is the width of a 50  $\Omega$  microstrip line on 1.27 mm thick RO3003 (Figure 5.18). The length of the antenna has been chosen to be one quarter-wavelength ( $\lambda_0/4$ ) at 2.4 GHz, and the diameter (D) of the circular disk and the length ( $L_2$ ) of the dipole antenna have been optimized to cover the desired operation frequency band (2.2 ~ 2.6 GHz).

The geometry and the fabricated prototype of the disk-loaded microstrip broadband antenna on RO3003 (thickness: 1.27 mm) are shown in Figure 5.18. The antenna was fabricated utilizing the same milling machine. The simulated and measured (in an anechoic chamber) reflection coefficient ( $S_{11}$ ) of the antenna presented in Figure 5.19 show good agreement over the investigated frequency range. The small discrepancy results from the fabrication error. The dimensions of the fabricated antenna are slightly smaller by about 200  $\mu\text{m}$  than the designed dimensions due to the slightly larger metal removal during the milling process. The simulation result is obtained for the dimensions shown in Figure 5.18. The rough surface and edge which result from the milling

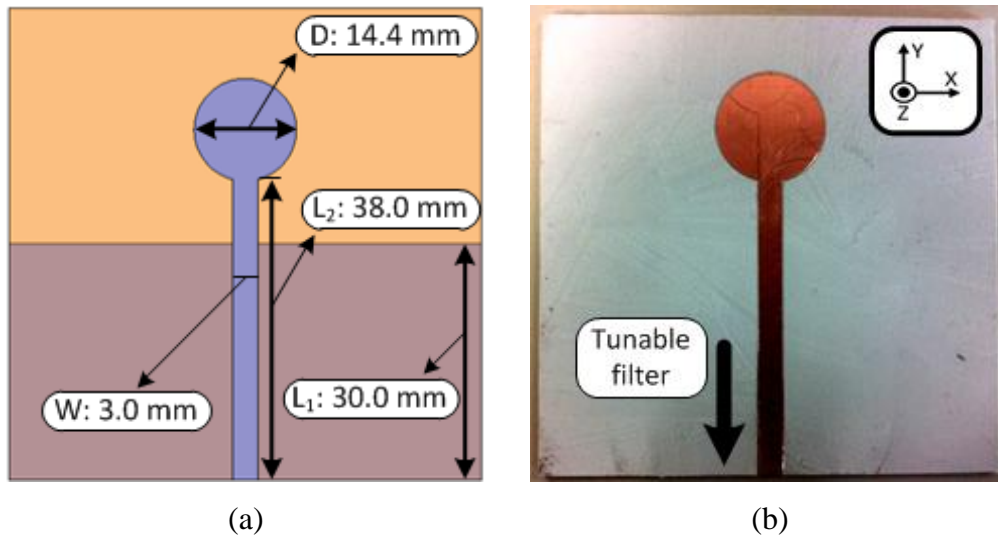


**Figure 5.18** (a) Geometry of the proposed microstrip monopole antenna and (b) the fabricated broadband antenna.

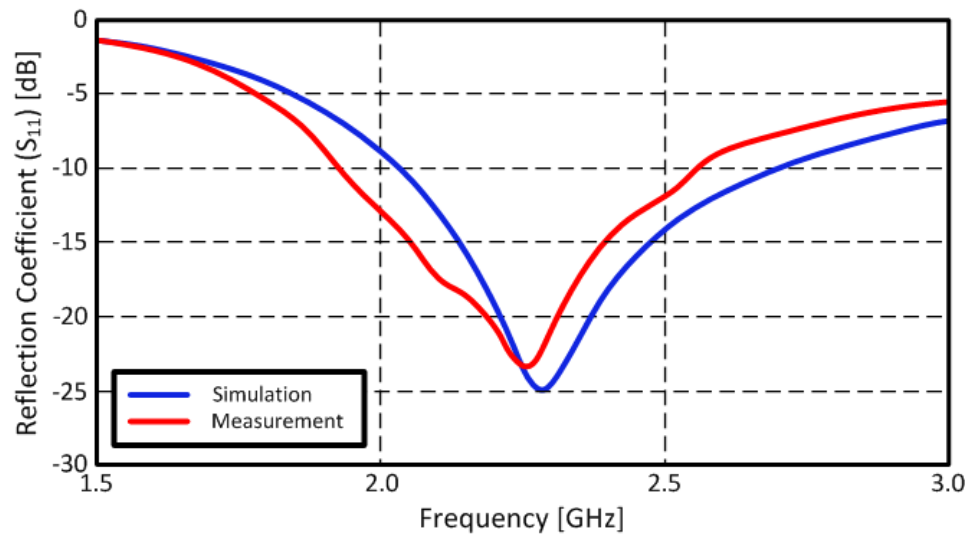


**Figure 5.19** Simulated and measured reflection coefficient ( $S_{11}$ ) of the microstrip monopole antenna.



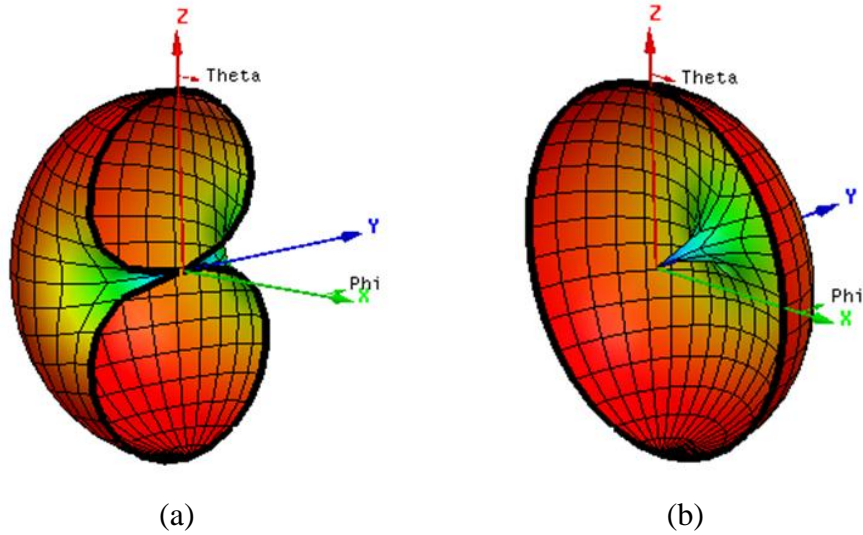


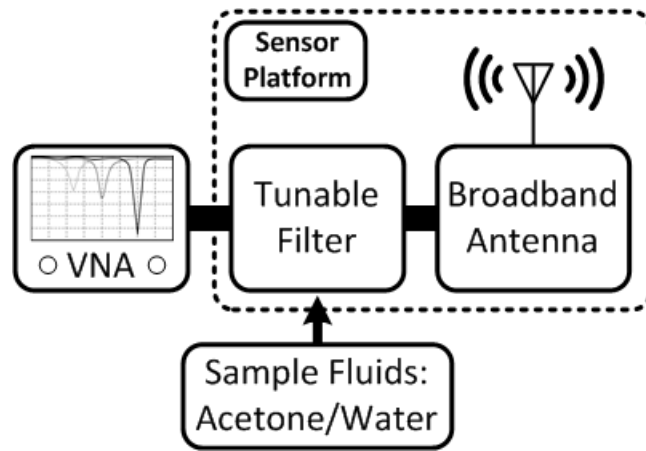
**Figure 5.20** Simulated radiation patterns on (a) E-plane (YZ-plane) and (b) H-plane (XZ-plane) at 2.24 GHz.

process also introduce unwanted parasitic effects. For the simulation, ANSYS HFSS v11.1 has been utilized. The resonant frequency of the antenna is 2.24 GHz and it has a fractional bandwidth of 27.9 % (625 MHz). The simulated radiation patterns on E-plane (YZ-plane) and H-plane (XZ-plane) at 2.24 GHz are shown in Figure 5.20. The antenna has an omnidirectional radiation pattern over the operation frequency range (2.2 GHz ~ 2.6 GHz). The calculated realized gain values of the antenna at 2.2 GHz, 2.4 GHz, and 2.6 GHz, which are the center frequencies of the loaded tunable filter with the gap filled with water, acetone, and air (no liquid) (Figure 5.17) are 2.78 dBi, 3.10 dBi, and 3.18 dBi, respectively. The simulated axial ratio (AR) of the antenna is 66.27 dB at bore-sight. The realized antenna meets every design specification, as it has been experimentally and theoretically verified.

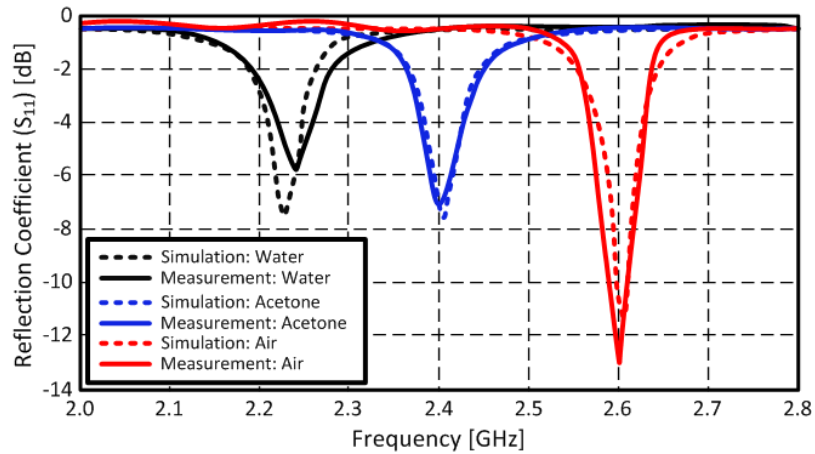
#### *5.5.4 Sensor Integration and Sensing Capability*

As a proof-of-concept demonstration of the fluid sensing capability, the designed broadband microstrip monopole antenna (Figure 5.18) has been integrated with the capacitive gap-loaded tunable filter (Figure 5.15). One port ( $P_1$ ) of the filter was connected to the antenna and the other port ( $P_2$ ) was connected to a VNA for the reflection coefficient ( $S_{11}$ ) measurement. Fluid samples (water and acetone) were loaded on the capacitive gap of the tunable filter and the frequency response was measured as shown in Figure 5.21. The simulation and measurement of the center frequency variation of the sensor platform (filter and antenna) depending on the sample fluids show very good agreement. The frequency shift of 200 MHz for acetone and 380 MHz for water is a drastically increased frequency shift compared to other reported similar RFID-based sensors [79][80]. To verify the performance of the proposed sensor in terms of repeatability, a series of similar measurements have been performed. The frequency responses retrieved have demonstrated a very close behavior.

In the final sensor platform, both  $P_1$  and  $P_2$  (Figure 5.15(b)) are connected to antennas. The broadband signal from the reader is received by the horizontally polarized antenna, and the broadband signal is filtered by the tunable filter which has a liquid-dependent center frequency. The vertically polarized antenna reradiates the filtered narrowband signal to the reader (Figure 5.14). Without a fluid sample, the reflection coefficient value is less than -10 dB at the operation frequency which results in more than 90 % of power to be delivered to the vertically polarized antenna (Figure 5.21). The high axial ratio (66.27 dB) of the antennas helps suppress the unwanted re-radiation from the horizontally polarized antenna in the vertical polarization. The interrogation range of the



(a)



(b)

**Figure 5.21** (a) The measurement setup of the designed sensor platform (the tunable filter and the antenna) and (b) the simulated and measured reflection coefficient ( $S_{11}$ ) of the chipless sensor platform with different fluids.

proposed sensor platform can be estimated based on the measured insertion loss of the filter and the calculated antenna gains. The estimated interrogation range is 5.33 m in free space assuming the reader sensitivity is below -60 dBm (sensitivity of commercial RFID reader) with a transmission power of 30 dBm (FCC regulation [75]) from a reader antenna with a gain of 6 dBi.

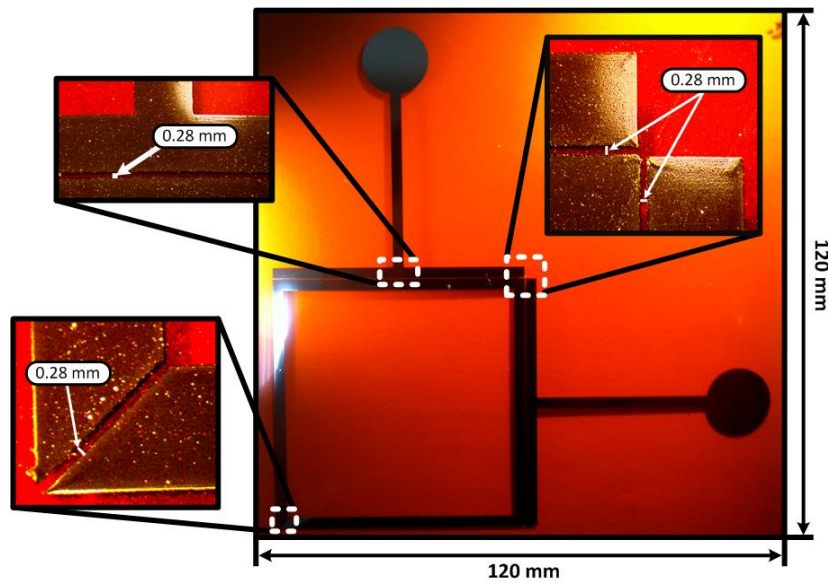


**Figure 5.22** The inkjet-printed chipless RFID-based fluid sensor platform on a Kapton substrate.

### 5.5.5 Inkjet Printing of the Sensor Platform

It is important to implement the hereby introduced liquid sensing platform on flexible substrates in order to allow for rugged surface mounting, such as for instance cylindrical pipelines. Subtractive fabrication methods, such as milling and etching, are widely utilized for prototyping due to its ease of feature size control. However, the milling technique is not suitable for thin flexible substrates because its drill bit may damage the substrate. The etching technique can handle a thin flexible material but it utilizes strong acids to wash away the metals and requires masks for patterning. In this case, an additive method like the inkjet printing technology has great potential to implement a low cost environmentally friendly flexible sensor platform because it does not produce any byproducts by just printing the conductive ink on the desired position with an easily controlled amount volume of ink. Figure 5.22 shows the picture of an inkjet-printed prototype of the proposed sensor platform on Kapton, that demonstrates the

realization feasibility of highly scalable low-cost flexible "green" wireless liquid sensors with enhanced sensitivity.

## **5.6 Summary**

In this chapter, novel inkjet-printed RFID-enabled sensors for the printed autonomous sensor platform are presented. The concept and operation principle of RFID-enabled sensor are discussed. Two types of RFID-enabled sensor with/without an RFID chip are presented and their performances are experimentally tested. A dual-tag calibration free RFID-enabled sensor design is proposed and printed planar LC resonators are integrated to the sensor tag to suppress the crosstalk. Its decision method is discussed based on PPMCC.

A chipless RFID-based passive fluid sensor platform is also presented in this work. It utilizes vertical and horizontal polarized antennas to discriminate interrogation and reflected signals. A resonant frequency of the capacitive gap-loaded tunable filter is varied depending on the loaded fluid at the gap resulting in sensing capability of the sensor platform.

The RFID-enabled sensors are a critical part of the autonomous wireless sensor platform because the RFID-enabled sensors can be easily implemented without complex electronics and they require low power to operate the whole sensor system.

## CHAPTER 6

### INKJET-PRINTED VIAS AND SIW COMPONENTS

#### 6.1 Introduction

Inkjet-printed wireless power transmission devices, RFID-based sensors, and microwave components for high speed communications are actively investigated and successfully demonstrated [9][81]. However, most of these works are single-layered structures because it is challenging to implement vias which are one of the most critical factors for the realization of highly integrated systems and multi-layered structures.

In this chapter, the implementation of vias on paper and a thick substrate (thickness  $> 100 \mu\text{m}$ ) is presented for the first time. Only a small number of technologies for implementing vias utilizing inkjet printing technology have been reported, all of which have been implemented on very thin substrates with thickness below  $100 \mu\text{m}$  [10][12]. Such thin substrates are not suitable for applications in relatively lower frequency bands, such as mobile, WiFi, ISM, etc. The feature size of microwave components such as the width of microstrip line is very narrow on the thin substrate, which results in very high design sensitivities to fabrication tolerances. The radiation efficiency of antennas, like patches, resonators and waveguide structures, such as substrate-integrated waveguides (SIW), is significantly affected by the substrate thickness [82]. Therefore it is necessary to develop via fabrication concepts or techniques which can be applied on a range of different thicknesses. The major issue in the metallization of via holes utilizing inkjet printing technology is to maintain a continuous metal layer after the sintering process, which is challenging because the inkjet-printed silver nanoparticles shrink during

sintering. The via hole topology with an exponentially tapered profile is introduced in order to facilitate the formation of continuous metal layers using conductive inks.

As a proof-of-concept demonstration of the proposed inkjet-printed stepped via and copper vias on paper configuration, SIW structures, such as a  $\mu$ strip-to-SIW interconnect and a SIW slotted waveguide antenna, are presented on the polymethyl methacrylate (PMMA) substrate and paper. SIW structures require a large number of vias, which makes them good benchmarking structures to test the repeatability and performance of the proposed stepped vias. PMMA, which is also known as plexiglass or acrylic, is a widely used commercial polymer material for numerous applications such as display devices and medical instruments due to its high transparency and good compatibility with human tissue [83]. In addition, PMMA can be utilized as a dielectric layer for transistors realized using inkjet printing [84]. The application spectrum of PMMA and paper is getting wider and wider due to their aesthetic characteristics and bio-compatibility as those properties are important factors of electronic devices for the modern wireless applications. Therefore, PMMA and paper are chosen as substrates, and the proposed via topologies are implemented on those substrates. Plus, the demonstration of the first fully inkjet-printed SIW structures suggests the importance of inkjet-printing technology toward implementing the system-on-substrate (SoS) concept in communication, sensing and Internet of Things (IoT) applications.

## **6.2 Inkjet-printed SIW Components on Paper**

### *6.2.1 Via Fabrication on Paper*

The drilling and laser processing are suitable processing for the paper substrate among many via hole fabrication technologies because those are complete dry processes

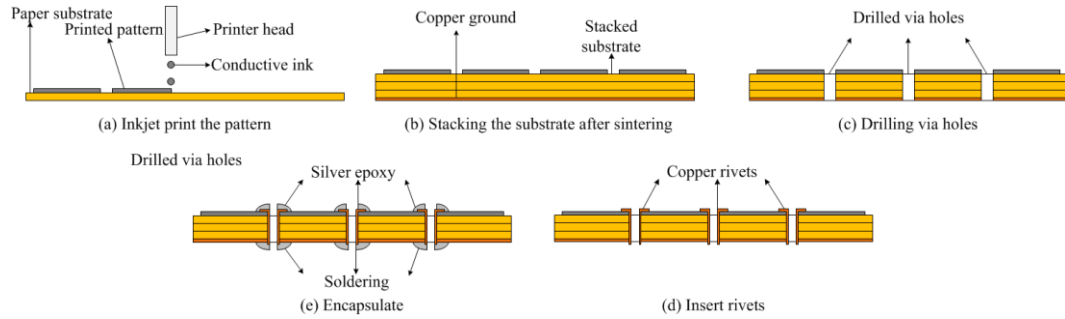


**Figure 6.1** Via metallization on paper.

and no surface treatments are required. In addition, those processes have good aspect ratios and feature sizes. The aspect ratios of drilling and laser processing are larger than 10 and 20, respectively. The general achievable feature size of drilling is 300  $\mu\text{m}$  and of laser processing is 5  $\mu\text{m}$ .

In this work, a mechanical drill is utilized to make via holes since it does not damage the substrate and the rim of via holes. Some blackening is observed around the via hole when the laser processing is utilized. This may degrade the performance of the inkjet-printed circuits on paper substrate, since the electric properties of the burnt area are different from its original properties.

For the via hole metallization, cylindrical copper rivets are utilized. In previous works, via holes were metallized using conductive epoxy or printing conductive ink over and over [10][11]. The epoxy filled via hole cannot guarantee a tight contact to the side wall of the via hole or the roughness of the metallized via hole. The ink filling technique cannot be applied to a thick substrate, and in the case of a paper substrate it appears critical, since paper absorbs ink during the printing process. For achieving a repeatable and stable via hole metallization, a cylindrical copper rivet with outer diameter of 0.8 mm is inserted into the via hole.



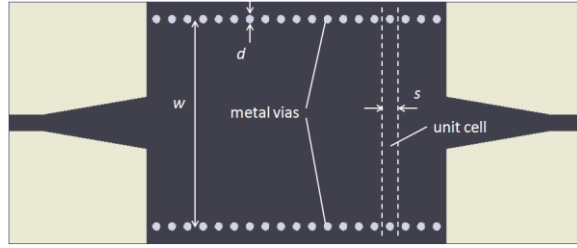


**Figure 6.2** Geometry of a SIW interconnect on paper.

The whole fabrication process is depicted in Figure 6.1. For the first step, the SIW structure is printed on the single layer of paper substrate. Two more layers of paper substrate are stacked to get the desired substrate thickness of 0.69 mm after sintering the printed pattern. The PolyVinylPyrrolidone (PVP) based glue is utilized to bond the paper substrates because of ease of fabrication and its electrical permeability is similar to that of the paper [82]. The copper ground plane is bonded, and via array is drilled. The top and bottom of the via hole are covered with conductive epoxy or soldering to improve the contacts after filling the via holes with the cylindrical copper rivets.

### 6.2.2 Inkjet-printed $\mu$ Strip-to-SIW Interconnect

A straight 25 mm long SIW interconnect on paper has been implemented. The SIW lines have been designed for an operation frequency of 5 GHz, and for this reason the cutoff frequency of the fundamental mode was set to  $f_0 = 3.75$  GHz. This performance is achieved by properly selecting the geometrical dimensions of the SIW structure (Figure 6.2). The width of the SIW ( $w$ ) is 24 mm, the diameter of metal vias ( $d$ ) is 0.8 mm and their pitch ( $s$ ) is 1.6 mm. The dimensions of the pitch and the diameter of the holes were chosen to avoid the radiation leakage as well as to minimize fabrication inaccuracy.

The substrate thickness is about 0.69 mm, which is obtained by stacking 3 layers of paper (each of them with a thickness of 0.23 mm). As conductor loss can be minimized

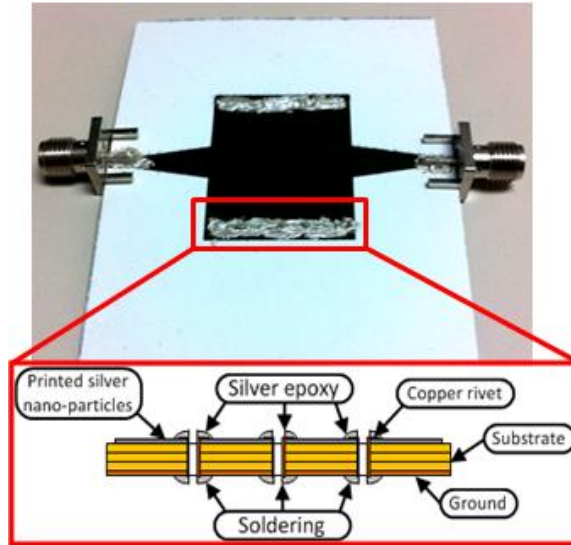


**Figure 6.3** Fabricated SIW interconnect on paper.

by increasing the substrate thickness [82], this thickness has been chosen reasonably large to reduce the loss component due to the relative low ink conductivity. The structures have been designed, considering the nominal relative values of the dielectric constant ( $\epsilon_r$ ) of 3, the loss tangent ( $\tan \delta$ ) of 0.06, and the ink conductivity ( $\sigma$ ) of  $1.5 \times 10^7$  S/m.

A picture of the fabricated paper SIW is shown in Figure 6.3. The scattering parameters of the three SIW structures have been experimentally determined as shown in Figure 6.4. The estimated insertion loss (IL) of the SIW is 0.5 dB/cm at 5 GHz while each microstrip-to-SIW transition and connector have an additional IL of about 0.5 dB. The small discrepancies between theory and measured data are attributed to repeatability issues in the fabrication of the different SIW interconnects. In particular the difference near the cutoff frequency is attributed to the radiated coupling between the microstrip-to-SIW transitions. In fact, a small portion of the power radiated by the transition is received by the other one.

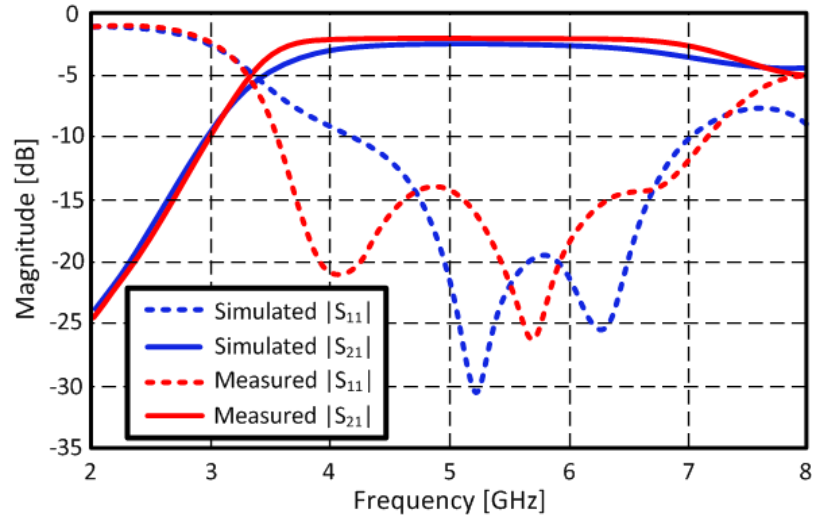


**Figure 6.4** Measured S-parameters.

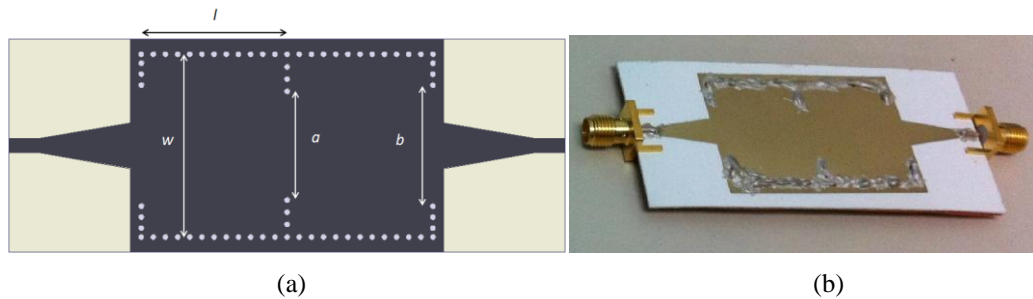


**Figure 6.5** (a) Geometry of the SIW filter and (b) the fabricated filter on paper.

### 6.2.3 Inkjet-printed SIW Cavity Filter

A two-pole SIW cavity filter was designed and measured to investigate the feasibility of SIW components on paper substrate. The topology of this filter is simple: it comprises two cavities which are coupled by an iris. The geometry and fabricated SIW cavity filter are presented in Figure 6.5. The simulated and measured S-parameters of the filter are reported in Figure 6.6, with a measured insertion loss (IL) of about 5 dB at 5 GHz. These results show that losses represent an issue, and the performance of the filter is affected by the significant losses of the material. For this reason, the filter topology needs to be carefully selected for the effective implementation of SIW filters on paper.

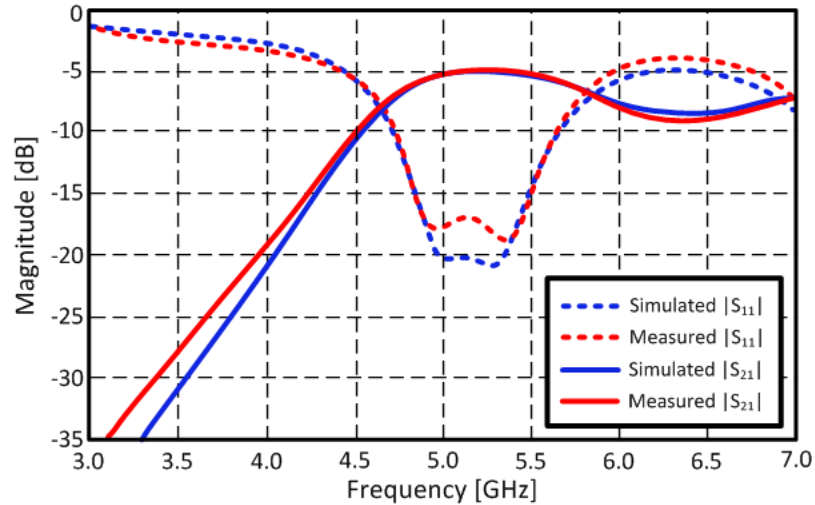


**Figure 6.6** Simulated and measured S-parameters of SIW filter on paper.

Possibly, the use of pre-distorted filter configurations could represent an interesting solution and partially mitigate this issue [85].

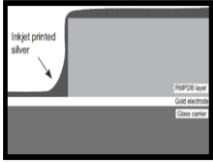
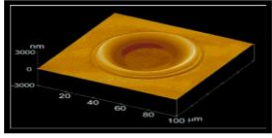
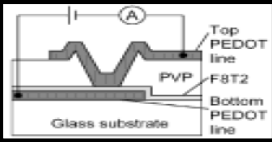
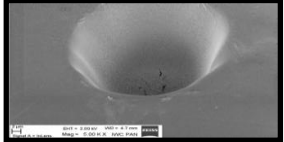
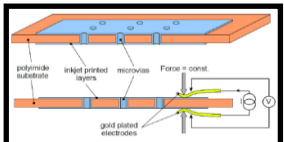
## 6.3 Inkjet-printed Via

### 6.3.1 Challenges

In previously reported work, inkjet-printed via holes have been successfully implemented on very thin substrates [10-12], as shown in Table 6.1. In [10], 3 layers of silver nanoparticles are inkjet-printed over the thin vertical wall utilizing a 50 pL cartridge. In [11], a crater-like via hole is made by inkjet printing an ethanol drop to dissolve a polyvinyl phenol (PVP) layer. In [12], a microvia array, which consists of small laser-drilled microvias, is presented on polyimide substrate. The proposed stepped via approach (with a 2 mm diameter) achieved the thickest via thickness of 1 mm with good via resistance of  $7.4 \pm 2 \Omega$  compared to the reported works.

It is very challenging to metalize via holes on relatively thick substrate. If the via holes are metalized with a similar approach to other inkjet-printed structures, i.e. printing

**Table 6.1** Inkjet-printed vias.

	In [10]	In [11]	In [12]
<b>Via length (<math>\mu\text{m}</math>)</b>	25 ~ 65	0.5	100
<b>Via diameter (<math>\mu\text{m}</math>)</b>	N/A	0.75	65
<b>Via resistance (<math>\Omega</math>)</b>	$1.9 \pm 0.1$	$5 \times 10^5$	0.52
<b>Geometry</b>		 	 

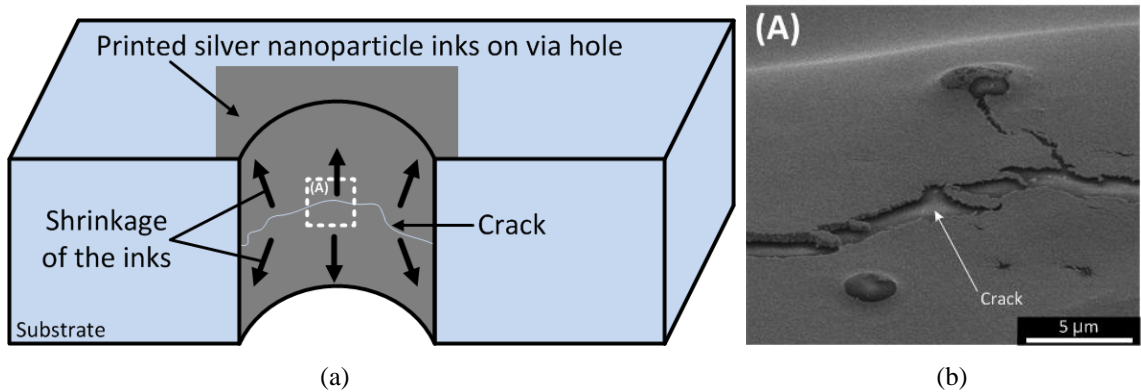


**Figure 6.7** (a) Crack formation of inkjet-printed silver nanoparticle on the vertical via hole and (b) SEM image of the crack on the metalized via hole.

multiple layers on drilled via holes, it results in discontinuities, as shown in Figure 6.7. For demonstration purpose, a straight via hole was drilled on 1 mm thick PMMA using CO<sub>2</sub> laser, and silver nanoparticles were printed over the via hole 5 times. The printed via hole is sintered at 120 °C for 2 hours. The printed silver nanoparticles failed to form a continuous metal layer on the via hole due to the shrinkage of the silver ink during the sintering process due to the evaporation of the solvents, the polymers (a dispersant on the

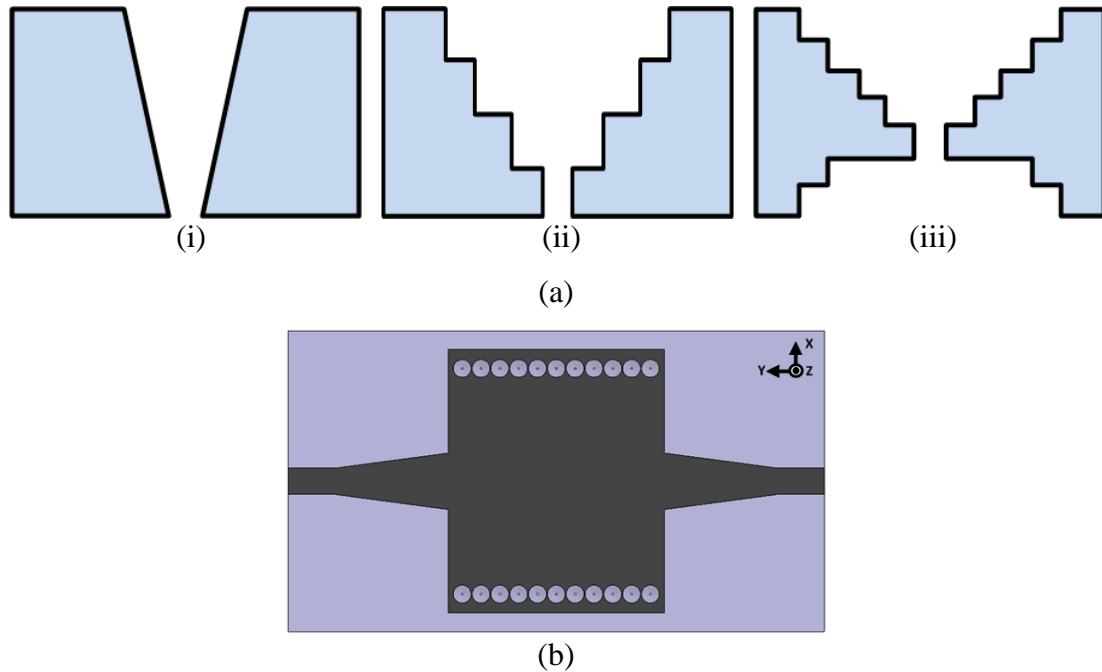


**Figure 6.8** (a) Proposed via profiles and (b) testing SIW structure.

silver nanoparticles) and the impurities of the ink. The gravity force further enhance the downward shrinkage of the ink, which results in cracks on the metalized via wall. The shrinkage of the inkjet-printed silver nanoparticles on the vertical via wall is briefly depicted in Figure 6.7(a). The inkjet-printed silver nano-particles on the vertical wall are shrinking in different directions, and this results in cracks as shown in Figure 6.7(b).

### 6.3.2 Stepped-via Topology

A stepped via hole is introduced in order to create a gradual transition between the top and the bottom planar substrate surface and reduce the stress on printed silver nanoparticles on the via hole during the sintering process, that are typically detrimental for the performance of uniform vias. The three types of via holes are investigated: a conical (Figure 6.8(a)-(i)), a single side stepped (Figure 6.8(a)-(ii)), and a double side stepped (Figure 6.8(a)-(iii)) via profile. The proposed via profiles

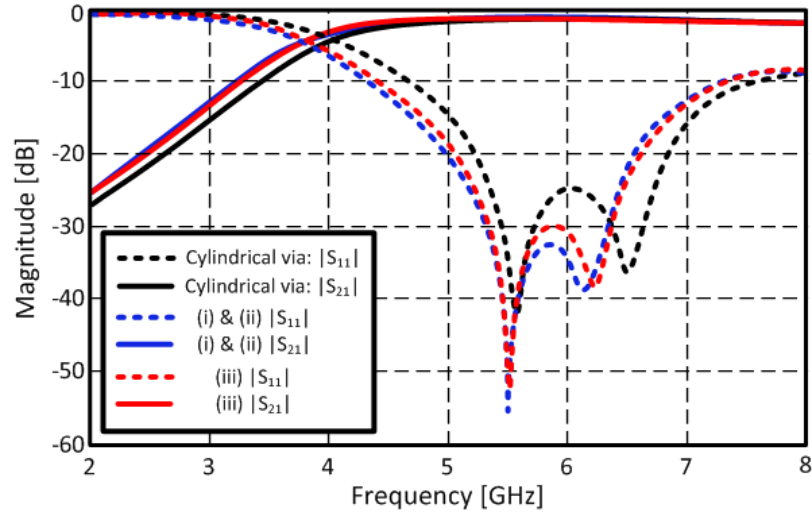


**Figure 6.9** Simulated S-parameters ( $S_{11}$  &  $S_{21}$ ) of the testing SIW structure with the proposed via profiles.

are implemented on a  $\mu$ Strip-to-SIW interconnect to investigate the effect of the via profiles (Figure 6.8(b)). The simulated S-parameters ( $S_{11}$  &  $S_{21}$ ) of the SIW interconnect with the proposed via profiles are shown in Figure 6.9. It should be noted that the via profiles minimally affect the frequency response of the SIW interconnect but the cut-off frequency has slightly shifted to a lower frequency due to the parasitic inductance and capacitance of the stepped and conical via profile. The conical via profile is simpler than other via topology but it is challenging to realize a smooth conical shape on a polymer substrate without using a wet process such as chemical etching. The proposed stepped via topologies (Figure 6.8(a)-(i),(ii)) are feasible and compatible with dry fabrication process, such as laser drilling and mechanical milling. However, the yield of the single side stepped via topology (Figure 6.8(a)-(ii)) was much lower than the double side stepped via topology (Figure 6.8(a)-(iii)) when the inkjet printing technology is utilized since the metallization of the sharp transition from the via to the bottom is challenging. In this work, the double side stepped via hole (Figure 6.8(a)-(iii)) is thoroughly investigated.

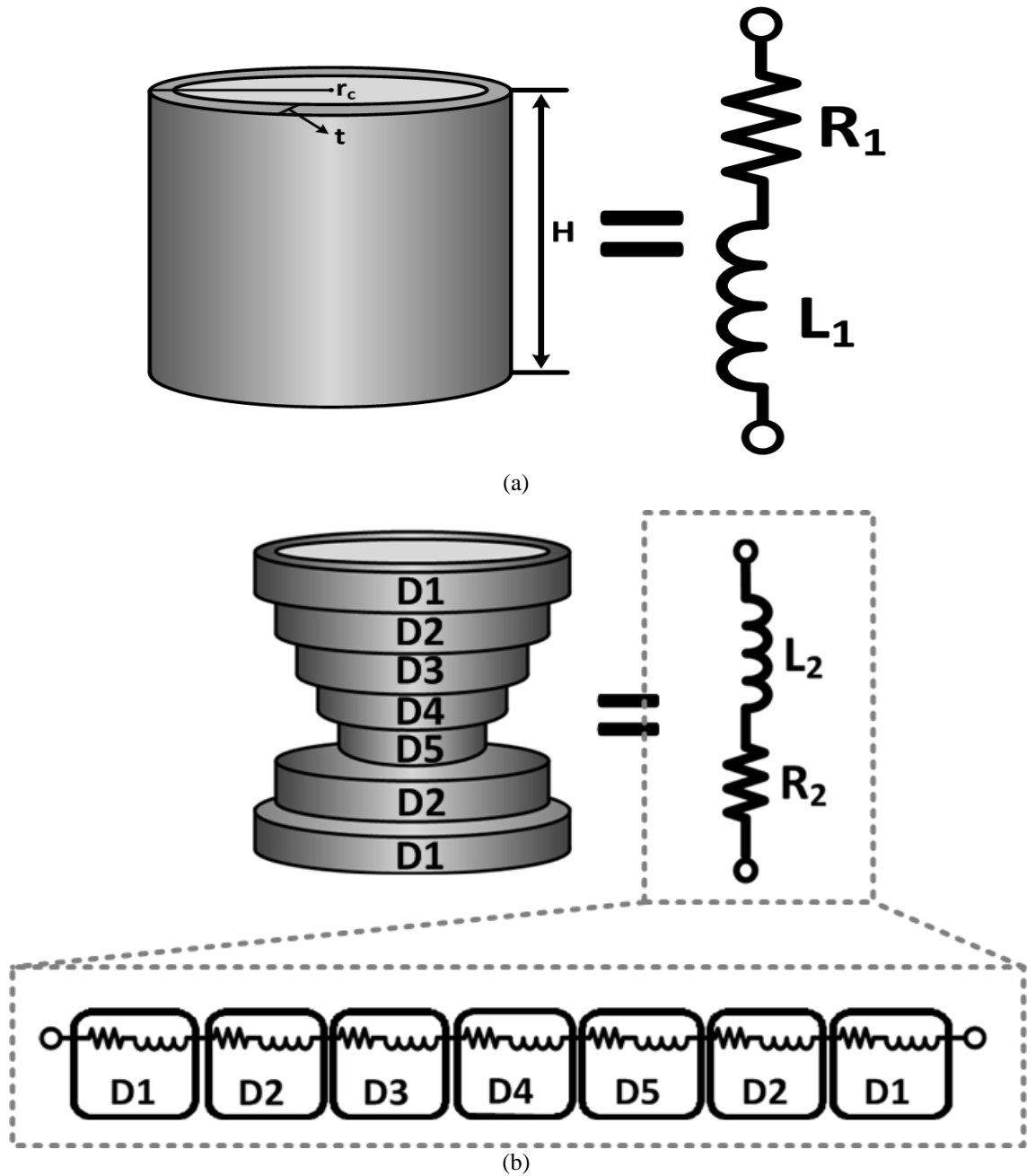


**Figure 6.10** Equivalent circuit model of (a) a cylindrical via and (b) a stepped-via.

### 6.3.3 Stepped-via Modeling

A typical cylindrical via can be modeled as an inductor and a resistor in series as shown in Figure 6.10(a). The proposed stepped via (Figure 6.10(b)) can be considered as a series of cylindrical vias modeled in Figure 6.10(a). For the model simplicity, cylinders on the bottom side are chosen to have the same dimensions with the cylinders on top



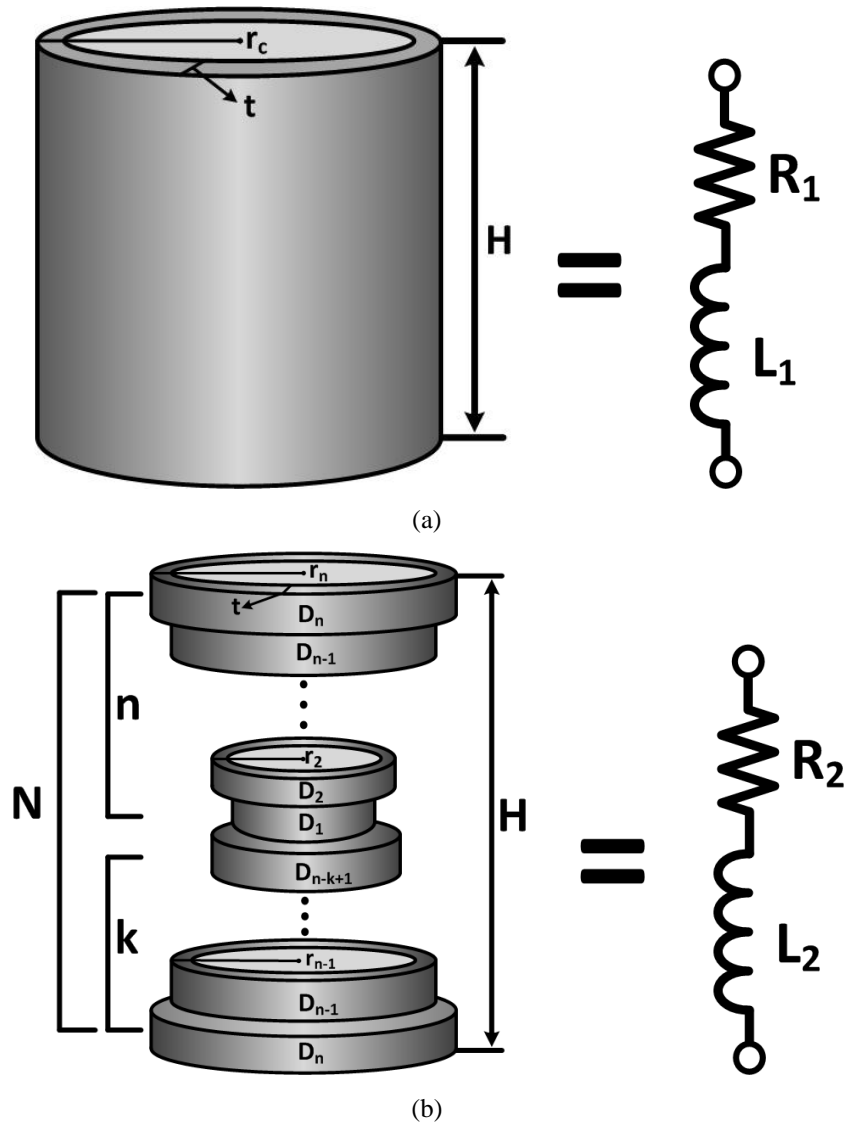


**Figure 6.11** Generalized (a) cylindrical via and (b) stepped via circuit model.

(Figure 6.10(b)). The inductance of horizontal contacts is negligible because of the thin metal thickness. The generalized cylindrical and the stepped via are shown in Figure 6.11 and their equivalent circuit model (inductance and resistance) is derived based on the geometry of the vias. An inductance value ( $L_1$ ) and a resistance value ( $R_1$ ) of a straight cylindrical via can be expressed as shown in (6.1) and (6.2).

$$L_1 = \frac{\mu_0 H}{4\pi} f(r_c, t) \quad (6.1)$$

$$R_1 = \frac{H}{\sigma\pi} g(r_c, t) \quad (6.2)$$

where

$$f(r_c, t) = \frac{1}{(r_c^2 - (r_c - t)^2)} \left[ (r_c^2 - (r_c - t)^2) - 2(r_c - t)^2 \ln \frac{r_c}{r_c - t} \right] \quad (6.3)$$

$$g(r_c, t) = \frac{1}{t(2r_c - t)} \quad (6.4)$$

Similarly, the circuit model ( $L_2$  &  $R_2$ ) of the proposed stepped via hole can be modeled based on (6.1) ~ (6.4).

$$L_2 = \frac{\mu_0 h}{4\pi} \left[ 2 \sum_{i=n-k+1}^n f(r_i, t) + \sum_{i=1}^{n-k} f(r_i, t) \right] \quad (6.5)$$

$$R_2 = \frac{1}{\sigma\pi} \left[ h \left( \sum_{i=1}^n g(r_i, t) + \sum_{i=n-k+1}^n g(r_i, t) \right) + \sum_{i=1}^{n-1} h(r_{i+1}, r_i, t) + \right. \\ \left. \sum_{i=n-k+1}^{n-1} h(r_{i+1}, r_i, t) \right] \quad (6.6)$$

where

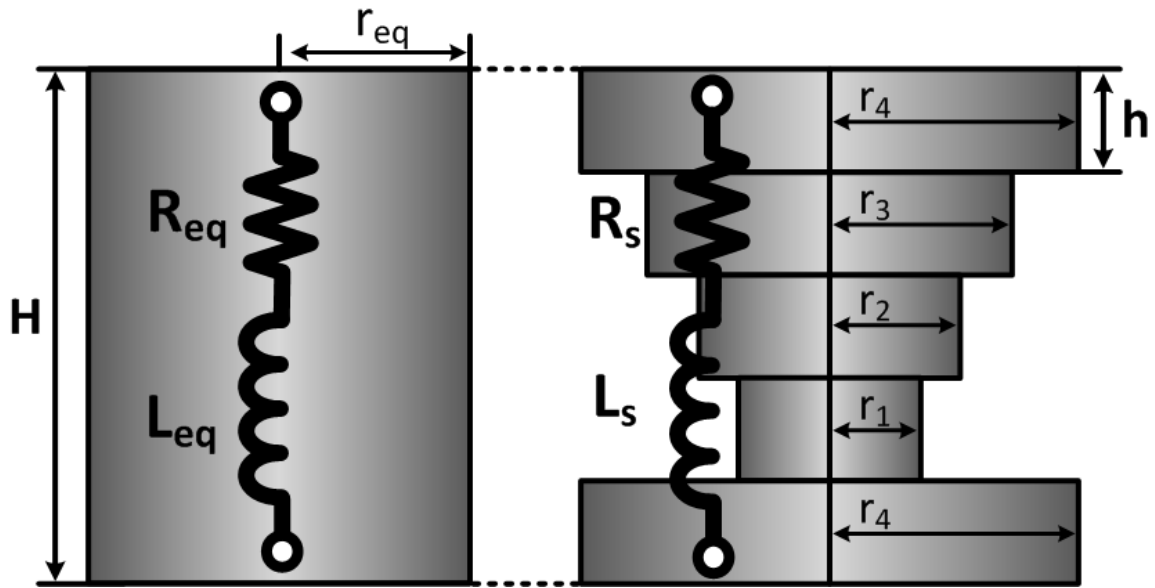
$$N = n + k \quad (6.7)$$

$$f(r_i, t) = \frac{1}{(r_i^2 - (r_i - t)^2)} \left[ (r_i^2 - (r_i - t)^2) - 2(r_i - t)^2 \ln \frac{r_i}{r_i - t} \right] \quad (6.8)$$

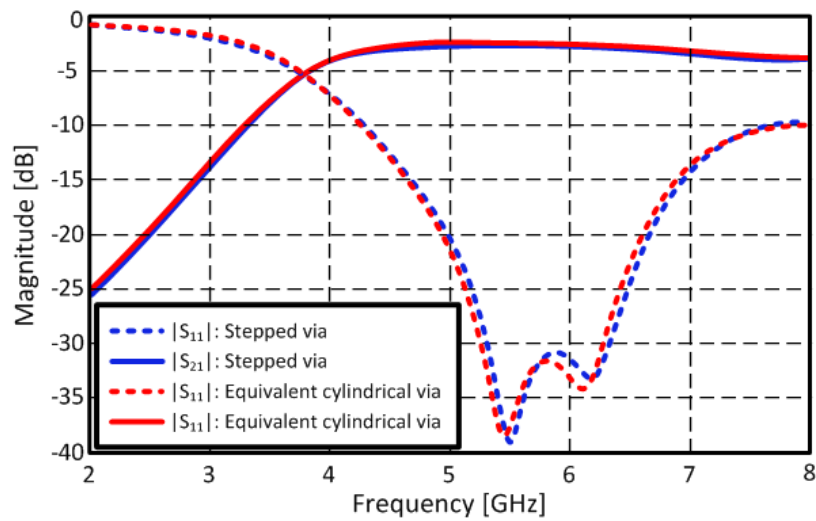
$$g(r_i, t) = \frac{1}{t(2r_i - t)} \quad (6.9)$$

$$h(r_{i+1}, r_i, t) = \frac{1}{(r_{i+1} - t)^2 - (r_i - t)^2} \quad (6.10)$$

The proposed stepped via topology is easy to fabricate utilizing inkjet printing technology but it is impractical to model every stepped via in full wave 3D simulators, such as HFSS and CST, due to the complexity of the stepped model resulting in large computation resources and long calculation time. It would be convenient to design a cylindrical via model in which the inductance and resistance are the same as the fabricated stepped via. The 5 stepped via is assumed as presented in Figure 6.12(a). The height of the each cylinder ( $h$ ) is 200  $\mu\text{m}$ , the radius of the largest cylinder ( $r_4$ ) is 1 mm, and the metal thickness ( $t$ ) is set to 70 nm with a conductivity value of  $6 \times 10^5$  S/m. The radii are exponentially tapered ( $r_{n+1} = e r_n$ ). The equivalent circuit model ( $L_{\text{eq}}$  &  $R_{\text{eq}}$ ) of the cylindrical via is designed based on (6.1) ~ (6.10). The equivalent radius ( $r_{\text{eq}}$ ) of the cylindrical via is 500  $\mu\text{m}$  with a thickness of 1.8  $\mu\text{m}$  and a conductivity value of  $7.3 \times 10^5$  S/m. The designed equivalent circuit model of the cylindrical via has the same inductance and resistance ( $L_{\text{eq}}$  &  $R_{\text{eq}}$ ) with those of the stepped via ( $L_s$  &  $R_s$ ). The equivalent via model is able to simplify the whole circuit model and save computational resources. The simulated equivalent via and stepped via models are shown in Figure 6.12(b) and the results are in very good agreement.



(a)



(b)

**Figure 6.12** (a) Concept of equivalent via model and (b) simulated model comparison

### 6.3.4 Stepped-via Fabrication

The fabrication process of the proposed double side stepped via hole is described in Figure 6.13. A thin concentric circular cylinder is engraved on the substrate to form a stepped via profile (Figure 6.13(i), (ii)). Then, the substrate is flipped to drill another

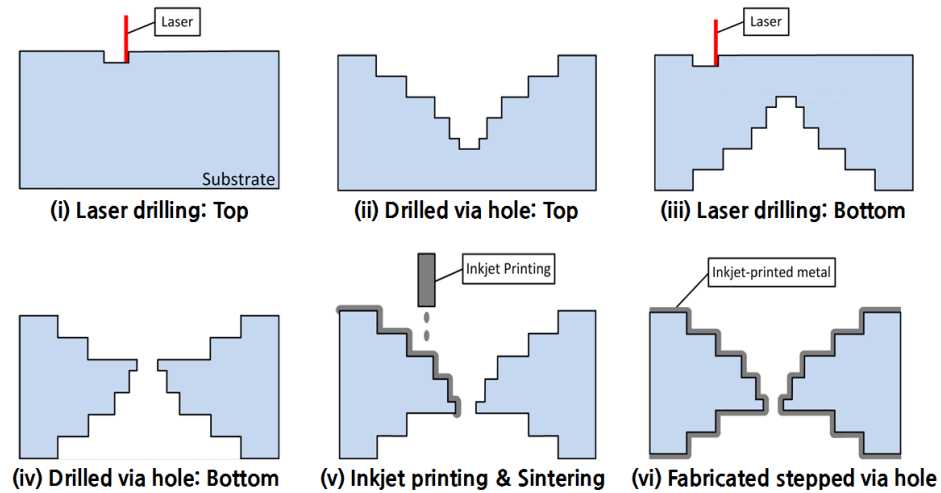


**Figure 6.13** Fabrication process of the stepped via

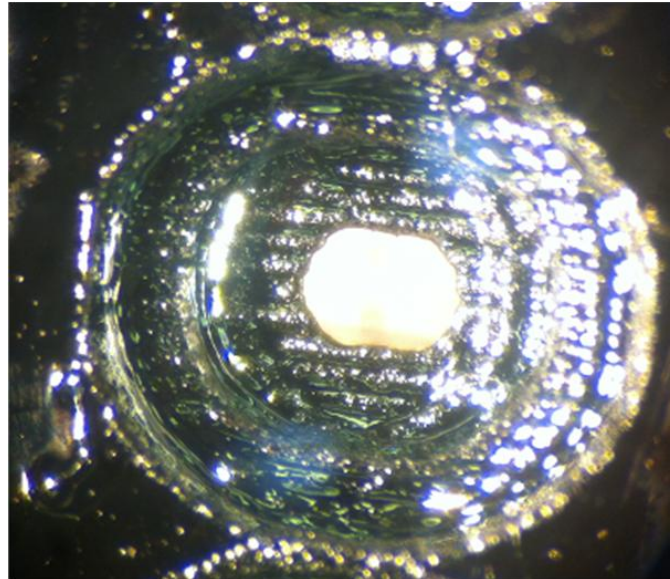
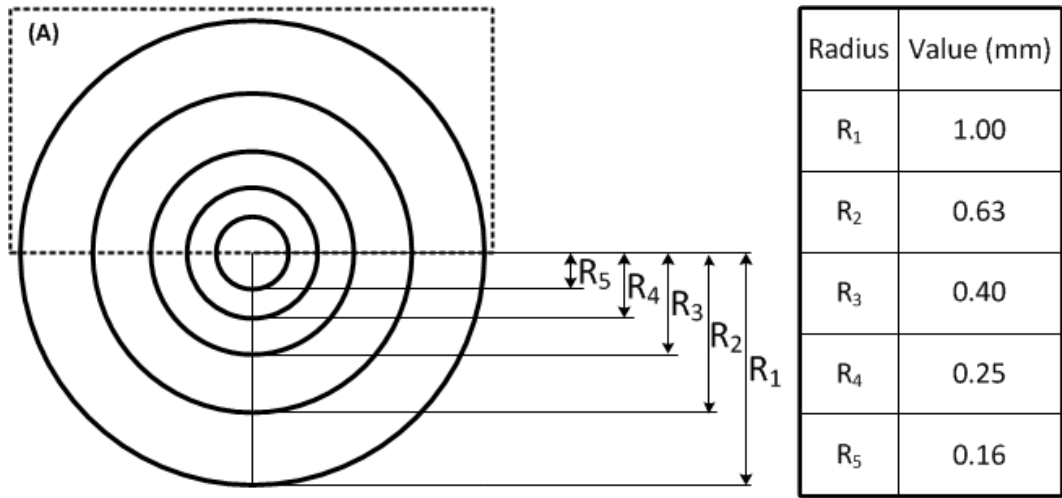


**Figure 6.14** Fabricated inkjet-printed stepped via hole (magnification ratio:  $\times 10$ ).

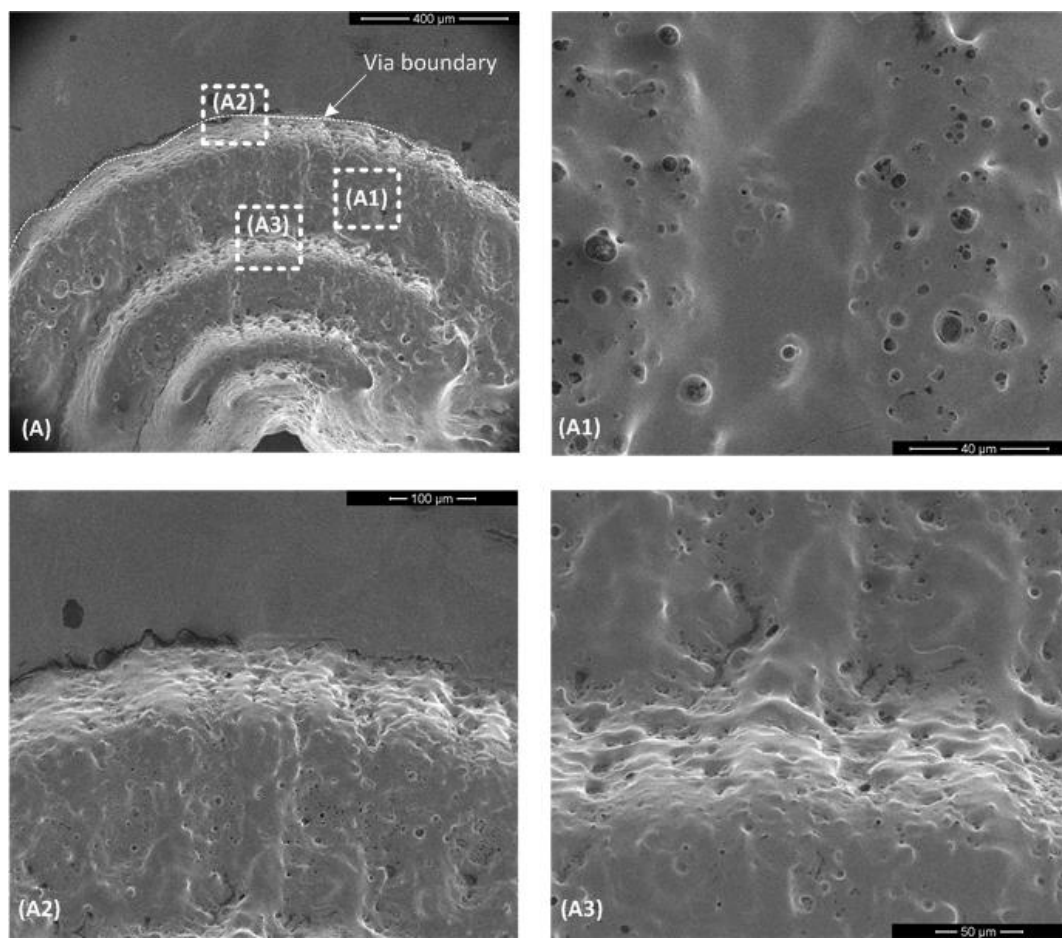
stepped via on the bottom side (Figure 6.13(iii), (iv)). It is necessary to form a smooth transition through the via to the bottom of the substrate. The final step is the inkjet printing process (Figure 6.13(v), (vi)). The fabricated stepped via hole on PMMA is shown in Figure 6.14. This fabrication process is suitable for the inkjet printing because the drilling process and inkjet printing process are completely separated, while the via metallization is easily achieved during the inkjet printing process without any extra

processes. It is a totally dry process which is also advantageous to inkjet printing technology. The fabrication concept shown here on PMMA substrate is for proof of concept only, and is equally applicable to other inkjet printable polymer substrates.

As a design example, 1 mm thick PMMA is used to fabricate inkjet-printed vias as shown in Figure 6.15 and Figure 6.16. The geometries of the stepped via (top and side view) are shown in Figure 6.15(a) and Figure 6.16(a). Five concentric disks are drilled to form a stepped via profile on the top and two concentric disks are drilled on the bottom. The two concentric disks on the bottom with gradually increasing radii ensure that the penetration of the via hole runs through the entire substrate, because the upper five concentric disks with gradually decreasing radii sometime fail to form a through hole due to misalignment of the laser focus or uneven substrate surface. The bottom disks also improve the metal continuity, because they enable a smoother transition from the via to the bottom by chamfering the transition from the via to the bottom which helps form a continuous metal layer. The disk radii of  $R_1$  and  $R_2$  are chosen for the bottom disks to facilitate the alignment and fabrication, since misalignment and fabrication errors can be compensated within the larger radii  $R_1$  and  $R_2$ . The equal via radii at the top and bottom via disks assist in the easier continuation of the layout at the top layer to the layout at the bottom layer. The radius of each circular disk is tabulated in Figure 6.15(a), featuring exponentially tapered values. A Universal laser system's PLS6.75 CO<sub>2</sub> laser is utilized. The laser is raster-scanned over the concentric circles at 1.4 W in a speed of 71 cm/s and a resolution of 1000 pulse per inch (PPI). Five layers of silver nano-particle ink were printed over the engraved stepped via hole using the same inkjet printing machine and settings discussed in Section II-A. The printed via sample was sintered at 120 °C for 2

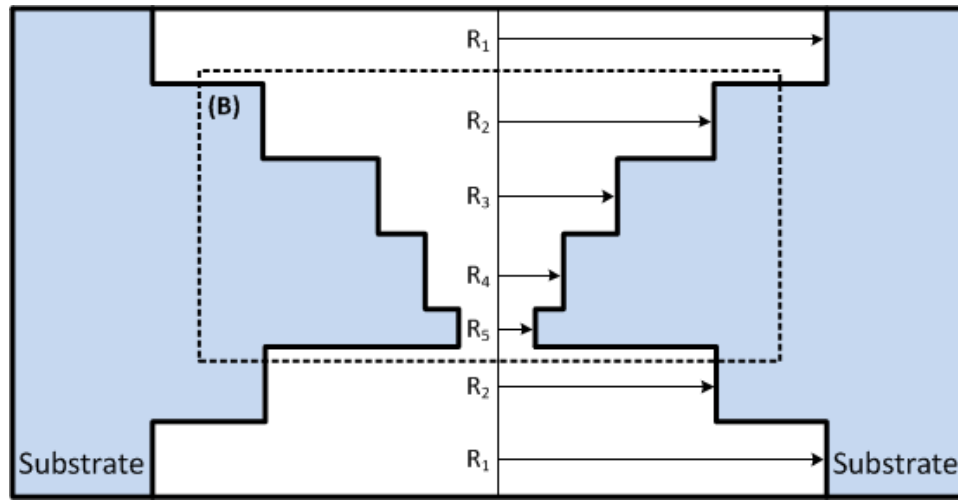


(a)

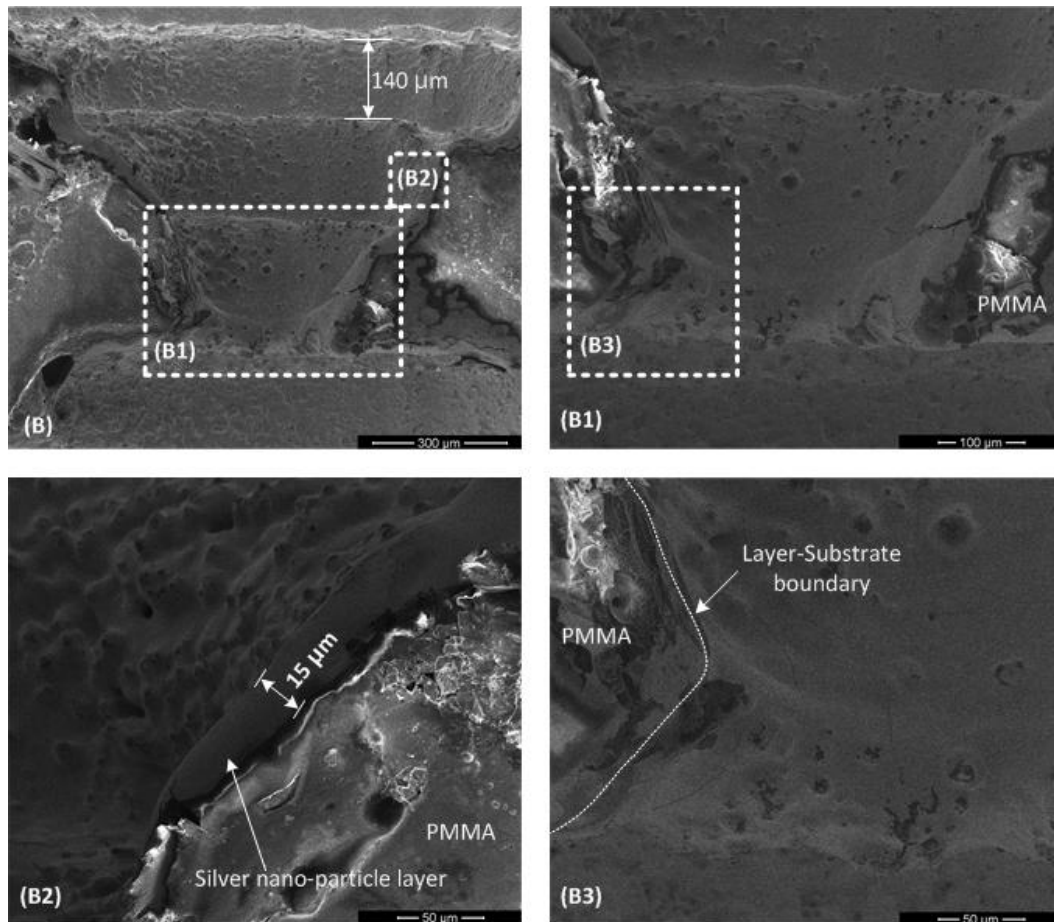


(b)

**Figure 6.15** (a) Geometry of stepped via hole and (b) SEM images of metalized stepped via hole: top view.



(a)



(b)

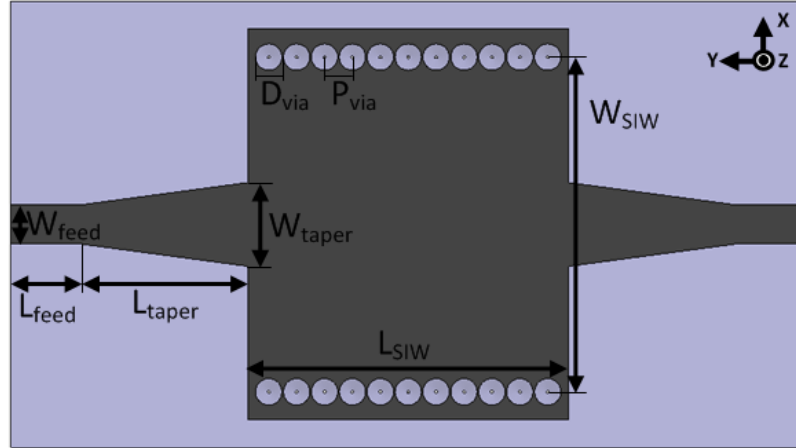
**Figure 6.16** (a) Geometry of stepped via hole and (b) SEM images of metalized stepped via hole: side view



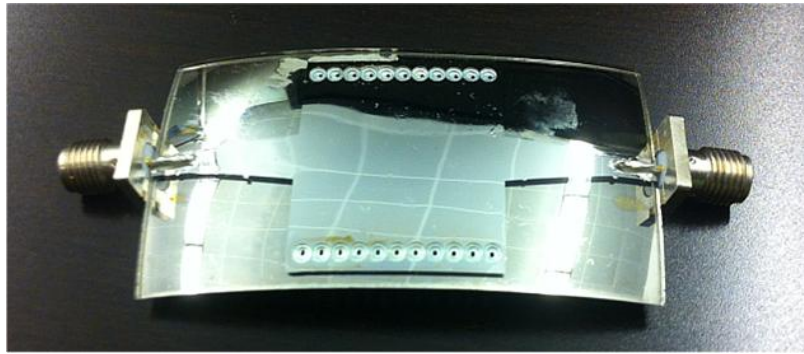
hours. Scanning electron microscope (SEM) images are shown in Figure 6.15(b) and Figure 6.16(b). The Quanta™ 3D FEG SEM tool is utilized in this work. Figure 6.15(b)-(A) shows the semicircle area of the inkjet-printed stepped via which corresponds to the dashed box in Figure 6.15(a) (top view). The stepped via profile is clearly observed with continuous metallization (Figure 6.15(b)-(A)). Each figure in Figure 6.15(b)-(A1) ~ (A3) shows magnified SEM images of corresponding areas depicted in Figure 6.15(b)-(A). Figure 6.15(b)-(A1) shows a planar area of the inkjet-printed stepped via. Figure 6.15(b)-(A2) shows the transition from the surface of the top substrate to the stepped via and Figure 6.15(b)-(A3) shows the transition between two consecutive stepped via disks. The rough surface of the via hole is due to the laser raster scanning which utilizes pulse laser. The profile of the stepped via hole is also shown in Figure 6.16(side view). Figure 6.16(b)-(B) shows the area of the dashed boxes in Figure 6.16(a). The depth of each step is around 140  $\mu\text{m}$  and a continuous silver nano-particle layer is observed throughout the entire stepped via hole. Each figure in Figure 6.16(b)-(B1) ~ (B3) shows magnified SEM images of corresponding areas depicted in Figure 6.16(b)-(B), (B1). The silver nanoparticles form a solid layer along the via hole (Figure 6.16(b)-(B2), (B3)) and a smooth transition from top to bottom is observed (Figure 6.16(b)-(B3)). The transition boundary between the silver nano-particle layer and the PMMA substrate is depicted in dashed line in Figure 6.16(b)-(B3).

### *6.3.5 Fully Inkjet-printed SIW Interconnect*

The results of the inkjet-printed stepped vias and the substrate characterization at microwave frequency range suggest that relatively high conductivity values of inkjet-printed silver nanoparticles ( $4.6 \times 10^6 \sim 8.0 \times 10^6$  S/m) and fabrication of numerous vias



(a)



(b)

**Figure 6.17** (a) Geometry of the  $\mu$ Strip-to-SIW interconnect and (b) the fabricated component on PMMA.

can be easily achieved. As a proof of the via fabrication concept and its application, SIW components with large number of vias are designed, and the prototypes are experimentally investigated.

A simple  $\mu$ Strip-to-SIW interconnect on PMMA has been designed, and it is fully inkjet-printed by introducing the stepped via structure for the first time. Its fundamental mode cutoff frequency ( $f_0$ ) has been set to 4 GHz in order to enable an operating frequency of 5 GHz. The geometry of the proposed  $\mu$ Strip-to-SIW transition is shown in Figure 6.17(a). The SIW and the tapered transition are designed and optimized by following the reported design guide described in [86]. The width ( $W_{SIW}$ ) and the length

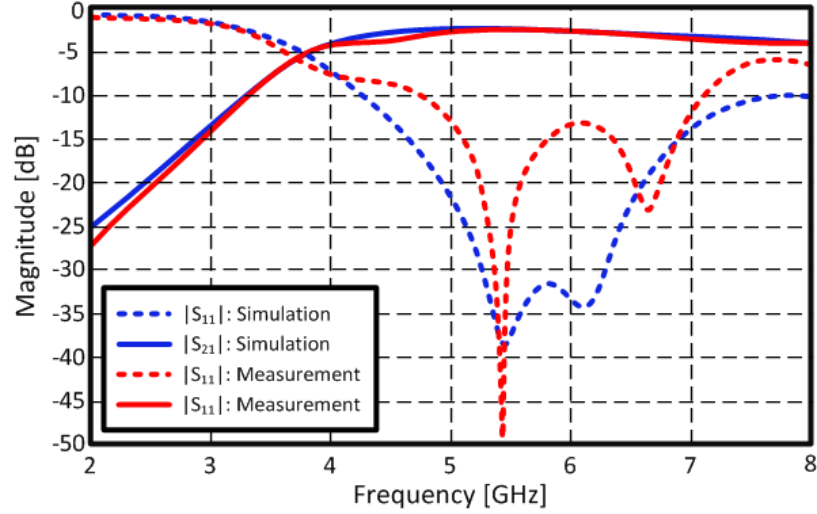


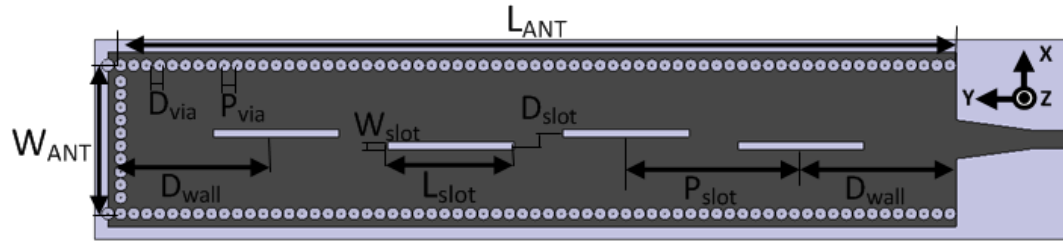
**Figure 6.18** Measured scattering parameters of microstrip-to-SIW transition.

( $L_{SIW}$ ) of the SIW is 24 mm and 23 mm, respectively. The diameter ( $D_{via}$ ) and the pitch ( $P_{via}$ ) of the stepped vias are 2 mm. The length ( $L_{taper}$ ) of the tapered microstrip-to-SIW interconnect is 12 mm and the width ( $W_{taper}$ ) of it is 6 mm. The thickness of the substrate is 1 mm. Figure 6.17(b) shows the fully inkjet-printed  $\mu$ Strip-to-SIW transition on PMMA. The stepped vias are drilled, and then the SIW pattern and the ground plane are printed.

The measured and simulated values of the magnitude of the scattering parameters ( $|S_{11}|$  &  $|S_{21}|$ ) are shown in Figure 6.18, demonstrating a good agreement. The both simulated and measured scattering parameters match to each other very well. The measured insertion loss (IL) of the proposed  $\mu$ Strip-to-SIW at 5 GHz is 2.4 dB. It is notable that inkjet-printed vias have been successfully implemented.

### 6.3.6 Fully Inkjet-printed SIW Slot Antenna

A slotted waveguide SIW antenna is designed on PMMA at 5.6 GHz. The geometry and the fabricated antenna are shown in Figure 6.19(a). The width ( $W_{ANT}$ ) and the length ( $L_{ANT}$ ) of the antenna are 12 mm and 129 mm, respectively. The via diameter ( $D_{via}$ ), the



(a)



(b)

**Figure 6.19** (a) SIW slotted waveguide antenna geometry:  $W_{ANT} = 23$  mm,  $L_{ANT} = 129$  mm,  $D_{wall} = 24$  mm,  $L_{slot} = 19.5$  mm,  $W_{slot} = 1.2$  mm,  $D_{slot} = 2$  mm,  $P_{slot} = 27$  mm,  $D_{via} = 2$  mm, and  $P_{via} = 2$  and (b) fabricated antenna on PMMA.

pitch ( $P_{via}$ ), substrate thickness and the dimensions of  $\mu$ Strip-to-SIW transitions are the same as presented. The distance of the slot from the via wall ( $D_{wall}$ ) is 24 mm and the pitch of the slots ( $P_{slot}$ ) is 27 mm. The distance between consecutive slots is 2 mm. The width ( $W_{slot}$ ) and the length ( $L_{slot}$ ) of the slot are 1.2 mm and 19.5 mm, respectively. Figure 6.19(b) shows the fully inkjet-printed slotted SIW waveguide antenna on PMMA. The fabrication process and inkjet printing settings are the same with those of the microstrip-to-SIW transition. The pitch of the slots ( $P_{slot}$ ) should be half of the guided wavelength ( $\lambda_g/2$ ) in order to maintain in-phase excitation, and the length of the slot ( $L_{slot}$ ) should also be half of the guided wavelength ( $\lambda_g/2$ ) of desired operation frequency [87]. In addition, the distance from the via wall ( $D_{wall}$ ) should be an odd multiple of one quarter of the guided wavelength ( $\lambda_g/4$ ) in order to place the slots at the maximum point of the standing wave due to the short-circuit termination implemented through the via array [88].

The simulated and measured reflection coefficient ( $S_{11}$ ) and gains values for the antenna prototype are shown in Figure 6.20 and Figure 6.21, respectively, showing good agreement. The simulations and the measurements match very well. However, the low gain of the antenna is mainly due to the skin depth ( $\delta$ ) effect. The conductivity of the inkjet-printed silver nanoparticles is  $4.6 \times 10^6$  S/m and the metal thickness ( $t$ ) is about 1.5  $\mu\text{m}$  on PMMA in this work, while the skin depth at 5.6 GHz with the conductivity of  $4.6 \times 10^6$  S/m is 3.14  $\mu\text{m}$ . The thickness of the inkjet-printed metallic layer is only about a half (47.8 %) of the required skin depth at the operation frequency. Most of power is not radiated but dissipated as a loss which results in the antenna gain of -4.8 dBi at 5.6 GHz with the measured radiation efficiency of 0.04 while the simulated radiation efficiency is 0.035. The calculated antenna gain of 2.2 dBi with the radiation efficiency of 0.16 can be achieved when the metal is much thicker than the skin depth  $\delta$  ( $t > 3 \cdot \delta$ ) as shown in Figure 6.21. The thin metal thickness of the inkjet-printed microwave devices is one of the most challenging issues in the inkjet-printing technology area, and it is studied in [89].

The radiation patterns are measured and shown in Figure 6.22. The normalized radiation patterns on E- ( $x$ - $z$ ) and H- ( $y$ - $z$ ) plane of the antenna are measured at 5.6 GHz. The measured and the simulated radiation patterns show good agreement which means that the inkjet-printed vias are metalized very well since no side lobes are observed.

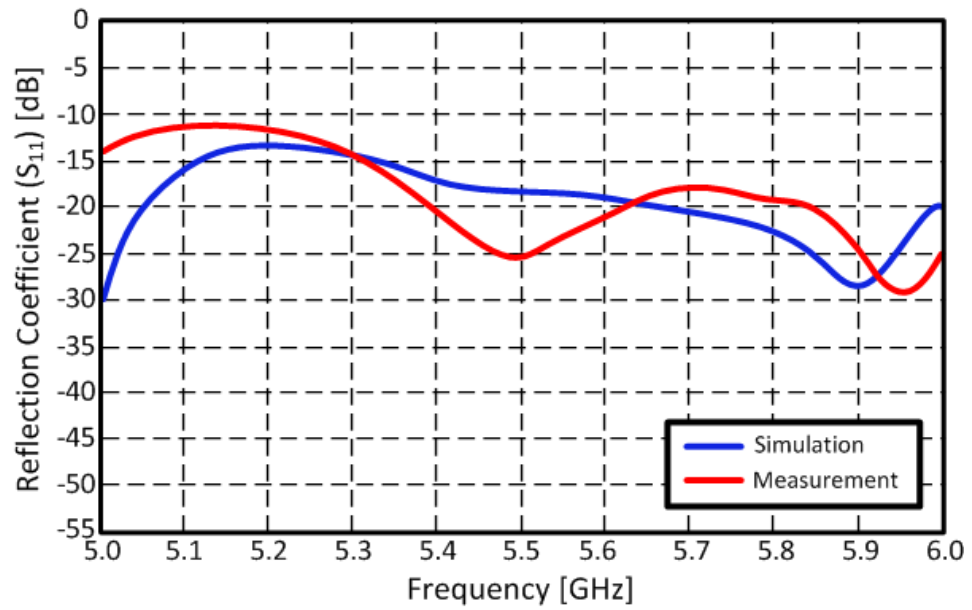


**Figure 6.20** Measured reflection coefficient ( $S_{11}$ ) of the printed antenna.

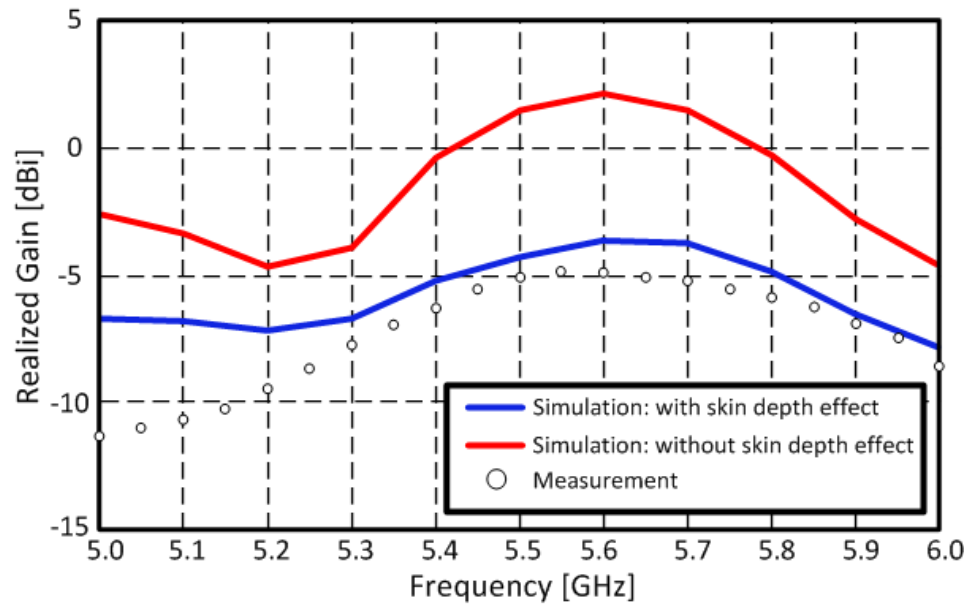


**Figure 6.21** Measured and simulated antenna gain.

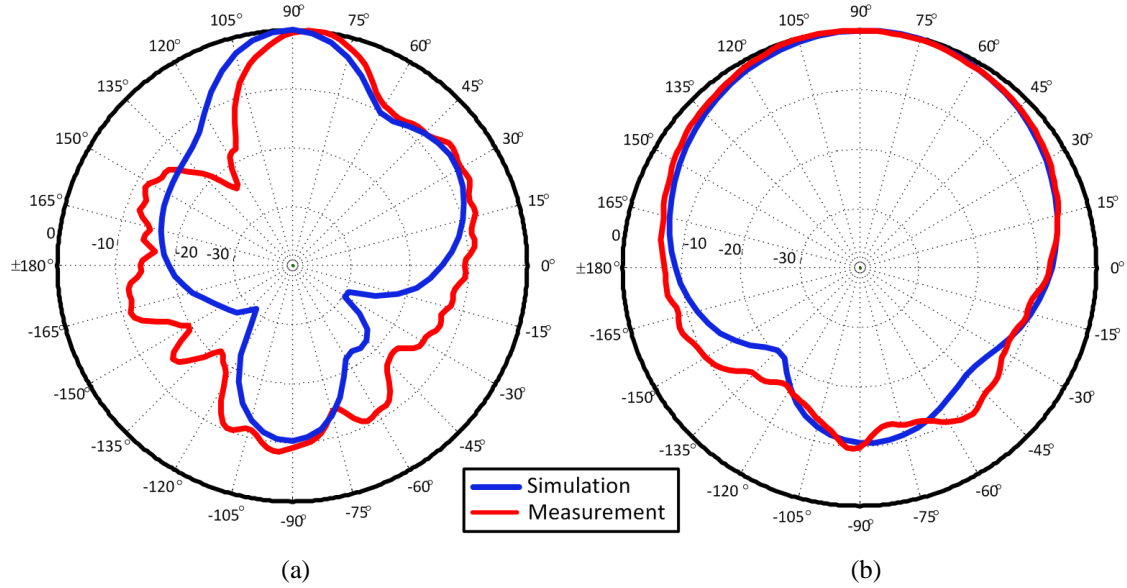


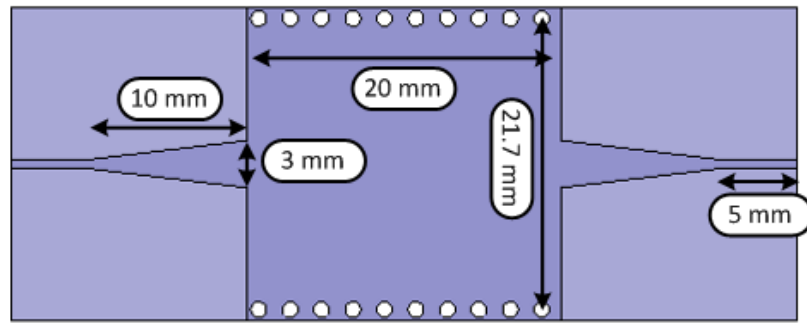
**Figure 6.22** Normalized radiation patterns at 5.6 GHz (a) E-plane (x-z plane) (b) H-plane (y-z plane).

## 6.4 Fully Inkjet-printed SIW Multilayer Coupler

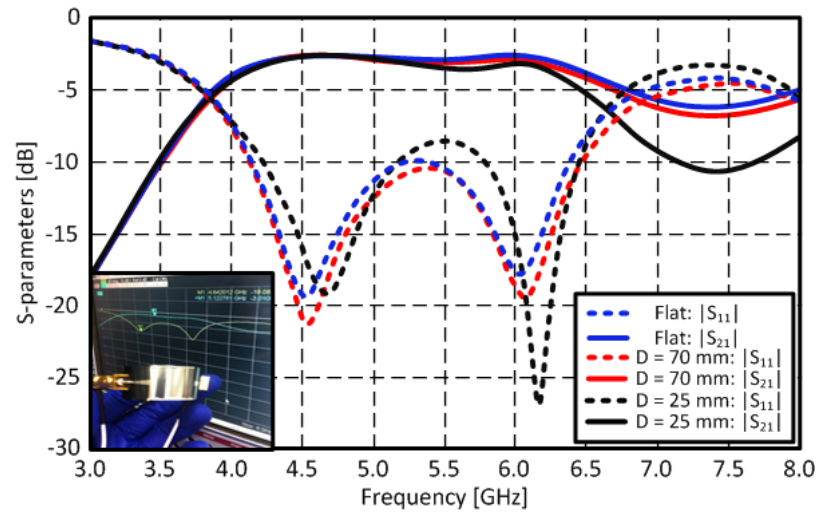
### 6.4.1 Flexible Inkjet-printed SIW Interconnect

An SIW interconnect has been printed on a flexible polyimide film as shown in Figure 6.23(a). The SIW line was designed for the operation frequency of 5.8 GHz, and for this reason the cutoff frequency of the fundamental mode ( $f_0$ ) was set to 4 GHz. The width of the SIW was 21.7 mm, the diameter of metal vias was 1.0 mm and their pitch was 2 mm. The dimensions of the pitch and the diameter of the via holes were chosen to reduce the radiation leakage as well as to minimize the fabrication error [82]. The transition is designed to transform the quasi-TEM mode of microstrip line into the  $TE_{10}$  mode in the SIW. The ratio of length to width is set to 3 and optimized to match the fields of the microstrip line and the SIW [90].

The full wave electromagnetic solver, Ansys HFSS, was used to design and simulate the SIW structure including the microstrip-to-SIW transitions. The substrate thickness is



(a)



(b)

**Figure 6.23** (a) Geometry of flexible SIW interconnect and (b) measured S-parameters ( $S_{11}$  &  $S_{21}$ ) of the SIW interconnect

254  $\mu\text{m}$  which has a dielectric permittivity ( $\epsilon_r$ ) of 3.0 and a loss tangent ( $\tan \delta$ ) of 0.03. For the measurements, a Rhode and Schwartz ZVA-8 VNA was used. The measured insertion loss (IL) of the microstip-to-SIW transition is about 0.8 dB while a reported transition has an IL of 0.2 ~ 0.3 dB because it is built on a low loss substrate whose loss tangent is approximately one-tenth of the polyimide film used in this work [90]. The flexibility of the designed SIW interconnect was tested by wrapping it around a cylinder with various diameters ( $D$ ). The magnitudes of the S-parameters are very stable although the SIW interconnect is bent along cylinders of two radii of curvature ( $D = 70 \text{ mm}$  &  $25 \text{ mm}$ )



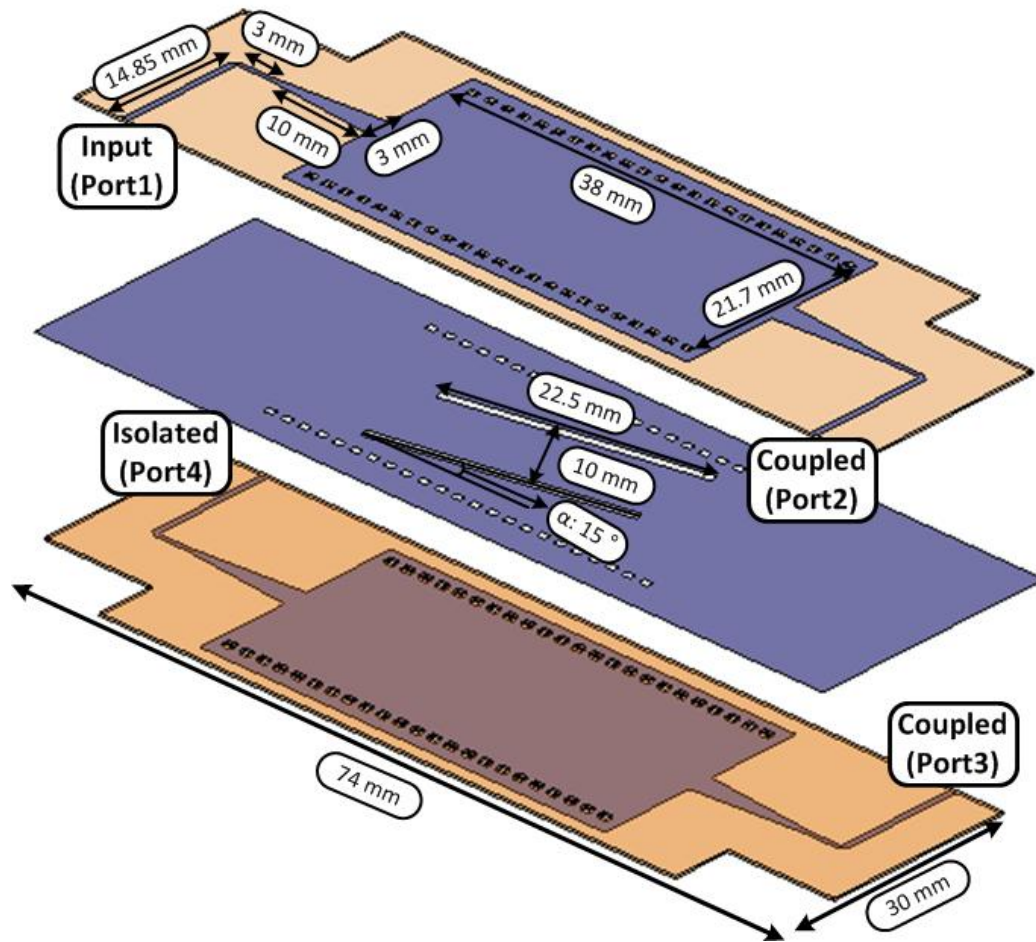


**Figure 6.24** Geometry of the multilayer coupler.

as shown in Figure 6.23(b). It should be noted that the inkjet-printed SIW interconnect showed good repeatability since S-parameters were almost identical before and after bending.

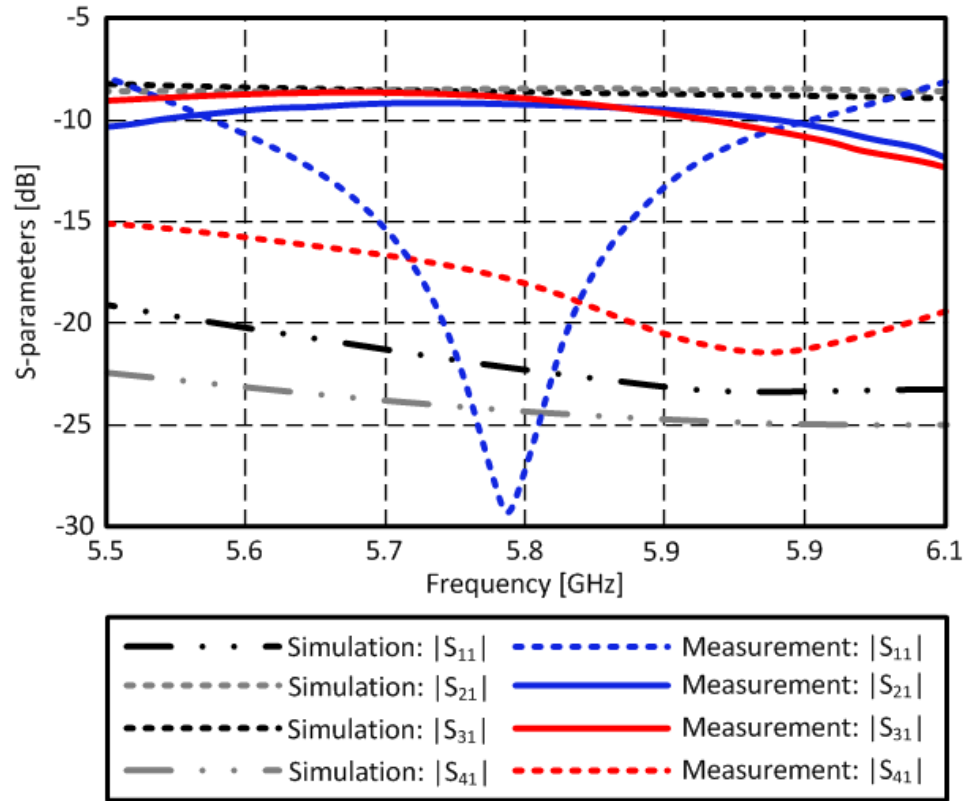
#### 6.4.2 Inkjet-printed Multilayer Coupler

The geometry of the double-layered SIW coupler consists of two SIWs – one on top of the other coupled through two slanted slots as shown in Figure 6.24. The length, the angle and the distance of the 1 mm thick slanted slots are optimized to achieve a maximum coupling level at the operation frequency of 5.8 GHz [91]. Two 254  $\mu\text{m}$  thick

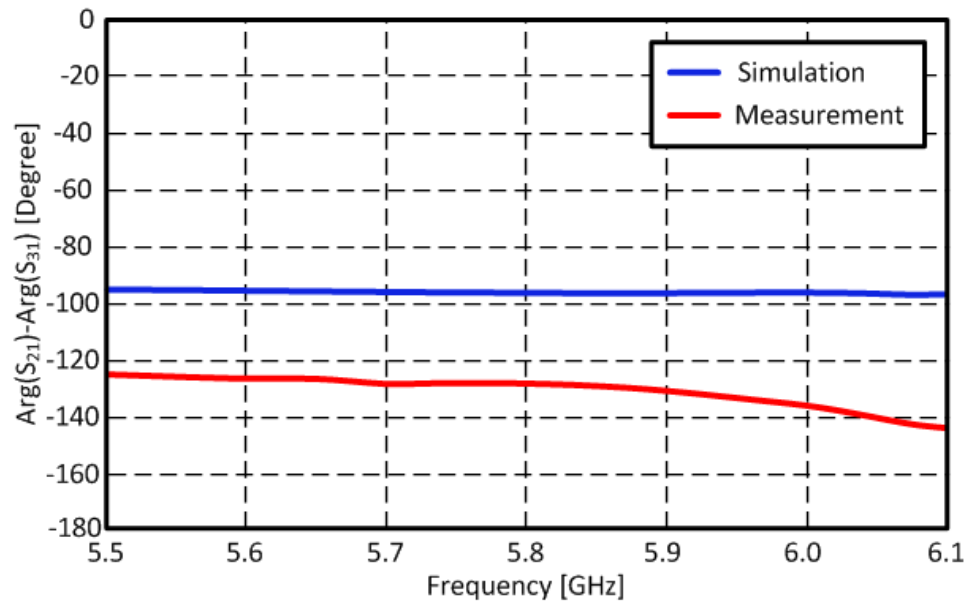
polyimide films are stacked which results in an overall coupler size of 30 mm × 74 mm with total thickness of 0.5 mm. The volume of the proposed coupler ( $0.74\lambda_0 \times 0.42\lambda_0 \times 0.01\lambda_0$ ) in the multilayer SIW configuration was successfully miniaturized by a factor of 58 in terms of wavelength at the operation frequency compared to a previously reported coupler ( $2\lambda_0 \times 1\lambda_0 \times 0.09\lambda_0$ ) [91]. The two individual SIWs have been printed separately on the two overlying polyimide layers that share a ground plane which has the inclined slot for coupling. The proposed coupler has utilized the same fabrication and design method with the flexible inkjet-printed SIW interconnect. The coupler has been designed and optimized for the operation frequency at 5.8 GHz with a 90 degree phase difference between the coupled (Port3) and the direct port (Port2) [92]. The measured 4-port S-parameters and the phase difference are shown in Figure 6.25. The measured insertion loss of the fabricated multilayer coupler is 9.3 dB and the phase difference is 127 degrees at 5.8 GHz as shown in Figure 6.25, while the simulated insertion loss and phase difference are 8.5 dB and 96.7 degrees, respectively. The fabricated coupler has a relatively broad bandwidth of 10.3 %. Additional losses from the conductors have occurred due to the fact that the measured thickness of the printed conductive lines is about 2.4  $\mu\text{m}$  while the skin depth of the printed silver nanoparticle layer at 5.8 GHz is about 2.7  $\mu\text{m}$ .

#### *6.4.3 Printed Multilayer Coupler Fabrication*

The inkjet-printed SIW-based interconnect and broadband coupler are constructed in three steps. The first step involves the cutting of the 254  $\mu\text{m}$  thick substrate along the outline of the design using a laser cutter. Cutting the 254  $\mu\text{m}$  thick polyimide film uses Epilog system's Legend 36EXT with a laser power of 7.2 Watts in a scanning speed of



(a)



(b)

**Figure 6.25** (a) S-parameters of the inkjet-printed multilayer coupler and (b) phase difference between the direct (Port2) and the coupled port (Port3)

5.0 cm/s and a resolution of 1200 pulse per inch (PPI). The laser cut substrate is thoroughly washed in flowing water to wash away the blackening and dust.

Step two is to focus on the inkjet printing of the SIW and ground patterns on the prepared substrate. The substrate surface is cleaned using 99% ethanol. A Dimatix DMP-2800 printer is used to print Advanced Nano Products (ANP) DGP 40LT-15C silver nanoparticle ink. A 10 pL cartridge is utilized in a nozzle temperature of 37.5 °C and a printer's platen temperature of 60 °C with a drop spacing of 30 μm (847 dpi) in order to prevent running of the printed ink on the polyimide film. A higher platen temperature is desirable to dry the printed silver nanoparticle as fast as possible and optimized drop spacing is required to balance the surface energy of the substrate and the surface tension of the printed ink. The ground plane with the slanted slots is printed on one side and the SIW patterns are printed on the other side of the two layers. Each pattern is printed three times. Solid patterns (without via holes) are printed over the via holes in order to form a continuous ink layer on the via holes. The via holes were successfully metalized by printing over the via holes 3 times on each layer. The measured resistance of the 254 μm long inkjet-printed via was about 2.4 ~ 2.7 Ω. The printed pattern is dried at 100 °C for 30 mins and the pattern for the other layer is printed. The alignment function of the printer is utilized to align the printing point which has a 20 μm mechanical error. The printed prototypes are cured at 130 °C for 1 hour as a last step of printing. The measured thickness of every individual inkjet-printed conductive layer with 30 μm drop spacing is about 800 nm and the conductivity value of the cured silver nanoparticle layer is about

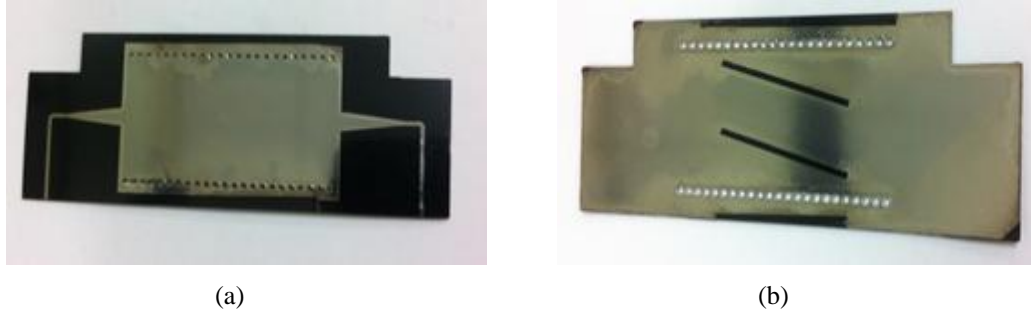


**Figure 6.26** Inkjet-printed multilayer broadband coupler on polyimide film: (a) SIW layer for top and bottom layer (b) ground plane with two slanted slots.

$6 \times 10^6$  S/m. The top and bottom of the printed coupler on kapton are shown in Figure 6.26.

The final step is the alignment and the bonding of the printed layers. Two wires with a diameter that fits the via hole dimensions are inserted in two via holes at opposite via walls to align the top and bottom layer. The via holes are filled by a conductive epoxy to maintain the alignment and firm contact of the two layers.

## 6.5 Summary

Via fabrication technologies depending on substrates utilizing inkjet printing technology have been presented with design examples of SIW components, such as a  $\mu$ Strip-to-SIW interconnect, a cavity filter, and a slot antenna, in this chapter. For the via holes on paper, a mechanical milling machine is chosen to drill via holes to minimize the damages on the substrate, and then cylindrical copper rivets are inserted to metalize the via holes. An inkjet-printed  $\mu$ Strip-to-SIW interconnect, a cavity filter, and an slot antenna on paper are designed and fabricated utilizing the proposed via fabrication technology to investigate the effect and performance of the implemented SIW components on paper. The fabricated SIW components on paper have high insertion loss

due to the high loss tangent of the paper substrates and the thin metallic layer, which is thinner than skin depth, but the implemented vias are working robustly.

Toward the fully inkjet-printed multilayer structures, an inkjet-printed via topology on a thick polymer substrate is thoroughly investigated. The main challenge of implementing the inkjet-printed vias is the crack formation on the via wall due to the low viscosity of the silver nanoparticle ink. Shrinking of the printed nanoparticle ink during the sintering process and gravity make cracks and a non-continuous metallic surface on the vertical via holes. A stepped via hole topology is proposed in order to introduce a gradual change of the via diameter unlike the vertical via hole. The gradual change of the via diameter helps the printed nanoparticle ink to form a continuous metallic layer resulting in fully inkjet-printed via hole on relatively thick substrate. The proposed stepped via topology has been implemented on 1mm thick PMMA and SIW components, such as a  $\mu$ Strip-to-SIW interconnect and an antenna, are designed utilizing the stepped via topology. The measurements of the components have demonstrated the novel performance of the proposed via technology.

The work presented in this chapter is the fundamental study toward the future inkjet-printed via-enabled wireless devices and systems. The next step of this study is to increase the thickness of the inkjet-printed silver nanoparticles on various polymer substrates in order to avoid the skin depth effect or conductor loss. Optimizing the via profile to get a higher aspect ratio and implementing the stepped vias on various substrate are good topics for future work.

## CHAPTER 7

### CONCLUSION

#### 7.1 Summary and Conclusion

In this thesis, the fundamental experimental research on implementing a low-cost flexible autonomous wireless sensor platform was examined. The primary goal of this research was to investigate the feasibility of a flexible autonomous wireless sensor platform featuring wireless communication, a sensing component, an energy harvesting capability, and system integrity. Chapter 2 focused on the electrical properties of the printed metallic layer and Chapter 3 investigated characteristics of various printable flexible substrates. Chapter 4 demonstrated the feasibility of the inkjet-printing technology as a fabrication method for low-cost flexible wireless electronics, such as a high gain wearable antenna and an RF-to-solar power converter. A multiband RF energy harvesting circuit for autonomous/power-efficient operation of the standalone sensor platform was also covered in Chapter 4. Chapter 5 discussed an RFID-enabled sensor topology in detail with design examples and an event detection algorithm. Chapter 6 proposed inkjet-printed via-enabled structures, such as SIW components, for fully inkjet-printed flexible compact multilayer electronics.

Chapters 2 and 3 were a preliminary study for the implementation of the inkjet-printed flexible low-cost autonomous sensor platform. The inkjet printing technology was studied as a fabrication method and various substrate materials were discussed. Primarily, Chapter 2 discussed the electrical properties of the inkjet-printed silver nanoparticle ink and PdCl<sub>2</sub> catalyst ink. The conductivity values of inkjet-printed silver nanoparticles were

studied as a function of the sintering temperature and the number of printed layers. The electrical conductivity value was about  $6 \times 10^6 \sim 10^7$  S/m and the thickness of the printed silver nanoparticles after thermal sintering was about 800 nm per layer with 10 pL droplets. The PdCl<sub>2</sub> catalyst-based electroless electroplating of copper was also studied as well. A seed layer for the copper deposition was printed on the substrate and the substrate was submerged in a copper bath to deposit copper. The electrical property of deposited copper was studied and the electrical properties of the printed silver nanoparticles and deposited copper were discussed. The conductivity of the deposited copper layer was as high as that of the printed silver nanoparticles but the deposited copper had more flexibility compared to the inkjet-printed silver nanoparticles. Chapter 3 studied various substrates compatible with the inkjet-printing process. Basic substrate characterization methods utilizing T- and ring resonators were introduced and electrical properties of Teslin paper and PMMA were studied. Widely used substrates for microwave applications, such as paper, polyimide, and LCP, were summarized as well. Chapters 3 and 4 are fundamental for future research and Chapters 4 to 6 illustrate applications based on the characterization data of the inkjet-printed silver nanoparticles on low-cost substrates. The inkjet-printed microwave components shown in this thesis has been designed utilizing the experimental data from Chapters 2 and 3.

Chapter 4 discussed the feasibility of inkjet-printing technology as a fabrication method for microwave components on flexible substrates. A printed AMC structure for wearable antenna applications, a printed beacon oscillator for WPT, and dual band RF energy harvester were introduced and their design steps and performance were discussed. These are critical components for implementing a low-cost autonomous sensor platform



as the components have been designed for efficient power management and harvesting. The vialess topology of the printed AMC plane was an effective method to isolate the wireless system from adverse environments, such as a human body and a metallic surface. Unwanted power dissipation of the radiated waves from the antenna could be prevented and relatively low power was required to maintain the same communication range in a harsh environment for the wireless system when the antenna was mounted on an AMC plane. Design steps and performance of a printed beacon oscillator or solar-to-RF power convertor were thoroughly discussed. The whole system consisting of solar module, voltage regulator, oscillator, and printed slot antenna was designed and its feasibility as a solar-to-RF power converter and WPT device for the autonomous sensor platform has been demonstrated. A dual band RF energy harvester was also discussed to implement a low power autonomous sensor platform. A 3D folded dual band dipole antenna was proposed and a dual band rectifier circuit was also designed. The antenna and the rectifier were integrated in order to implement a complete RF energy harvesting module. The proposed RF energy harvester successfully harvested 12  $\mu\text{W}$  from 915 MHz and 2.45 GHz when the power density at each frequency band was a  $1 \mu\text{m}/\text{cm}^2$ . The measured conversion efficiency of the rectifier was 37 % at 915 MHz and 20 % at 2.45 GHz in  $1\mu\text{W}$  power density environment. The multi-band RF energy harvesting technology is critical to implement the autonomous wireless sensor platform.

Chapter 5 discussed a sensor topology based on the RFID concept. It features simple geometry, low-cost, and compatibility with prebuilt WSN. The RFID-enabled sensor topology is an important part of the autonomous wireless sensor platform because it can be easily implemented without complex electronics and requires low power to operate the

whole sensor system. Two types of sensor topology—RFID chip-enabled and passive chipless topology—were studied. A dual-tag calibration free RFID-enabled sensor design was proposed and planar printed planar LC resonators were integrated into the sensor tag to suppress the crosstalk and miniaturize the antennas. The communication range of the antenna array was theoretically studied based on measurements. Its event decision method and the sampling rate at the operation frequency band was also statistically discussed using PPMCC values of the sampled signals. A chipless RFID-based passive sensor topology was studied as well. It utilized two linearly polarized waves—vertical and horizontal polarizations—to discriminate interrogation and back-scattered signals. The event was detected based on the resonant frequency shift of the capacitive gap-loaded tunable filter depending on the loaded subjects at the gap.

Chapter 6 discussed via fabrication technologies on various substrates, such as paper and PMMA and SIW components were designed utilizing the proposed via fabrication technologies. Cylindrical copper rivets were inserted in mechanically drilled via holes on paper substrate because inkjet-printed silver nanoparticles were not able to form a continuous metallic layer on the drilled via hole. A  $\mu$ Strip-to-SIW interconnect, a cavity filter and an antenna were designed utilizing the inkjet-printing and the proposed via fabrication technologies on paper substrate. A high insertion loss was observed due to the high loss tangent of paper substrate and thin metal thickness of the printed silver nanoparticles, but this preliminary data demonstrated the feasibility of inkjet-printed SIW structures. A fully inkjet-printed via topology was also studied for multilayer structures. A stepped via hole topology was etched using a laser drill in order to implement gradual change of the via diameter. Concentric disks were etched to implement the gradual

change of the via profile which helped the printed nanoparticle ink to form a continuous metallic layer. It was a scalable topology to any application and SIW components, such as a  $\mu$ Strip-to-SIW interconnect and an antenna, were designed utilizing the proposed stepped vias.

## **7.2 Future Work**

Opportunities for future work involving characterization of nanoparticle-based ink, development of printable electronic inks, improved RFID-enabled sensors, optimized printed wireless components and inkjet-printed via topologies are discussed. These subjects are discussed in more detail in the following sections.

### *7.2.1 Nanoparticle-based Ink Characterization*

Basic electrical properties of inkjet-printed silver nanoparticles were characterized in this thesis but their conditions were limited to the thermal sintering process without any surface treatment. The electrical properties of the printed nanoparticles, such as conductivity and critical thickness (maximum printable thickness), are different depending on sintering methods and the surface energy of the ink. There are also many kinds of commercially available nanoparticle inks which have different electrical features. In this point of view, it is important and valuable to characterize various conductive nanoparticle inks depending on different processing conditions, such as the surface energy of the substrate, the nanoparticle density of the ink, and the sintering process. The experimental data of various nanoparticle inks can be utilized as a reference for printed circuit designers and give an intuition to designers for printing of numerous applications. It is also important to determine a critical height for the printed silver nanoparticle inks depending on substrates. The critical height is the maximum possible height of the

printed ink without running. The printed ink runs when it reaches the critical height, and the desired pattern can be ruined due to ink running. The critical height is a function of surface energy and tension of the ink and substrate so that it is determined by the interactions between the printed ink and the substrate surface. This height is important parameter for designing microwave components as the metal thickness is directly determined by the height of the printed ink. In other words, metal thickness affects the conductor loss from the skin effect which limits the efficiency of RF devices. Therefore, it is important to characterize the critical height of the printed inks depending on substrate.

### *7.2.2 Develop Printable Electronic Inks*

Printable electronic ink development is critical for implementing various sensor platforms. It has been demonstrated that many kinds of sensing materials, such as graphene and CNTs, have been inkjet-printed to implement low-cost printed sensors but their sensitivity and selectivity are still limited. The variation in the reported experimental data is huge depending on reported research. To develop more sensitive and selective inkjet-printable sensing materials is one of the most critical research tasks in order to realize accurate and robust sensor platform. Plus, inkjet printing of the nonlinear electronic devices, such as diodes and transistors, is also important future research topic. Many researches on printed transistors and diodes have only been reported but their performances have been demonstrated at relatively low frequencies. The truly printed nonlinear devices are going to have a disruptive impact on low-cost flexible printed electronics and numerous applications can be built utilizing the printed nonlinear devices. Therefore, developing printable electronic inks for applications such as semiconductor and sensing materials, is very promising research topic of this area.

### *7.2.3 Optimize Printed Wireless Components*

There are numerous remaining questions for applications in inkjet-printed wireless components. First of all, the proposed AMC antenna can be miniaturized. The array size can be miniaturized by increasing the height of the antenna. This work can be scaled to a higher frequency band to miniaturize the antenna size and a body-worn wireless system. Implementation of inkjet-print broadband AMC and Electromagnetic Band Gap (EBG) structures is also one of the major improvements of this work.

The next step of the beacon oscillator is to perform an optimized design of the oscillator element in order to maximize its DC to RF conversion efficiency by considering class-E topologies for the oscillator element. As one of the targeted applications of the proposed system is wireless power transmission, maximizing the DC to RF efficiency in the oscillator will also maximize the amount of RF power that the system will transmit. In addition, this type of system could be potentially used to increase the range of passive RFIDs. Another potential application is to use the proposed beacon oscillator to transmit RF signals in an RFID environment. The presence of additional RF signals apart from the signals from the reader has shown to improve the reading range of passive RFIDs.

### *7.2.4 Integrate RFID-enabled Sensor to WSN*

Numerous researches have been conducted on the RFID-enabled sensors due to their advantages of low-cost and compatibility with prebuilt sensor networks. Especially, many applications can utilize the proposed dual-tag calibration free RFID-enabled sensor topology. The proposed dual-tag RFID-enabled sensor can be deployed in the conventional RFID reader system to verify the capability as a sensor node. The sensor tag

with a meandered coil can be replaced by a printed sensing material to detect a gas, a fluid, or a humidity change. The proposed dipole antenna with the planar LC resonator can be further miniaturized by meandering the line inductor of the LC resonator.

The chipless passive RFID-based sensor is also a promising research topic. Only the feasibility of the system has been demonstrated in this thesis. Functionalized materials can be integrated near the capacitive gap to add a selectivity or a sensitivity of the sensor tag. It is important to implement the proposed chipless passive RFID-based sensor utilizing inkjet-printing process on flexible substrate like a polyimide film to realize a complete inkjet-printed flexible low-cost zero-power "green" RFID-based sensor system.

#### *7.2.5 Optimization and Characterization of the Printed Via*

The inkjet-printed via topology introduced in this thesis is only an experimental proof-of-concept. First of all, the characterization of the inkjet-printed stepped via at microwave frequencies should be studied. The important via features, such as a cut-off frequency, an average DC resistance, a metal thickness, and a RLC lumped element modeling of the inkjet-printed stepped vias, should be defined in order to utilize the proposed via topology. The quality of the proposed inkjet-printed vias can be experimentally verified through implementing a SIW cavity. The Q-factor of the SIW cavity with the inkjet-printed vias will be an index for measuring the quality of the proposed via. The stability of the via fabrication process can be evaluated by measuring the DC resistance of a large via array. The resistance variations of the connected large number of vias will demonstrate the stability of the fabrication process as well as robustness of the fabricated vias. The cut-off frequency of the proposed via can be defined by measuring an eye diagram or S-parameter across a via.

Implementing an inkjet-printed via on paper will be next step of the study. It has been considered that implementing an inkjet-printed via on paper is challenging due to the water absorbing property of paper resulting in a failure to form a continuous nanoparticle layer. Printing a polymer as a passivation layer can be helpful to form a uniform inkjet-printed metallic nanoparticle layer on via hole on paper. It is also possible to combine a screen printing technique to metalize the via hole on paper. Silver paste for screen printing has high viscosity compared to the nanoparticle ink for inkjet printing so that the paste can fill the via hole easily.

## Appendix A: The Effective Width and Effective Permittivity

The characteristic impedance of a microstrip line in static condition with given dimensions can be calculated using (A.1) [93]. The frequency-dependent characteristic impedance can be obtained by (A.2) based on (A.1).  $W$  is the width of the microstrip line,  $H$  is the height of the microstrip line, and  $\epsilon_r$  is the dielectric constant of the substrate. The error value is less than 1% for the ranges of  $0.1 \leq W/H \leq 10$ ,  $1 \leq \epsilon_r \leq 18$ , and  $0 \leq Hf \leq 30$  GHz·mm

$$Z_0(0) = \begin{cases} \frac{119.9}{\sqrt{2(\epsilon_r + 1)}} \left[ \ln \left( \frac{4H}{W} + \sqrt{16 \left( \frac{H}{W} \right)^2 + 2} \right) - \frac{1}{2} \left( \frac{\epsilon_r - 1}{\epsilon_r + 1} \right) \left( \ln \frac{\pi}{2} + \frac{1}{\epsilon_r} \ln \frac{4}{\pi} \right) \right] & (W/H < 3.3) \\ \frac{119.9\pi}{2\sqrt{\epsilon_r}} \left[ \frac{W}{2H} + \frac{\ln 4}{\pi} + \frac{\ln(e\pi^2/16)}{2\pi} \left( \frac{\epsilon_r - 1}{\epsilon_r^2} \right) + \frac{\epsilon_r + 1}{2\pi\epsilon_r} \left[ \ln \frac{\pi e}{2} + \ln \left( \frac{W}{2H} + 0.94 \right) \right] \right]^{-1} & (W/H > 3.3) \end{cases} \quad (\text{A.1})$$

$$Z_0(f) = Z_0(0) \left( \frac{R_8}{R_9} \right)^{R_{12}} \quad (\text{A.2})$$

Where

$$R_1 = 4.766 \exp[-3.228 \left( \frac{W}{H} \right)^{0.641}]$$

$$R_2 = 0.016 + (0.0514 \epsilon_r)^{4.524}$$

$$R_3 = 1.206 - 0.3144 \exp(-0.0389 \epsilon_r^{1.4}) \left[ 1 - \exp(-0.267 \left( \frac{W}{H} \right)^7) \right]$$

$$R_4 = 1 + 1.275 \left[ 1 - \exp\left(-0.00463 R_1 \epsilon_r^{1.674} \left( \frac{Hf}{18.37} \right)^{2.745} \right) \right]$$

$$R_5 = \frac{5.086 R_2 \left( \frac{Hf}{28.84} \right)^{12} \exp\left[-22.2 \left( \frac{W}{H} \right)^{1.92}\right]}{0.384 + 0.386 R_2} \frac{(\epsilon_r - 1)^6}{1 + 1.3 \left( \frac{Hf}{28.84} \right)^{12} + 10(\epsilon_r - 1)^6}$$

$$R_6 = \left[ 0.0962 + \left( \frac{19.47}{Hf} \right)^6 \right]^{-1}$$

$$R_7 = \left[ 1 + 0.00245 \left( \frac{W}{H} \right)^2 \right]^{-1}$$



$$\begin{aligned}
R_8 &= 0.9408\varepsilon_{eff}^{R_4}(f) - 0.9603 \\
R_9 &= (0.9408 - R_5)\varepsilon_{eff}^{R_4}(0) - 0.9603 \\
R_{10} &= 0.707(0.00044\varepsilon_r^{2.136} + 0.0184)\left(\frac{Hf}{12.3}\right)^{1.097} \\
R_{11} &= 1 + 0.0503\varepsilon_r^2 R_6 \left\{ 1 - \exp\left[-\left(\frac{W}{15H}\right)^6\right] \right\} \\
R_{12} &= R_3 \left\{ 1 - 1.1241\left(\frac{R_7}{R_{11}}\right)\exp\left[-0.026(Hf)^{1.1566} - R_{10}\right] \right\}
\end{aligned}$$

The effective permittivity ( $\varepsilon_{eff}$ ) at high frequency can be calculated using the static effective permittivity ( $\varepsilon_{eff}(0)$ ) and effective permittivity dispersion [93].

$$\begin{aligned}
\varepsilon_{eff}(0) &= \frac{\varepsilon_r + 1}{2} \left[ 1 - \frac{1}{2H'} \left( \frac{\varepsilon_r - 1}{\varepsilon_r + 1} \right) \left( \ln\left(\frac{\pi}{2}\right) + \frac{1}{\varepsilon_r} \ln\left(\frac{4}{\pi}\right) \right) \right]^{-2} && \left( \text{when } \frac{W}{H} < 1.3 \right) \\
&= \frac{\varepsilon_r + 1}{2} + \frac{\varepsilon_r - 1}{2} \left( 1 + 10 \frac{H}{W} \right)^{-0.555} && \left( \text{when } \frac{W}{H} > 1.3 \right)
\end{aligned} \tag{A.3}$$

where  $H' = \ln\left(\frac{4H}{W} + \sqrt{16\left(\frac{H}{W}\right)^2 + 2}\right)$

$$\varepsilon_{eff}(f) = \varepsilon_r - \frac{\varepsilon_r - \varepsilon_{eff}(0)}{1 + P(f)} \tag{A.4}$$

and where  $P(f) = P_1 P_2 [(0.1844 + P_3 P_4) 10 f H]^{1.5763}$

$$\begin{aligned}
P_1 &= 0.27488 + [0.6315 + 0.525/(1 + 0.157 f H)^{20}] \left(\frac{W}{H}\right) - 0.065683 \exp(-8.7513 \frac{W}{H}) \\
P_2 &= 0.33622 [1 - \exp(-0.03422 \varepsilon_r)] \\
P_3 &= 0.0363 \exp(-4.6 \frac{W}{H}) \left\{ 1 - \exp\left[-\left(\frac{fH}{3.87}\right)^{4.97}\right] \right\} \\
P_4 &= 1 + 2.751 \left\{ 1 - \exp\left[-\left(\frac{\varepsilon_r}{15.916}\right)^8\right] \right\}
\end{aligned}$$

The effective width ( $W_{eff}$ ) of the microstrip line can be calculated by A.5 using A.2 and A.3. The effective width ( $W_{eff}$ ) of the microstrip line can also be written in simpler form (A.6). In these equations,  $t$  is the thickness of the conductor.

$$W_{eff}(f) = \frac{H\eta_0}{Z_0(f)\sqrt{\epsilon_{eff}(f)}} \quad (\text{A.5})$$

$$W_{eff} = W + \frac{1.25t}{\pi} \left( 1 + \ln \left( \frac{2H}{t} \right) \right)^2 \quad (\text{A.6})$$

## REFERENCE

- [1] I. F. Akyildiz, W. Su, Y. Sankarasubramaniam, and W. Cayirci, "Wireless Sensor Networks: a Survey," *Comput. Netw.*, vol.38, no.4, pp.393-422, Mar. 2002.
- [2] J. Hill, M. Horton, R. Kling, and L. Krishnamurthy, "The Platforms Enabling Wireless Sensor Networks," *Commun. ACM*, vol.47, no.6, pp.41-46, June 2004.
- [3] R. Vyas, V. Lakafosis, H. Lee, G. Shaker, L. Yang, G. Orecchini, A. Traille, M. M. Tentzeris, and L. Roselli, "Inkjet Printed, Self-Powered, Wireless Sensors for Environmental, Gas, and Authentication-Based Sensing," *IEEE Sensors J.*, vol.11, no.12, pp. 3139-3152, Dec. 2011.
- [4] L. Yang, A. Rida, R. Vyas, and M. M. Tentzeris, "RFID Tag and RF Structures on a Paper Substrate Using Inkjet-Printing Technology," *IEEE Trans. Micro. Theo. Tech.*, vol.55, no.12, pp. 2894-2901, Dec. 2007.
- [5] J. Perelaer, A. W. M. de Laat, C. E. Hendriks, and U. S. Schubert, "Inkjet-printed Silver Tracks: Low Temperature Curing and Thermal Stability Investigation," *J. Mater. Chem.*, vol.18, pp.3209-3215, Apr. 2008.
- [6] D. Mager, A. Peter, L. D. Tin, E. Fischer, P. J. Smith, J. Hennig, and J. G. Korvink, "An MRI Receiver Coil Produced by Inkjet Printing Directly on to a Flexible Substrate," *IEEE Trans. Imag.*, vol.29, no.2, pp.482-487, Feb. 2010.
- [7] L. Basiricò, P. Cosseddu, B. Fraboni, and A. Bonfiglio, "Inkjet Printing of Transparent, Flexible, Organic Transistors," *Thin Solid Films*, vol.520, no.4, pp.1291-1294, Dec. 2011.
- [8] A. Rida, L. Yang, R. Vyas, and M. M. Tentzeris, "Conductive Inkjet-Printed Antennas on Flexible Low-Cost Paper-Based Substrates for RFID and WSN Applications," *IEEE Ant. Prop. Mag.*, vol.51, no.3, pp.13-23, June 2009.
- [9] S. Kim, B. Cook, T. Le, J. Cooper, H. Lee, V. Lakafosis, R. Vyas, R. Moro, M. Bozzi, A. Georgiadis, A. Collado, and M. M. Tentzeris, " Inkjet-printed Antennas, Sensors and Circuits on Paper Substrate," *IET Microw. Antenna P.*, vol.7, no.10, pp.858-868, July 2013.
- [10] I. Reinhold, M. Thielen, W. Voit, W. Zapka, R. Gotzen, and H. Bohlmann, "Inkjet Printing of Electrical Vias," in *Proc. EMPC*, Brighton, England, Sep. 2011, pp.1-4.
- [11] T. Kawase, H. Sirringhaus, R. H. Friend, and T. Shimoda, "Inkjet Printed Via-Hole Interconnections and Resistors for All-Polymer Transistor Circuits," *Adv. Mater.*, vol.13, no.21, pp.1601-1605, Nov. 2001.
- [12] T. Falat, J. Felba, A. Moscicki, and J. Borecki, "Nano-silver Inkjet Printed Interconnections Through the Microvias for flexible electronics," in *IEEE-NANO*, Portland, OR, USA, Aug. 2011 pp.473-477.

- [13] B. K. Park, D. Kim, S. Jeong, J. Moon, J. S. Kim, "Direct writing of copper conductive patterns by ink-jet printing", *Thin Solid Films*, vol.515, no.19, pp.7706–7711, Jul. 2007.
- [14] S. B. Fuller, E. J. Wilhelm, and J. M. Jacobson, "Ink-jet printed nanoparticle microelectromechanical systems," *J. Microelectromech. Syst.*, vol.11, no.1, pp.54–60, Feb. 2002.
- [15] Y. Nobusa, Y. Yomogida, S. Matsuzaki, K. Yanagi, H. Kataura, and T. Takenobu, "Inkjet printing of single-walled carbon nanotube thin-film transistors patterned by surface modification," *Appl. Phys. Lett.*, vol.99, no.18, pp.183106–183106-3, Oct. 2011.
- [16] M. F. Mabrook, C. Pearson, and M.C. Petty, "Inkjet-Printed Polymer Films for the Detection of Organic Vapors," *IEEE Sensors J.*, vol.6, no.6, pp.1435–1444, Dec. 2006.
- [17] S.-Y. Han, D.-H. Lee, G. S. Herman, and C.-H. Chang, "Inkjet-Printed High Mobility Transparent–Oxide Semiconductors," *J. Display Technol.*, vol.5, no.12, pp.520–524, Dec. 2009.
- [18] G. Shaker, S. Safavi-Naeini, N. Sangary, and M. M. Tentzeris, "Inkjet Printing of Ultrawideband (UWB) Antennas on Paper-Based Substrates," *IEEE Antennas Wireless Propag. Lett.*, vol.10, pp.111–114, Jan. 2011.
- [19] J. -U. Park, M. Hardy, S. J. Kang, K. Barton, K. Adair, D. Mukhopadhyay, C. Y. Lee, M. S. Strano, A. G. Alleyne, J. G. Georgiadis, P. M. Ferreira and J. A. Rogers, "High-resolution electrohydrodynamic jet printing," *Nature Materials*, **6**, pp.782–789, Aug. 2007.
- [20] B. S. Cook, and A. Shamim, "Inkjet printing of novel wideband and high gain antennas on low-cost paper substrate," *IEEE Trans. Ant. Prop.*, vol.60,no.9, pp. 4148–4156, July 2012.
- [21] K. Maekawa, K. Yamasaki, T. Niizeki, M. Mita, Y. Matsuba, N. Terada, and H. Saito, "Drop-on-Demand Laser Sintering With Silver Nanoparticles for Electronics Packaging," *IEEE Tans. Comp. Pack. Manu. Tech.*, vol.2, no.5, pp.868–877, Feb. 2012.
- [22] B. Polzinger, F. Schoen, V. Matic, J. Keck, H. Willeck, W. Eberhardt, and H. Kueck, "UV-sintering of inkjet-printed conductive silver tracks," in *IEEE NANO 2011*, Portland, OR, Aug. 2011, pp.201–204
- [23] M. Allen, A. Alastalo, M. Suhonen, T. Mattila, J. Leppäniemi, and H. Seppä, "Contactless Electrical Sintering of Silver Nanoparticles on Flexible Substrates," *IEEE Trans. Microw. Theory Techn.*, vol.59, no.5, pp.1419–1429, Apr. 2011.

- [24] M. M. Tentzeris, R. Vyas, V. Lakafosis, T. Le, A. Rida, and S. Kim, "Conformal 2D/3D Wireless Modules Utilizing Inkjet Printing and Nanotechnology", *Microwave Journal*, vol.33, no.2, Feb. 2012.
- [25] U. Caglar, K. Kaija, and P. Mansikkamäki, "Analysis of mechanical performance of silver inkjet-printed structures," in *IEEE INEC 2008*, Shanghai, 2008, pp. 851–856.
- [26] B. S. Cook, Y. Fang, S. Kim, T. Le, W. B. Goodwin, K. H. Sandhage, and M. M. Tentzeris, "Inkjet Catalyst Printing and Electroless Copper Deposition for Low-Cost Patterned Microwave Passive Devices on Paper," *Electron. Mater. Lett.*, vol.9, no.5, pp.669-676, Sep.2013.
- [27] L. Xu, J. Liao, L. Huang, D. Ou, Z. Guo, H. Zhang, C. Ge, N. Gu, and J. Liu, "Surface-bound nanoparticles for initiating metal deposition," *Thin Solid Films*, vol.434, no.1–2, pp.121–125, June 2003.
- [28] I. Ohno, "Electrochemistry of electroless plating," *Mat. Sci. Eng. A-Struct.*, vol.146, no.1–2, pp.33–49, Oct. 1991.
- [29] [Online] Available: <http://www.duracard.com>.
- [30] J. -M. Heinola, K. Tolsa, "Dielectric characterization of printed wiring board materials using ring resonator techniques: a comparison of calculation models," *IEEE Trans. Dielectr. Electr. Insul.*, vol.13, no.4, pp.717–726, Aug. 2006.
- [31] K. P. Latti, M. Kettunen, J. P. Stoem, and P. Silventoinen, "A review of microstrip T-Resonator method in determining the dielectric properties of printed circuit board materials," *IEEE Trans. Ins. Mea.*, vol.56, no.5, pp.1845–1850, Oct. 2007.
- [32] A. R. Fulford and S. M. Wentworth, "Conductor and dielectric-property extraction using microstrip tee resonators," *Microw. Opt. Techn. Lett.*, vol.47, no.1, pp. 14–16, Oct. 2005.
- [33] D. C. Thompson, O. Tantot, H. Jallageas, G. E. Ponchak, M. M. Tentzeris, and J. Papapolymerou, "Characterization of liquid crystal polymer (LCP) material and transmission lines on LCP substrates from 30 to 110 GHz," *IEEE Trans. Microw. Theory Techn.*, vol.52, no.4, pp. 1343–1352, Apr. 2004.
- [34] [Online] Available: <http://www.goodfellow.com/>
- [35] L. Devlin, G. Pearson, and J. Pittock, "RF and microwave component development in LTCC," in *IMAPS Nordic 38th Annu. Conf.*, Sep. 2001, pp. 96–110.
- [36] [Online] Available: <http://www.kapton-dupont.com>.
- [37] H. Sharifi, R. R. Lahiji, L. Han-Chung, P. D. Ye, L. P. B. Katehi, and S. Mohammadi, "Characterization of Parylene-N as Flexible Substrate and Passivation

Layer for Microwave and Millimeter-Wave Integrated Circuits," *IEEE Trans. Adv. Pack.*, vol.32, no.1, pp.84–92, Feb. 2009.

- [38] [Online] Available: <http://www.dow.com>.
- [39] S. Kim, Y. -J. Ren, H. Lee, A. Rida, S. Nikolaou, and M. M. Tentzeris, "Monopole Antenna With Inkjet-Printed EBG Array on Paper Substrate for Wearable Applications," *IEEE Antennas Wireless Propag. Lett.*, vol.11, pp. 663–666, June 2012.
- [40] MCL Technology, Ltd., Dingstow, U.K., "MCL-T whole-body solid SAM phantom," 2012 [Online]. Available: [http://www.mcluk.org/solid\\_bodies.php](http://www.mcluk.org/solid_bodies.php).
- [41] S. Kim, M. M. Tentzeris, and S. Nikolaou, "Wearable biomonitoring monopole antennas using inkjet printed electromagnetic band gap structures," in *Proc. EuCAP 2012*, Prague, Czech, Mar. 2012, pp.181–184.
- [42] H. -S. Tsai and R. A. York, "FDTD analysis of CPW fed folded-slot and multiple-slot antennas on thin substrates," *IEEE Trans. Ant. Prop.*, vol.44, no.2, pp.217–226, Feb 1996.
- [43] F. Giuppi, A. Georgiadis, S. Via, A. Collado, R. Vyas, M. M. Tentzeris and M. Bozzi, "A 927 MHz Solar Powered Active Antenna Oscillator Beacon Signal Generator," in *Proc. WiSNET 2012*, Santa Clara, CA, Jan 2012.
- [44] R. B. Waterhouse and D. Novak, "Small folded CPW fed slot antennas," in *Proc. AP-S 2006*, Albuquerque, NM, July 2006, pp.2599–2602.
- [45] K. Chang, R.A. York, P.S. Hall, and T. Itoh, "Active integrated antennas," *IEEE Trans. Microw. Theory Techn.*, vol.50, no.3, pp.937–944, Mar 2002.
- [46] S. Vaccaro, J.R. Mosig, and P. de Maagt, "Two advanced solar antenna "SOLANT" designs for satellite and terrestrial communications," *IEEE Trans. Antennas Propag.*, vol.51, no.8, pp. 2028–2034, Aug. 2003.
- [47] N. Shinohara, "Power without wires," *IEEE Microw. Mag.*, vol.12, no.7, pp.S64–S73, Dec. 2011.
- [48] A. Boaventura, A. Collado, N. B. Carvalho, and A. Georgiadis, "Optimum behavior: Wireless power transmission system design through behavioral models and efficient synthesis techniques," *IEEE Microw. Mag.*, vol.14, no.2, pp.26–35, 2013.
- [49] K. Niotaki, S. Kim, S. Jeong, A. Collado, A. Georgiadis, and M. M. Tentzeris, "A Compact Dual-Band Rectenna Using Slot-loaded Dual Band Folded Dipole Antenna," *IEEE Antennas Wireless Propag. Lett.*, vol.12, pp.1634–1637, Dec. 2013.

- [50] H. Liu, M. Bolic, A. Nayak, and I. Stojmenovic, "Taxonomy and challenges of the integration of RFID and wireless sensor networks," *IEEE Network*, vol.22, no.6, pp.26–35, Dec. 2008.
- [51] S. Kim, C. Mariotti, F. Alimenti, P. Mezzanotte, A. Georgiadis, A. Collado, L. Roselli, and M. M. Tentzeris, "No Battery Required: Perpetual RFID-Enabled Wireless Sensors for Cognitive Intelligence Applications," *IEEE Microw. Mag.*, vol.14, no.5, pp.66–77, July–Aug. 2013.
- [52] R. Want, "An introduction to RFID technology," *IEEE Pervasive Computing*, vol.5, no.1, pp. 25–33, Feb. 2006.
- [53] D. Girbau, A. Ramos, A. Lazaro, S. Rima, and R. Villarino, "Passive wireless temperature sensor based on time-coded UWB chipless RFID Tags," *IEEE Trans. Microw. Theory Tech.*, vol.60, no.11, pp.3623–3632, Nov. 2012.
- [54] R. A. Potyrailo, C. Surman, S. Go, Y. Lee, T. Sivavec, and W. G. Morris, "Development of radio-frequency identification sensors based on organic electronic sensing materials for selective detection of toxic vapors," *J. Appl. Phys.*, vol.106, no.12, pp.124092:1–6. Dec. 2009.
- [55] C. Occhiuzzi, C. Paggi, and G. Marrocco, "Passive RFID strain-sensor based on meander-line antennas," *IEEE Trans. Antennas Propag.*, vol.59, no.12, pp.4836–4840, Dec. 2011.
- [56] J. Virtanen, L. Ukkonen, T. Bjorninen, A. Z. Elsherbeni, and L. Sydänheimo, "Inkjet-printed humidity sensor for passive UHF RFID systems," *IEEE Trans. Instrum. Meas.*, vol.60, no.8, pp.2768–2777, Aug. 2011.
- [57] B. S. Cook, T. Le, S. Palacios, A. Traille, and M. M. Tentzeris, "Only skin deep: Inkjet-printed zero-power sensors for large-scale RFID-integrated smart skins," *IEEE Microw. Mag.*, vol.14, no.3, pp.103–114, May 2013.
- [58] A. Gluhak, S. Krco, M. Nati, D. Pfisterer, N. Mitton, and T. Razafindralambo, "A survey on facilities for experimental internet of things research," *IEEE Commun. Mag.*, vol.49, no.11, pp.58–67, Nov. 2011.
- [59] S. Shrestha, M. Balachandra, M. Agarwal, V. V. Phoha, and K. Varahramyan, "A chipless RFID sensor system for cyber centric monitoring applications," *IEEE Trans. Microw. Theory Techn.*, vol.57, no.5, pp.1303–1309, May 2009.
- [60] J. Gao, J. Sidén, H.-E. Nilsson, and M. Gulliksson, "Printed humidity sensor with memory functionality for passive RFID tags," *IEEE Sensors J.*, vol.13, no.5, May 2013.
- [61] J. Zhu and G. V. Eleftheriades, "A simple approach for reducing mutual coupling in two closely spaced metamaterial-inspired monopole antennas," *IEEE Antennas Wireless Propag. Lett.*, vol.9, pp.379–382, Apr. 2010.

- [62] F. W. Grover, "Inductance calculations: working formulas and tables," Mineola, NY: Courier Dover Publication, 2004.
- [63] R. Esfandiari, D. W. Maki, and M. Siracusa, "Design of interdigitated capacitors and their application to gallium arsenide monolithic filters," *IEEE Trans. Microw. Theory Techn.*, vol.31, no.1, pp.57–64, Jan. 1983.
- [64] H. Meier, U. Löffelmann, D. Mager, P. J. Smith, and J. G. Korvink, "Inkjet printed, conductive, 25  $\mu\text{m}$  wide silver tracks on unstructured polyimide," *Phys. Status Solidi A*, vol.206, no.7, pp.1626–1630, July 2009.
- [65] H. Lee, S. Kim, D. De Donno, and M. M. Tentzeris, "A novel ""Universal" inkjet-printed EBG-backed flexible RFID for rugged on-body and metal mounted applications," in *IEEE MTT-S International Microwave Symposium Digest (MTT)*, Montréal, Canada, Jun. 2012, pp.1–3.
- [66] S. -H. Hwang, T. -S. Yang, J. -H. Byun, and A. S. Kim, "Complementary pattern method to reduce mutual coupling in metamaterial antennas," *IET Microw. Ant. Prop.*, vol.4, no.9, pp.1397–1405, Sep. 2010.
- [67] Gabriel, C., "Compilation of the dielectric properties of body tissues at RF and microwave frequencies", Brooks Air Force Technical Report AL/OE-TR-1996-0037, 1996.
- [68] K. V. S. Rao, P. V. Nikitin, and S. F. Lam, "Antenna design for UHF RFID tags: a review and a practical application," *IEEE Trans. Antennas Propag.*, vol.53, no.12, pp.3870–3876, Dec. 2005.
- [69] J. R. Mautz and R. Harrington, "Modal analysis of loaded N-port scatterers," *IEEE Trans. Antennas Propag.*, vol.21, no.2, pp. 188–199, Mar. 1973.
- [70] R. E. Collin, *Antennas and Radiowave Propagation*. New York: Mc-Graw-Hill, 1985.
- [71] A. Georgiadis, G. Andia-Vera, A. Collado "Rectenna design and optimization using reciprocity theory and harmonic balance analysis for electromagnetic (EM) energy harvesting," *IEEE Antennas Wireless Propag. Lett.*, vol.9, pp.444–446, May 2010.
- [72] G. Marrocco, "RFID grids: Part I—Electromagnetic theory," *IEEE Trans. Antennas Propag.*, vol.59, no.3, pp. 1019–1026, Mar. 2011.
- [73] C. A. Balanis, *Antenna Theory: Analysis and Design*, 3<sup>rd</sup> Edition, Wiley, 2005.
- [74] [Online] Available: <http://www.voyantic.com/tagformance>.



- [75] Understanding the FCC regulations for low-power, non-licensed transmitters, Federal Communications Commission (FCC), OET Bulletin no.63, Feb. 1996.
- [76] J. L. Rogers and W. A. Nicewander, "Thirteen ways to look at the correlation coefficient," *The Am. Stat.*, vol.42, no.1, pp.59–66, Feb. 1988.
- [77] R. B. Dell, S. Holleran, and R. Ramakrishnan, "Sample Size Determination," *ILAR J.*, vol.43, no.4, pp.207–213, Apr. 2002.
- [78] V. K. Tripathi and I. Wolff, "Perturbation Analysis and Design Equations for Open- and Closed-Ring Microstrip Resonators," *IEEE Trans. Microw. Theory Techn.*, vol.32, no.4, pp.405–410, Apr. 1984.
- [79] B. Cook, J. Cooper, S. Kim, and M. M. Tentzeris, "A Novel Inkjet-Printed Passive Microfluidic RFID-based Sensing Platform," *IEEE MTT-S International Microwave Symposium Digest (MTT)*, Seattle, WA, 2013.
- [80] R. S. Nair, E. Perret, S. Tedjini, and T. Baron, "A Group-Delay-Based Chipless RFID Humidity Tag Sensor Using Silicon Nanowires," *IEEE Antennas Wireless Propag. Lett.*, vol.12, pp.729–732, June 2013.
- [81] R. Want, "Enabling ubiquitous sensing with RFID," *Computer*, vol.37, no.4, pp.84–86, Apr. 2004.
- [82] M. Bozzi, A. Georgiadis, and K. Wu, "Review of Substrate Integrated Waveguide (SIW) Circuits and Antennas," *IET Microw. Antennas Prop.*, vol. 5, no. 8, pp. 909–920, June 2011.
- [83] G. H. Kim, "A PMMA composite as an optical diffuser in a liquid crystal display backlighting unit (BLU)," *Eur. Polym. J.*, vol.41, no.8, pp.1729–1737, Aug. 2005.
- [84] K. -J. Baeg, D. Khim, J. Kim, D.-Y. Kim, S.-W. Sung, B.-D. Yang, and Y.-Y. Noh, "Flexible Complementary Logic Gates Using Inkjet-Printed Polymer Field-Effect Transistors," *IEEE Electron Device Lett.*, vol.34, no.1, pp.126–128, Jan. 2013.
- [85] F. Mira, J. Mateu, and M. Bozzi, "Substrate Integrated Waveguide Predistorted Filter at 20 GHz," *IET Microw. Antennas Prop.*, vol.5, no.8, pp.928–933, June 2011.
- [86] D. Deslandes, and K. Wu, "Accurate modeling, wave mechanisms, and design considerations of a substrate integrated waveguide," *IEEE Trans. Microw. Theory Techn.*, vol.54, no.6, pp.2516–2526, Jun. 2006.
- [87] A. M. Ali, H. B. El-Shaarawy, and H. Aubert, "Millimeter-Wave Substrate Integrated Waveguide Passive Van Atta Reflector Array," *IEEE Trans. Antennas Propag.*, vol.61, no.3, pp.1465–1470, Mar. 2013.

- [88] R. S. Elliott, "An improved design procedure for small arrays of shunt slots," *IEEE Trans. Antennas Propag.*, vol.31, no.1, pp.48–53, Jan. 1983.
- [89] C. E. Hendriks, P. J. Smith, J. Perelaer, A. M. J. van de Berg, and U. S. Schubert, "'Invisible' Silver Tracks Produced by Combining Hot-Embossing and Inkjet Printing," *Adv. Funct. Mater.*, vol.18, no.7, pp.1031–1038, Apr. 2008.
- [90] D. Deslandes and K. Wu, "Integrated Microstrip and Rectangular Waveguide in Planar Form," *IEEE Microw. Wireless Compon. Lett.*, vol.11, no.3, pp.68–70, Feb. 2001.
- [91] J. -X. Chen, W. Hong, Z. -C. Haom H. Li and K. Wu, "Development of a Low Cost Microwave Mixer using a Broad-band Substrate Integrated Waveguide (SIW) Coupler," *IEEE Microw. Wireless Compon. Lett.*, vol.16, no.2, pp.84–86, Feb. 2006.
- [92] A. A. M. Ali, N. J. G. Fonseca, F. Coccetti and H. Aubert, "Design and Implementation of Two-Layer Compact Wideband Butler Matrices in SIW Technology for Ku-Band Applications," *IEEE Antennas Propag. Mag.*, vol.59, no.2, pp.503–512, Jan. 2010.
- [93] T. C. Edwards, *Foundations for Microstrip Circuit Design*, Wiley, Great Britain, 1981.

## VITA

Sangkil Kim was born in Seoul, Republic of Korea, 1984. He received the B.S. degree in electrical and electronic engineering from Yonsei University, Seoul, Korea, in 2010. He received the M.S and Ph.D degree in electrical engineering from Georgia Institute of Technology, Atlanta, GA, in 2012 and in 2014, respectively. He visited King Abdullah University of Science and Technology (Thuwal, Saudi Arabia, 2013), CTTC (Barcelona, Spain, 2013) and CNRS-LAAS (Toulouse, France, 2013) as a visiting scholar. He authored and co-authored 31 conference papers and 12 journal papers. He also participated in writing 5 book chapters. His Ph.D thesis topic is the design and implementation of inkjet-printed novel 2D/3D wireless autonomous sensor platform.